ALMA MATER STUDIORUM - UNIVERSITÀ DI BOLOGNA

FACOLTA' DI INGEGNERIA

CORSO DI LAUREA SPECIALISTICA IN INGEGNERIA CIVILE

D.I.S.T.A.R.T.
DIPARTIMENTO DÌ INGEGNERIA DELLE STRUTTURE, DEI
TRASPORTI, DELLE ACQUE, DEL RILEVAMENTO, DEL TERRITORIO

TESI DI LAUREA
in
Tecnica delle Costruzioni LS

DYNAMIC TESTS AND STRUCTURAL IDENTIFICATION OF THE DOWLING HALL FOOTBRIDGE

CANDIDATO:

Stefano Sensoli

RELATORE:
Chiar.mo Prof.
Claudio Ceccoli

CORRELATORI:
Prof. Ing. Tomaso Trombetti
Prof. Ing. Babak Moaveni

Anno Accademico 2008/2009

Sessione III

Ai miei genitori,
per aver reso possibile la bellezza di questi anni.
Ai miei amici,
per avermi accompagnato ed abbracciato.

Index

INTRODUZIONE

Questo lavoro riguarda la progettazione e la realizzazione di due test dinamici eseguiti sul Dowling Hall Footbridge, sito presso il campus centrale della Tufts University, Medford, USA. Dai dati rilevati nei due test, è stato possibile, attraverso l'implementazione di adeguati algoritmi di calcolo, identificare le caratteristiche dinamiche della struttura e aggiornare e affinare il modello numerico agli elementi finiti creato per simulare il comportamento strutturale.

I test dinamici sono strumenti ampiamente utilizzati nell'ingegneria civile per identificare le caratteristiche dinamiche delle strutture (frequenze naturali, coefficienti di smorzamento, forme modali). Negli ultimi decenni si è riscontrato un interesse crescente intorno a quest'ambito, sia per la notevole attenzione suscitata dalla progettazione di strutture in zona sismica, sia per la possibilità di verificare e affinare modelli numerici grazie ai risultati ottenuti dalle prove sperimentali.

I test dinamici sono operativamente realizzati attraverso l'applicazione, in posizioni specifiche e accuratamente pianificate, di sensori capaci di rilevare molteplici tipologie di parametri, ambientali (temperatura, umidità, ecc.) e strutturali (accelerazioni, velocità, ecc.), che consentano una descrizione approfondita e completa di tutti i fattori che caratterizzano il comportamento della struttura sottoposta alle diverse tipologie di sollecitazione. In particolare è possibile identificare due diverse modi di svolgimento dei test, in cui la struttura risulta eccitata attraverso azioni di tipo ambientale (vento, traffico, pedoni) oppure attraverso l'utilizzo di appositi dispositivi meccanici che generano input dinamici programmati (shakers, vibrodine, ecc.). In entrambi i casi è possibile identificare le caratteristiche dinamiche facendo uso di appropriati algoritmi per l'identificazione strutturale che interpretino correttamente gli output della struttura a seguito della sollecitazione impressa.

Per il caso in esame, i test sono stati condotti utilizzando un'eccitazione di tipo ambientale e registrando la risposta della struttura attraverso dodici accelerometri disposti sull'intera lunghezza della passerella pedonale. Per analizzare i dati acquisiti durante i test, si sono ricorsi all'implementazione di due algoritmi numerici in grado di fornire le caratteristiche dinamiche richieste. In particolare, si è fatto uso del Peak-Picking method (PP) e del Natural Excitation Technique combinato con l'Eigensystem Realization Algorithm (NExT-ERA). Entrambi gli algoritmi permettono l'identificazione delle caratteristiche dinamiche della struttura partendo dagli output registrati utilizzando gli accelerometri. Il Peak-Picking utilizza l'output prodotto nel dominio delle frequenze, identificando i picchi del modulo della FRF (Funzioni di risposta in frequenza) per la determinazione delle frequenze proprie della struttura. Il NExT-ERA analizza l'output direttamente nel dominio del tempo e permette, attraverso la risoluzione di un sistema agli autovalori/autovettori, di ottenere le caratteristiche dinamiche in maniera totalmente automatica. Grazie all'identificazione strutturale è possibile descrivere adeguatamente il comportamento della struttura in campo dinamico.

Entrambi gli algoritmi impiegati sono risultati essere strumenti adeguati all'identificazione delle caratteristiche dinamica della struttura. Essi permettono di automatizzare la proceduta d'identificazione, rendendo possibile la loro applicazione a un sistema di monitoraggio continuo che permetta di conoscere lo stato strutturale nel tempo.

Comparando i dati ottenuti dall'applicazione dei due algoritmi, risulta che essi producono risultati confrontabili per quanto riguarda la precisione di calcolo e la raffinatezza d'identificazione delle caratteristiche dinamiche, nonostante siano di complessità differente, soprattutto per quanto riguarda l'onore computazionale. In particolare, il Peak-Picking è meno raffinato e di più facile interpretazione e maneggevolezza, essendo comunque capace di produrre risultati in linea con quelli proposti dal modello teorico di calcolo agli elementi finiti. Nonostante ciò, esso non può essere completamente automatizzabile, ma riserva la scelta delle frequenze naturali d'interesse come dato iniziale del problema. La sua semplicità lo rende tuttavia uno strumento ampiamente adottato nell'analisi strutturale.

Il NExT-ERA è uno strumento maggiormente raffinato, che richiede onori computazionali elevati, soprattutto in relazione alla presenza di una molteplicità di rilevazioni e alla loro durata temporale. Esso consente però la piena automatizzazione del processo di calcolo dall'output registrato dagli accelerometri direttamente nel dominio del tempo e realizza l'analisi partendo da una sollecitazione generica, sia di tipo impulsivo sia di tipo ambientale. I risultati ottenibili hanno una precisione elevata rendendo il NExT-ERA, lo strumento prescelto per l'elaborazione dei dati nel sistema di monitoraggio in continuo che si andrà a progettare.

Dai risultati dei test eseguiti è stato possibile identificare la strumentazione adeguata da installare per l'identificazione delle proprietà dinamiche della struttura, che sia in grado di tenere in considerazione le esigenze di tipo ambientale (grandi variazioni temperatura e umidità stagionali) e strutturali (posizione dei sensori, frequenze proprie rilevabili).

Il progetto prevede la realizzazione futura di un sistema di monitoraggio in continuo dei dati con l'intento di fornire informazioni sullo stato della struttura nel corso della sua vita, per identificare la presenza di eventuali danni o problematiche che potrebbero comprometterne l'integrità funzionale o strutturale. Inoltre, le informazioni generate da tale sistema offriranno le basi per la pianificazione di un'adeguata opera di manutenzione che prevenga l'insorgere di possibili situazioni di pericolo e consentano di salvaguardare l'integrità strutturale nel tempo.

I risultati dell'analisi sperimentali sono stati validati attraverso la realizzazione di un'analisi numerica ottenuta attraverso la creazione di un modello agli elementi finiti della struttura. Esso ha permesso di scongiurare che i risultati dell'analisi sperimentale fossero affetti da errori grossolani. Accertata l'accuratezza dei risultati dell'analisi sperimentali, questi sono stati utilizzati come punto di partenza per la calibrazione e l'aggiornamento del modello agli elementi finiti, in modo che esso potesse simulare il comportamento reale della struttura con la massima precisione possibile.

Nel primo capitolo viene presentata la struttura oggetto dei test dinamici, il Dowling Hall footbridge. In primo luogo sono presentate la caratteristiche geometriche e strutturali. Quindi, si analizza la scelta operata a proposito delle strumentazioni adottata per la rilevazione dei dati acquisiti durante i test, con la giustificazione della caratterizzazione delle specifiche di ogni elemento che compone la della postazione di registrazione. Successivamente sono descritti i test dinamici, la loro progettazione, pianificazione e realizzazione con l'illustrazione dettagliata della posizione dei sensori e dei modi di esecuzione di ogni test. Segue il capitolo riguardante l'implementazione dei sistemi d'identificazione strutturale e della loro applicazione agli output ottenuti dai test. I dati sono innanzitutto elaborati in modo da ottenere un segnale di qualità adatta all'analisi grazie all'adozione di strumenti di analisi dei segnali. Nel terzo capitolo, sono stati elaborati i risultai dell'analisi, raccolti e confrontati mettendo in evidenza le peculiarità dei diversi algoritmi per entrambe i test eseguiti. Nell'ultimo capitolo, i risultati dell'analisi sperimentale sono stati confrontati con quelli derivanti dall'analisi fatta attraverso un modello computerizzato agli elementi finiti, il quale è stato affinato e perfezionato in base ai risultati dell'analisi sperimentale. Questo consente di verificare la bontà del modello utilizzato in fase di progettazione e permette di valutare la necessità di eventuali interventi di adeguamento strutturale. Infine si analizzano le soluzioni progettuali per la realizzazione di un sistema di monitoraggio continuo che utilizzi un'eccitazione di tipo ambientale e che sia in grado di fornire dati riguardanti le caratteristiche dinamiche della struttura.

Questo lavoro ha permesso di analizzare e valutare tutte le fasi che riguardano la progettazione e la realizzazione di un sistema per l'identificazione delle caratteristiche dinamiche della struttura partendo dalle scelta della strumentazione richiesta e dalla progettazione e realizzazione dei test dinamici preliminari, della scelta, implementazione ed adeguatezza degli algoritmi di calcolo che permettono di comprendere il comportamento della struttura in campo dinamico e di progettare adeguatamente le soluzioni progettuali di messa in opera dei sensori e della strumentazione necessaria. Questo lavoro fornisce le basi per una adeguata progettazione e realizzazione del sistema di monitoraggio continuo che verrà realizzato per il monitoraggio del Dowling Hall footbridge in un prossimo futuro.

INTRODUCTION

This work is focused on the design and realization of two dynamic tests performed on the Dowling Hall Footbridge, located at the central campus of Tufts University, Medford, USA. The data collected in the two tests were analyzed through the implementation of appropriate algorithms, to identify the dynamic characteristics of the structure and update and refine a finite element numerical model designed to simulate the structural behavior.

The dynamic tests are a widely used civil engineering to identify the dynamic characteristics of structures (e.g. natural frequencies, damping ratios, modal forms). Over the past decades have seen a growing interest around this area, both for the considerable attention paid to the design of structures in seismic areas, and for the opportunity to test and refine numerical models due to the results obtained from experimental tests.

The dynamic tests are works through the implementation in a specific location and carefully planned, the sensors can detect multiple types of parameters, environmental (e.g. temperature, humidity, etc.) and structural (e.g. acceleration, speed, etc.), allowing the thorough and comprehensive description of all the factors that characterize the behavior of the structure subjected to different types of stress. In particular, it is possible to identify two different modes of tests, in which the structure is excited by raising ambient excitation (e.g. wind, traffic, pedestrians), or through the use of mechanical devices that generate input dynamic program (e.g. shakers, vibrodine, etc.). In both cases dynamic characteristics can be identified by using the appropriate algorithms for identifying structural characteristics by the correct interpretation of the output of the structure as a result of the solicitation impressed.

Modal analysis methodologies can be divided in two categories. First, Experimental Modal Analysis (EMA) employs an artificial excitation (e.g. mechanical shakers, instrumented hammers) in order to measure the frequency response function (FRF) or the impulse response function (IRF), which are typically used for modal parameters extraction. The input excitation is usually applied at a single location and can be monitored. Tests with measured inputs are usually conducted on small structures, where mechanical tools are capable to generate significant excitations. Second, Operational Modal Analysis (OMA), also known as output-only modal analysis, is able to perform modal analysis without knowing and/or controlling the input excitation. This method is still capable of estimating the same modal parameters as the traditional EMA techniques. In such cases, ambient vibration becomes the only source of excitation on the structure (more practical for larger structures). OMA makes use of ambient environment effects such as wind, traffic and pedestrian loads as excitation forces.

In this work, OMA was employed and the tests were conducted using the ambient excitation and recording the response of the structure through twelve accelerometers placed along the entire deck's length.

To analyze the data acquired during the test, two numerical algorithms have been implemented, that are able to provide the required dynamic characteristics: the Peak-Picking Method (PP) and the Natural Excitation Technique combined with Eigensystem Realization Algorithm (NExT-ERA). Both algorithms allow the identification of dynamic characteristics of the structure starting from the output recorded using accelerometers. The Peak-Picking uses the output produced in the frequency domain, by identifying the peaks in the form of the FRF (frequency response function) for the determination of natural frequencies of the structure. The NExT-ERA analyzes the output directly in the time domain and allows, through the resolution of a system eigenvalue / eigenvectors, obtaining the dynamic characteristics in a totally automatic way. By the structural identification, the behavior of the structure in the dynamic field can be entirely understood.

The project involves the construction of a future continuous monitoring system with the intent of providing information on the state of the structure during its life, to identify the presence of any damages or problems that might compromise the integrity of functional or structural. Furthermore, the information generated by this system will provide the basis for the planning of adequate maintenance work which prevents the occurrence of possible danger and to safeguard the structural integrity over time.

The results of the experiments have been validated through the realization of numerical analysis obtained by creating a finite element model of the structure. It has helped to avoid the experimental analysis results to be affected by blunders. Once the accuracy of the results has been verified, they were used as a starting point for calibrating and updating of finite element model, so that it could simulate the actual behavior of the structure as accurately as possible.

The first chapter presents the Dowling Hall footbridge, presenting the geometric and structural characteristics. Then, we analyze the choice made regarding the instrumentation adopted for data acquisition gathered during testing, with the justification of the specific characterization of each element of the data acquisition system. Following in the chapter, the dynamic tests have been described, their design, planning and implementation with the detailed explanation of the position of sensors and ways of performing each test. Chapter two is focused on the raw data processing. The data are first processed in order to obtain a good quality signal analysis by adopting suitable tools for signal analysis. In the third chapter, the analysis results have been elaborated, collected and compared, highlighting the peculiarities of different algorithms for both tests performed. In the last chapter, the results of experimental were compared with those derived from the analysis done by a finite element computer model, which has been refined and perfected according to the results of the experiment. This allows checking the goodness of the model used in the design phase and allows assessing the need for possible interventions of structural adjustment. Finally, we analyze the design solutions for the creation of continuous monitoring system employing ambient excitation that will be able to provide data regarding the dynamic characteristics of the structure.

This work has allowed to analyze and evaluate all phases affecting the design and implementation of a system for identifying the dynamic characteristics of the structure from the choice of instrumentation required, and the design and implementation of preliminary dynamic tests, choice, implementation and adequacy of algorithms that allow to understand the behavior of the structure in the dynamic field and to design appropriate design solutions for deployment of sensors and instrumentation required. This work provides the basis for an appropriate design and implementation of the monitoring system that will be designed for the continuous monitoring of Dowling Hall footbridge in the near future.

1. *TESTS*

Full-scale dynamic testing of structures can provide valuable information on the service behavior and performance of structures. With the growing interest in the structural condition of civil structures in general, and bridges in particular, dynamic testing can be used as a tool for assessing their integrity. From the measured dynamic response, induced by ambient or forced excitation, modal parameters (e.g. natural frequencies, mode shapes and modal damping values) and system parameters (stiffness, mass and damping matrices) can be obtained. These identified parameters can then be used to characterize and monitor the performance of the structure. Analytical models of the structure can also be validated using these parameters.

This section describes the set of dynamic tests performed on the Dowling Hall footbridge on April 4, 2009 and on June 4, 2009. The following chapter presents the description of the bridge's structure characteristics, the information regarding the instrumentation employed in the data acquisition processes and all the design and implementation steps for the two dynamic tests.

1.1 The Dowling Hall footbridge

Figure 1.1 shows the Dowling Hall footbridge, which is located in the Tufts University main campus area, in Medford, MA.

The bridge connects the 7th floor of the Dowling Hall building with the Tufts main campus area, allowing people to transfer from the parking structure to the main campus. The bridge is a continuous two-span steel frame with concrete slab deck. It is supported by a central pier placed in the middle of the structure’s length, a pier closes the Dowling Hall building and a concrete support, linking the Tufts main campus side directly to the ground.

The Dowling Hall footbridge has a total length of 43.80m and a width of 3.20m, with two symmetric spans. The bridge is equipped with a heated deck system in order to avoid the snow accumulation during the winter months.

Figure 1.1 The Dowling Hall footbridge

1.2 Instrumentation

The instrumentation employed during the dynamic tests included 12 accelerometers, a data acquisition device and a laptop, which allowed us to measure the bridge's ambient acceleration response.

PCB Piezotronics 393B04 model accelerometers, which are shown in Figure 1.2, were used to measure the bridge acceleration response. The sensors' characteristics are shown in Table 1.

Table 1 PCB accelerometers properties

Flexural ICP acceleration	1000 mV/g
Sensitivity	±10%
Broadband resolution	(1 to 10000 Hz) 0.000003 g rms
Measurement range	±5 g
Frequency range	(±5%) 0.06 to 450 Hz
Electrical connector	10-32 coaxial jack
Weight	1.8 oz (50 gm)

The data acquisition system consisted of two parts: the National Instruments (NI) USB-9234 modules, which are shown on the right side of Figure 1.2 and the National Instruments cDAQ 9172 chassis, which is shown in Figure 1.3.

Figure 1.2 PCB Piezotronics 393B04 accelerometer (left), NI USB-9234 module (right)

NI USB-9234 is a 4-Channel, ±5 V, 24-Bit software-selectable IEPE and AC/DC analog input module which provides the accelerometers connection. The NI USB-9234 includes an internal master timebase with a frequency of 13.1072 MHz. The frequency of a master timebase (f_M) controls the data rate (f_s) of the NI USB-9234. The following Equation (1.1) provides the available device data rates:

$$f_s = \frac{f_M \div 256}{n} \tag{1.1}$$

where n is an integer between 1 and 31. According to Equation (1.1), the acceptable sampling frequency rates are 51.2 kHz, 25.6 kHz, 17.067 kHz, and so on down to 1.652 kHz, depending on the value of n. A manageable 2.048 kHz sampling rate was selected for data acquisition.

Figure 1.3 NI cDAQ-9172 chassis

The NI cDAQ-9172, shown in Figure 1.3, is an eight-slot USB chassis designed for use with I/O modules. The NI cDAQ-9172 chassis is capable of measuring a broad range of analog and digital I/O signals and sensors using a Hi-Speed USB 2.0 interface. Labview Signal Express 3.0 software was used to record the data.

1.3 Dynamic tests performed

1.3.1 April test

On April 4 2009, a set of five dynamic tests were performed on the Dowling Hall footbridge in order to identify its modal parameters (natural frequencies, damping ratios and mode shapes). Figure 1.6 shows the instrumentation employed during the tests.

Twelve accelerometers were placed in different positions on the north and the south sides of the bridge, symmetrically about the centre of the structure as shown in Figure 1.5. The arrangement of sensors has been chosen referring to the mode shapes proposed by the theory of structures dynamic. In order to obtain the measurements for each sensor on at least the first three vibration modes, accelerometers position have been referred to the theoretical framework of the deformation in the dynamic field of a symmetrical beam on three supports, so as to avoid the nodes, where the displacements are zero and therefore the accelerations. Figure 1.4 shows the first two theoretical dynamic deflections for a continuous beam and the sensors locations, selected in order to provide significant results during the dynamic tests.

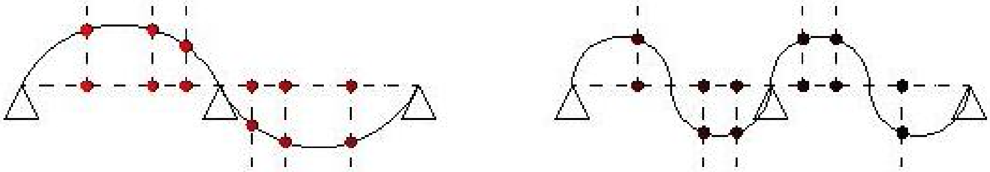

Figure 1.4 Sensors locations showing dynamic deformations

Sensors placement on the structure's deck was preceded by the study of the dynamic characteristics of plates that make up the concrete slab. This analysis is necessary to identify the natural frequencies of concrete elements and avoid the mistake with the results relative to the whole structure. The study was conducted on a plate type, since all elements have the same size and subject to the same degree of restraint. The frequencies were found to be higher than that of the steel structure of the bridge, with the first natural frequency around 16 Hz and higher frequencies greater than 30 Hz. This observation has led to correctly identify the natural frequencies of the bridge without interference by concrete elements.

The accelerometers were set as close as possible to the steel trusses, on the outer sides of the slabs of concrete, so that they do not affect the detection frequencies of the steel structure. Furthermore, the sensors were placed in correspondence of the horizontal steal currents, near the junction with the main structure, to improve the detection of the steal frame frequencies.

In order to provide a tight connection between the sensors and the concrete slabs, aluminum angular brackets were firmly fixed to the concrete deck using a fast-setting two-part epoxy cement. The brackets were machined to accept the mounting stud of the accelerometer. Then, the accelerometers were screwed into the brackets.

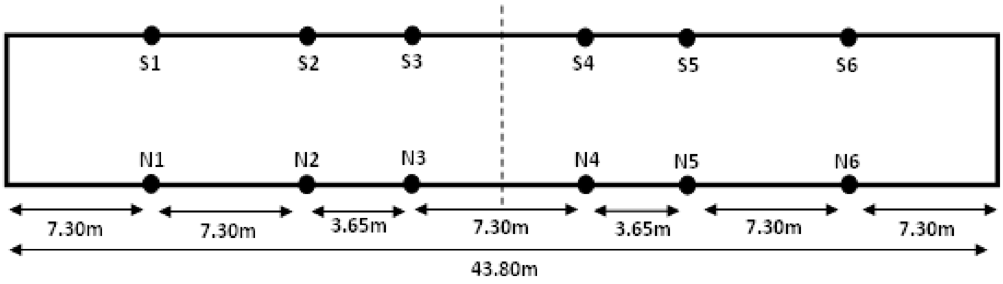

Figure 1.5 April test sensors layout along the bridge deck

The five tests have been performed by exciting the structure with pedestrian traffic and people jumping in various positions along the bridge deck, together with wind excitation. Two sensors configurations were selected in order to measure both vertical and horizontal components of the bridge acceleration response:

1. The vertical configuration, consisting of all the twelve sensors measuring vertical accelerations
2. The horizontal-vertical configuration, employing the six south side (S) sensors measuring vertical accelerations and the six north side (N) sensors measuring horizontal accelerations.

The five tests were performed in succession, using a sampling rate of 2.048 kHz imposed by instrumentation, and an acquisition time of 300 seconds, maximum time allowed by the acquisition software used, resulting in 614,400 samples per channel. A high acquisition time was required to achieve high definition signal in the frequency domain, resulting in the distance between two points in the frequency domain (df) is inversely proportional to the total time of acquisition.

Preparation for the test began on the afternoon of April 3rd with cementing of the steel brackets to the bridge deck. This was done to allow overnight curing of the epoxy and avoid setting up in the rain which was predicted for the following morning.

Final preparations for the test were finished on the morning of June 4th, including installation of all sensors, cable connections, and data acquisition hardware. The actual test was conducted between 12:00 and 14:30. Weather conditions at the time of the test were cloudy and quite raining, with moderate wind and a temperature of 10° to 13° C.

The description of the five tests is presented:

1. Test 1 consisted of recording the accelerations of the structure caused by wind and pedestrian excitation, using the vertical accelerometers configuration.
2. During Test 2, the bridge was excited by wind, pedestrian traffic and people jumping in different locations along the bridge deck. The test was performed using vertical accelerometers configuration.
3. Test 3 was conducted in the same excitation conditions as Test 1, still using vertical accelerometers configuration.
4. Test 4 consisted of recording the accelerations of the structure caused by wind and pedestrian excitation, using the vertical-horizontal accelerometers configuration.
5. During Test 5, the bridge was excited by wind, pedestrian traffic and people jumping in different locations along the bridge deck. The test was performed using vertical-horizontal accelerometers configuration.

Figure 1.6 April test data acquisition system and bridge instrumentation

1.3.2 June test

On June 4 2009, a second set of five dynamic tests were performed on the Dowling Hall footbridge, starting from the results of April test.

The objectives of this second test were to: 1) quantify motion at the supporting piers; 2) gather more data on the horizontal motion of the bridge; 3) detect any significant axial motion. Accelerometers were laid out as shown in Figure 1.7.

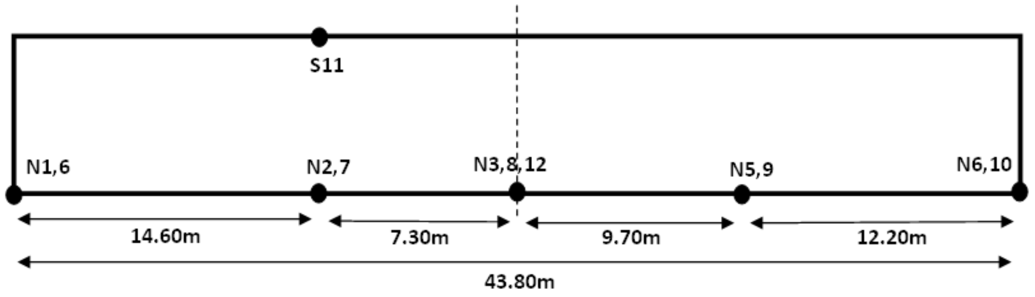

Figure 1.7 June test sensors layout along the bridge deck

Twelve accelerometers were placed in different positions on the north and the south sides of the bridge. The arrangement of sensors has been chosen in order to provide accelerations at the three supports location. A reference sensor (N5,9) has been placed in the same position of the April test, so that a comparison and calibration of the data from the two tests was possible.

The accelerometers were set as close as possible to the steel trusses, on the outer sides of the slabs of concrete, so that they do not affect the detection frequencies of the steel structure. Furthermore, the sensors were placed in correspondence of the horizontal steal currents, near the junction with the main structure, to improve the detection of the steal frame frequencies.

In order to provide a tight connection between the sensors and the concrete slabs, aluminum angular brackets were firmly fixed to the concrete deck using a fast-setting two-part epoxy cement. The brackets were machined to accept the mounting stud of the accelerometer. Then, the accelerometers were screwed into the brackets.

The five tests have been performed by exciting the structure with pedestrian traffic and people jumping in various positions along the bridge deck, together with wind excitation. Sensors configurations were selected in order to measure both vertical and horizontal components of the bridge acceleration response for all the accelerometers locations. An axial component configuration accelerometer (N12) was places at the center pier. Finally, one accelerometer (S11) was fixed with the vertical configuration on the south side, corresponding to the N2,7 sensors on the north side, in order to get the acceleration at the same horizontal coordinates of the bridge.

The five tests were performed in succession, using a sampling rate of 2.048 kHz imposed by instrumentation, and an acquisition time of 300 seconds, maximum time allowed by the acquisition software used, resulting in 614,400 samples per channel. A high acquisition time was required to achieve high definition signal in the frequency domain, resulting in the distance between two points in the frequency domain (df) is inversely proportional to the total time of acquisition.

Preparation for the test began on the afternoon of June 3rd with cementing of the steel brackets to the bridge deck. This was done to allow overnight curing of the epoxy and avoid setting up in the rain which was predicted for the following morning.

Final preparations for the test were finished on the morning of June 4th, including installation of all sensors, cable connections, and data acquisition hardware. The actual test was conducted between 11:00 and 12:30. Weather conditions at the time of the test were sunny and dry, with low wind and a temperature of 25° to 27° C.

The description of the five tests is presented:

1. Test 1 consisted of recording the accelerations of the structure caused by 3 minutes with five persons running and jumping across the bridge and 2 minutes with no excitation.
2. During Test 2, the bridge was excited by:
   1 minute: with five persons jumping at the midpoint between the center pier and Dowling Hall;

1 minute: with five persons standing at the midpoint between the center pier and Dowling Hall;

1 minute: five persons moving to the midpoint between the center pier and main campus;

1 minute: five persons jumping at the midpoint between the center pier and main campus;

1 minute: five persons standing at the midpoint between the center pier and main campus;

3. Test 3 was conducted with one person walking/lightly jumping across the bridge for 5 minutes
4. Test 4 consisted of recording the accelerations of the structure caused by:

   1 minute: hammer impacts at 8m from center on campus side (vertical hammer)

   1 minute: hammer impacts at 8m from center on campus side (horizontal hammer)

   1 minute: hammer impacts at 2,5m from center on campus side (vertical hammer)

   1 minute: hammer impacts at 5m from center on Dowling Hall side (vertical hammer)

   1 minute: hammer impacts at 5m from center on Dowling Hall side (horizontal hammer)
5. During Test 5, the bridge was excited with similar conditions employed performing Test 4, with input data from impact hammer added to record as Channel 13.

Figure 1.8 June test data acquisition system and bridge instrumentation

2. *ROW PROCESSING OF EXPERIMETAL DATA*

Before the system identification methods were applied to the measured data, they were filtered and down-sampled.

The down-sampling process allows decreasing the signal's number of samples maintaining the original signal quality. The down-sampled signal is obtained by selecting one sample for every N sample in the signal's time history, where N is the integer number that defines the down-sampling factor. The down-sampling process is performed in order to improve the computational efficiency of data analysis process.

Increasing the integer N, the computation becomes lighter but, at the same time, the down-sampled signal is less accurate. The down-sampling factor has to be determined based on the frequencies of interest.

The sampling frequency, according to the NI 9234 timebase frequency, was assumed equal to 2048 Hz. The highest identifiable frequency is the Nyquist frequency, equivalent to half the sampling rate used. Given the large number of samples collected during each phase of testing, analysis may be computationally expensive. To make the calculation less demanding, a downsampling was performed on data sampled in the time domain, thus reducing significantly the number of samples that make up the single signal and lowering the sampling frequency to values more compatible with the natural frequencies are seeking.

In fact, the maximum frequency detectable in the frequency domain, corresponding to the Nyquist frequency, is assumed to be: $f_d \leq 2B$, where where f_p is the pulse frequency (in pulses per second) and B is the bandwidth (in hertz). The quantity 2B later came to be called the Nyquist rate.

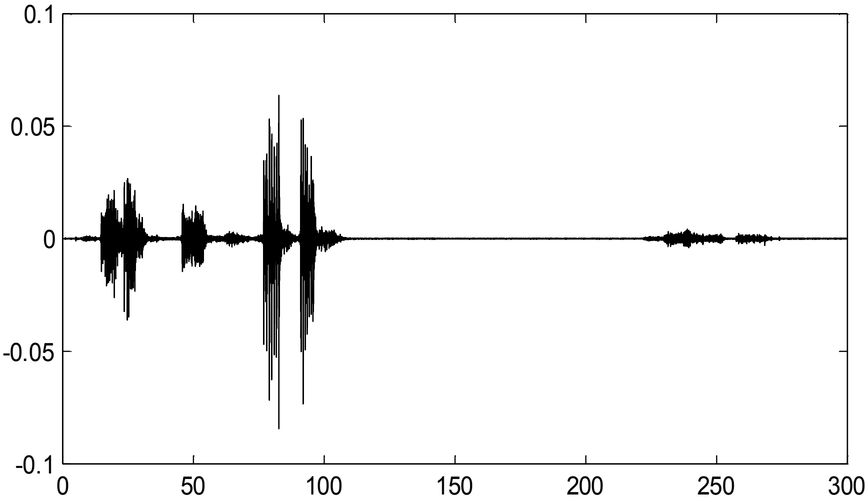

Figure 2.1. Acceleration time history of Channel S2 Test 2

Figure 2.1 shows the acceleration time history at Channel S2 during Test 2, before filtering and down-sampling.

Appendix A presents plots of the time history, Fourier spectra and power spectral density for all the channels and the five tests performed.

2.1 Filtering

Signal filtering is often used in eddy current testing to eliminate unwanted frequencies from the receiver signal. While the correct filter settings can significantly improve the visibility of a defect signal, incorrect settings can distort the signal presentation and even eliminate the defect signal completely. Therefore, it is important to understand the concept of signal filtering.

Figure 2.2 shows the finite impulse response (FIR) band-pass digital filter designed and applied for data filtering. The data filtering process allows selecting the frequency range of interest by designing and applying a digital filter. The three standard filters found in most impedance plane display instruments are:

- the ‘High Pass Filter (HPF);
- the‘Low Pass Filter (LPF);

- the Band Pass Filter’ (BPF), which is an high and low pass filter combination.

The HPF allows high frequencies to pass and filters out the low frequencies. The HPF is basically filtering out changes in the signal that occur over a significant period of time. The LPF allows low frequency to pass and filters out the high frequency. In other words, all portions of the signal that change rapidly (have a high slope) are filtered, such as electronic noise.

The main function of the LPF is to remove high frequency interference noise. This noise can come from a variety of sources including the instrumentation and/or the probe itself. The noise appears as an unstable dot that produces jagged lines on the display as seen in the signal from a surface notch shown in the left image below. Lowering the LPF frequency will remove more of the higher frequencies from the signal and produce a cleaner signal as shown in the center image below. When using a LPF, it should be set to the highest frequency that produces a usable signal. The HPF is used to eliminate low frequencies which are produced by slow changes, such as conductivity shift within a material, varying distance to an edge while scanning parallel to it, or out-of-round holes in fastener hole inspection. The BPF is typically used to isolate the component of a time series that lies within a particular band of frequencies.

Low-pass or band-pass filters with low frequencies ranges are typically used in studying bridges, which are flexible structures characterized by low natural frequencies. A band-pass digital filter with a 2-50 Hz range has been designed for the Dowling Hall footbridge analysis.

FIR, Finite Impulse Response, filters are one of the primary types of filters used in Digital Signal Processing. FIR filters are said to be finite because they do not have any feedback. Therefore, if you send an impulse through the system (a single spike) then the output will invariably become zero as soon as the impulse runs through the filter.

There are a few terms used to describe the behavior and performance of FIR filter including the following:

- Filter Coefficients - The set of constants, also called tap weights, used to multiply against delayed sample values. For an FIR filter, the filter coefficients are, by definition, the impulse response of the filter.

- Impulse Response – A filter's time domain output sequence when the input is an impulse. An impulse is a single unity-valued sample followed and preceded by zero-valued samples. For an FIR filter the impulse response of a FIR filter is the set of filter coefficients.
- Tap – The number of FIR taps, typically N, tells us a couple things about the filter. Most importantly it tells us the amount of memory needed, the number of calculations required, and the amount of "filtering" that it can do. Basically, the more taps in a filter results in better stopband attenuation (less of the part we want filtered out), less rippling (less variations in the passband), and steeper rolloff (a shorter transition between the passband and the stopband).
- Multiply-Accumulate (MAC) – In the context of FIR Filters, a "MAC" is the operation of multiplying a coefficient by the corresponding delayed data sample and accumulating the result. There is usually one MAC per tap.

Reducing the number of taps used in the filter will reduce the number of calculations to process in the signal, however, the quality of the filtering will suffer. Rippling will become more sever, the rolloff will be less steep, and the passband will be less accurate.

The designed FIR filter is characterized by the 2-50 Hz band-pass range frequencies and by the 4096 N-th order, as shown in Figure 2.2.

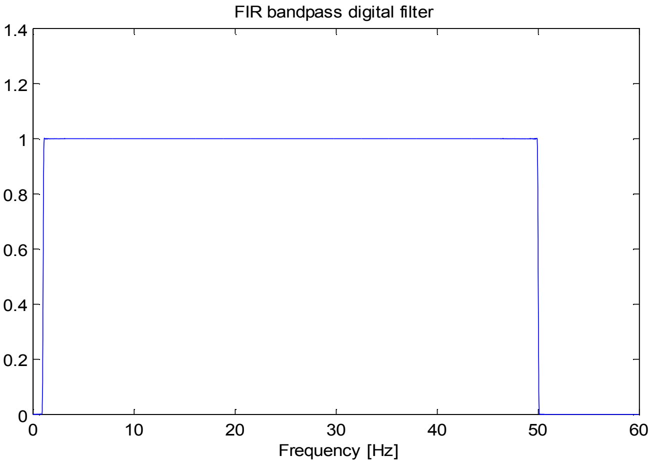

Figure 2.2 FIR band-pass digital filter

The impulse response, the filter's response to a Kronecker delta input, is finite because it settles to zero in a finite number of sample intervals. This is in contrast to infinite impulse response (IIR) filters, which have internal feedback and may continue to respond indefinitely. The impulse response of an Nth-order FIR filter lasts for N+1 samples and then dies to zero. The FIR digital filter is real and has linear phase.

Figure 2.3 shows the effect of the digital filter on a Fourier amplitude spectrum.

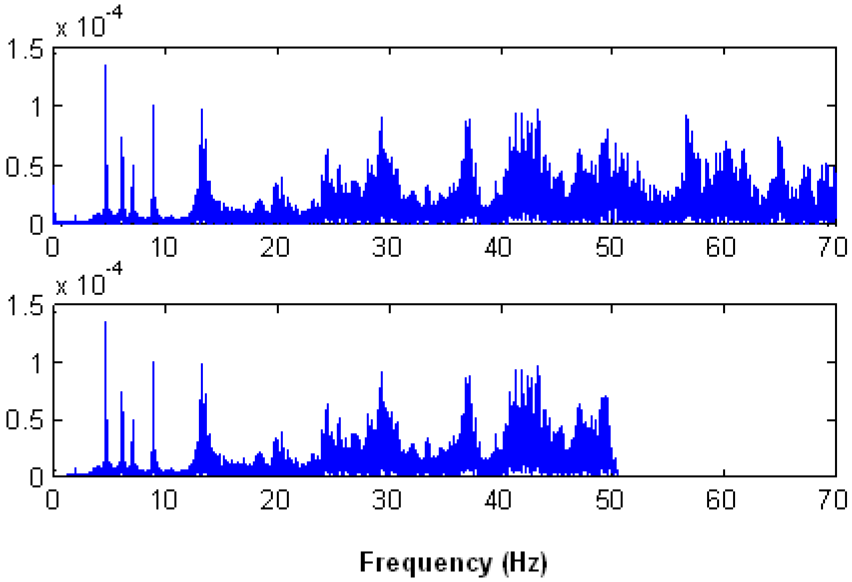

Figure 2.3 Fourier amplitude spectra of Channel S2 during Test 2, before and after filtering

Figure 2.3 shows a Fourier spectrum sample before and after the FIR digital filter application.

2.2 Down-Sampling

The data down-sampling process allows the number of samples reduction in signal’s time history by picking one sample from every N, where N is a real integer usually called down-sampling factor. The down-sampling factor N is selected such that the down-sampled Nyquist

Frequency is still larger than the frequency range of interest. In addition, low-pass filters should be applied to the data before down-sampling in order to avoid aliasing. In this work the down-sampling factor has been selected equal to 8, corresponding to a down-sampled signal eight times smaller than the original one. However, the quality of the “new” signal is still acceptable as shown in Figure 2.4. The down-sampling process allows working with less data without compromising the signal quality.

According with the N value, sampling rate has been reduced from 2.048 kHz to 256 Hz, corresponding to a samples decreasing from 614,400 to 78,600 samples for each channel.

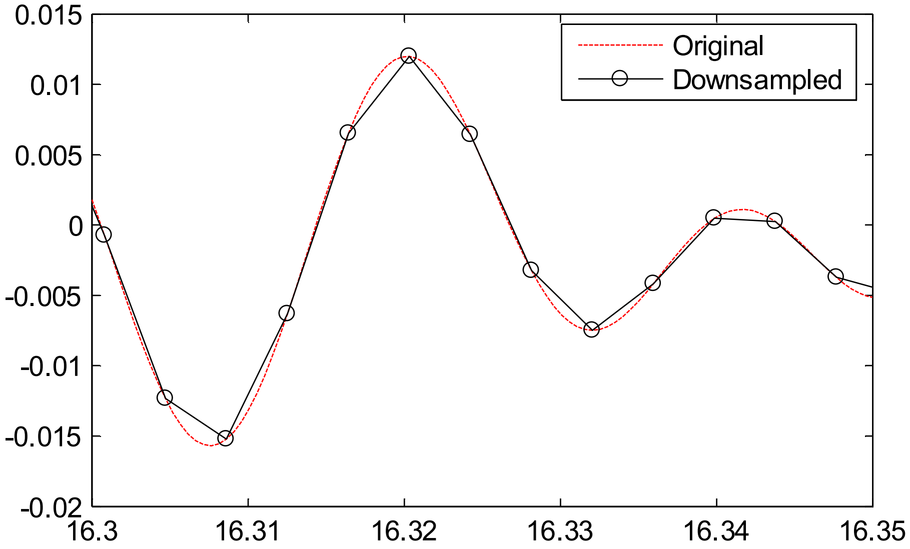

Figure 2.4 Original and the down-sampled signal.

If the sampling condition given by the Nyquist-Shannon sampling theorem is not satisfied, adjacent copies overlap, and it is not possible in general to discern an unambiguous signal. Any frequency component above is indistinguishable from a lower-frequency component, called an alias, associated with one of the copies. Aliasing refers to an effect that causes different signals to become indistinguishable (or aliases of one another) when sampled.

For a sinusoidal component of exactly half the sampling frequency, the component will in general alias to another sinusoid of the same frequency, but with a different phase and amplitude.

To prevent or reduce aliasing, two things can be done:

- Increase the sampling rate, to above twice some or all of the frequencies that are aliasing.
- Introduce an anti-aliasing filter or make the anti-aliasing filter more stringent.

2.3 Fourier transform and Power Spectral Density

Non-sinusoidal periodic signals are made up of many discrete sinusoidal frequency components (see applet Fourier Synthesis of Periodic Waveforms). The process of obtaining the spectrum of frequencies *H(f)* comprising a time-dependent signal h(t) is called Fourier Analysis and it is realized by the so-called Fourier Transform (FT). A single square pulse or an exponentially decaying sinusoidal signal are typical examples of non-periodic signals, of finite duration. Even these signals are composed of sinusoidal components but not discrete in nature, i.e. the corresponding *H(f)* is a continuous function of frequency rather than a series of discrete sinusoidal components

The traditional approach to a modal parameters identification process consists of detecting the natural frequencies directly from peaks in the signal's Fourier amplitude spectra. The signal is generally acquired in time domain (signal time history) and then transformed into its corresponding frequency domain. The Fourier transform (FT) is a widely used mathematical tool to get this transformation.

The periodic signals, i.e. if $x\ (t)\ =\ x\ (t\ +\ T_0)$ for each instant of time t, since T_0 is the period, can be written as a sum, usually finite, of harmonic functions through the Fourier series:

$$x(t) = \sum_{k=-\infty}^{\infty} X_k(\omega) e^{jk\omega t} \tag{2.1}$$

where the coefficients X_k are derived from the following expression (2.2):

$$X_k(\omega) = \frac{1}{T_0} \int_{-\frac{T_0}{2}}^{\frac{T_0}{2}} x(t) \cdot e^{-jk\frac{2\pi}{T_0}t} \mathrm{d}t \tag{2.2}$$

The Fourier transform is a generalization of the Fourier series to the case where the function *x(t)* is not periodic (i.e. infinite period). The Fourier transform of a function *x(t)* is given by the (2.3):

$$X_k(\omega) = \int_{-\infty}^{\infty} x(t) \cdot e^{-j\omega t} \mathrm{d}t \tag{2.3}$$

To calculate the Fourier coefficient corresponding to the *k-th* harmony through discrete steps *Δt*, should approximate formula (2.2) as follows:

$$X_k = \frac{1}{N\Delta t} \sum_{n=0}^{N-1} x(n\Delta t) \cdot e^{-jk\frac{2\pi}{N\Delta t}n\Delta t} \tag{2.4}$$

where the summation term is the fast Fourier transform (FFT) or discrete transform. The discrete Transforms produce Fourier spectra consist of values in which each can be thought as the output of a filter centered at frequency ω.

The autocorrelation function for a generic signal *x(t)* is:

$$R_{xx}(\tau) = \lim_{T\to\infty} \frac{1}{T} \int_0^T x(t)x(t+\tau)\mathrm{d}t \tag{2.5}$$

showing the correlation of a signal to itself. The autocorrelation of a periodic function is periodic, while the autocorrelation of a random signal tends to zero for nonzero τ. The Fourier transform of the autocorrelation function $R_{xx}(\tau)$ is that power spectral density (PSD), or autospettrum, defined as:

$$S_{xx}(\omega) = \int_{-\infty}^{+\infty} R_{xx}(\tau) e^{-j2\pi\omega\tau} d\tau \tag{2.5}$$

Function $S_{xx}(\omega)$ is related to the Fourier transform $X(\omega)$ of $x(t)$ by report:

$$S_{xx}(\omega) = X(\omega)^* X(\omega) \tag{2.6}$$

where $X(\omega)^*$ indicates the complex conjugate of $X(\omega)$. It is a real function and contains information on the frequencies present in $x(t)$ but not those on the phases, as obtained from the only form. $X(\omega)$. The cross-correlation (or cross-correlation) function of two signals $x(t)$ and $y(t)$ is defined as:

$$R_{xy}(\tau) = \lim_{T \to \infty} \frac{1}{T} \int_0^T x(t) y(t+\tau) \mathrm{d}t \tag{2.7}$$

and indicates how the two signals are correlated. Fourier transform function of cross-correlation R_{xy} is called cross-spectrum (CSD) and is usually indicated by $S_{xy}(\omega)$:

$$S_{xy}(\omega) = \int_{-\infty}^{+\infty} R_{xy}(\tau) e^{-j2\pi\omega\tau} \mathrm{d}\tau \tag{2.8}$$

Function $S_{xy}(\omega)$ is related to the Fourier transform of $x(t)$ and $y(t)$ by the expression:

$$S_{xy}(\omega) = X(\omega)^* Y(\omega) \tag{2.9}$$

that is a complex function containing information both on frequencies and phases.

Through the FFT, the frequency domain shows the signal’s frequency content, allowing the direct natural frequencies detection. The signal can also be analyzed into its frequency domain by using the power spectral density (PSD), providing the representation of the frequencies power content. Using PSD, the signal can be averaged through the windowing process in order to provide smoother plots as shown in Figure 2.6

.

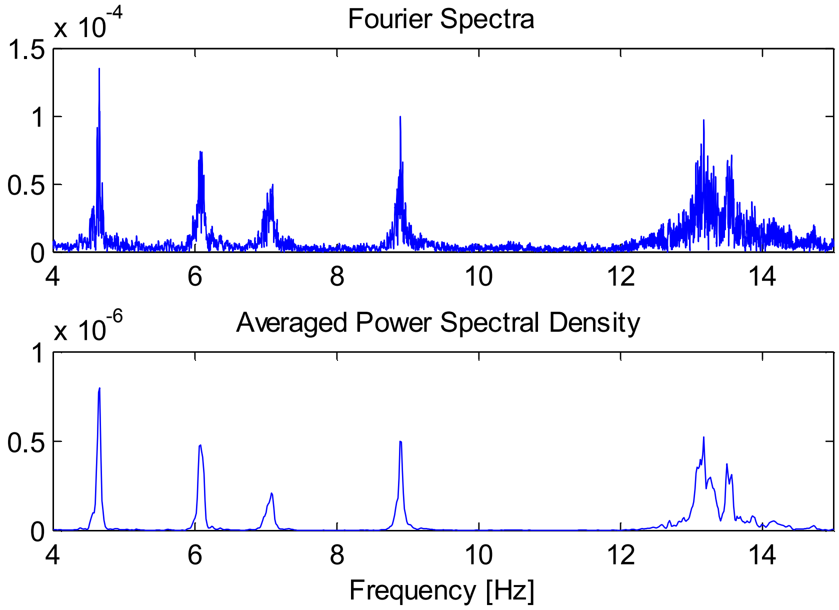

Figure 2.5 Fourier spectra and averaged PSD. of Channel S2 during Test 2.

The purpose of the window function is to reduce side-lobe level in the spectral density estimate, at the expense of frequency resolution, exactly as in the case of sinusoidal spectrum analysis.

Welch's method is based on the concept of using periodograms, which converts a signal from the time domain to the frequency domain.

The Welch method develops in the following steps:

- The signal is split up into overlapping segments. The original data segment is split up into L data segments of length M, overlapping by D points.
  If $D = M/2$, the overlap is said to be 50%
  If $D = 0$, the overlap is said to be 0%.
- The overlapping segments are then windowed. After the data is split up into overlapping segments, the individual L data segments have a window applied to them (in the time domain). Most window functions afford more influence to the data at the center of the set than to data at the edges, which represents a loss of information. To mitigate that loss, the individual data sets are commonly overlapped in time (as in the above step).

The windowing of the segments is what makes the Welch method a "modified" periodogram.

The periodogram is calculated by computing the discrete Fourier transform, and then computing the squared magnitude of the result. The individual periodograms are then time-averaged, which reduces the variance of the individual power measurements.

A window function is a function that is zero-valued outside of some chosen interval. For instance, a function that is constant inside the interval and zero elsewhere is called a rectangular window, which describes the shape of its graphical representation. When another function or a signal (data) is multiplied by a window function, the product is also zero-valued outside the interval: all that is left is the view through the window.

The generalized Hamming family of windows is constructed by adding one period of a cosine function to the rectangular window. The benefit of adding the cosine segment is lower side lobes. An example of Hamming window representation in time domain is shown in Figure 2.6.

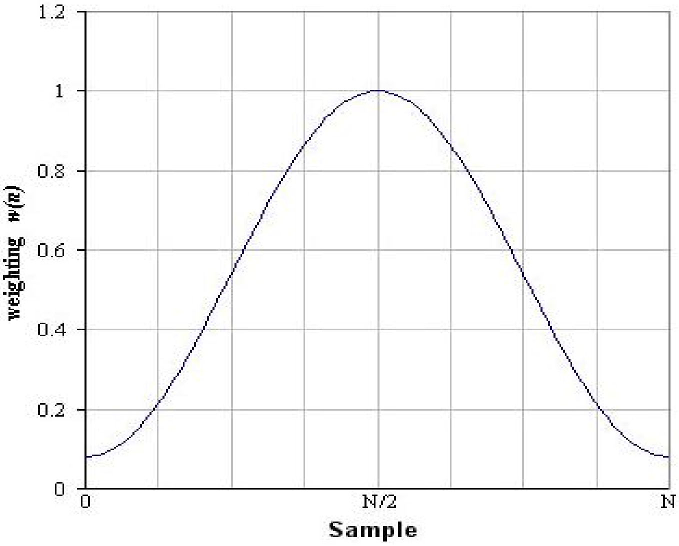

Figure 2.6 Hamming window

In this work the power spectral density has been computed using Welch's method. Windowing is applied by 9600 points (N) Hamming windows with 50% overlap resulting in a frequency resolution of $\Delta f = 0.016$ Hz.

3. *MODAL ANALYSIS*

System identification using output-only ambient response was originally performed in frequency domain. The method of selecting peaks in frequency domain of spectral density is generally called the Peak Picking method (Bernat & Piersol, 1993) and has been used extensively in classical modal analysis based on ambient excitation. Several techniques were later developed to facilitate an automatic 'picking' procedure, such as frequency domain decomposition using singular value decomposition of power spectral density. However, in practice the classical identification techniques that use spectral analysis give reasonable estimates of natural frequencies and mode shapes only if the modes are well separated. Natural Excitation Technique (NExT) (James et al. 1993) combined with Eigensystem Realization Algorithm (ERA) (Juang and Pappa 1985) have been frequently used for modal identification of structures. NExT-ERA has been successfully applied to structural identification based on ambient excitation (He et al. 2009; Farrar and James 1997). In this section the Peak Picking method and the NExT-ERA are briefly reviewed and their modal identification results are presented.

3.1 Peak Picking

Ambient excitation testing does not directly lend itself to FRFs or IRFs calculations because the input forces are not measured. In the paper two modal parameter identification methods that can deal with ambient vibration measurements are implemented. The first is a rather simple Peak-Picking (PP) method. Though it has some theoretical drawbacks, the Peak-Picking method is probably the most widely used method in civil engineering because of its simplicity.

3.1.1 Method

The Peak-Picking method (Bendat and Piersol 1993) is the simplest known method for identifying the modal parameters of civil engineering structures subjected to ambient vibration loading.

The method leads to reliable results provided that the basic assumptions of low damping and well-separated modes are satisfied. In fact, when a lightly damped structure is subjected to a random excitation, the output ASD at any response point (and the CSD amplitude between any two measurement points) will reach a maximum at frequencies where either the excitation spectrum peaks or the frequency response function of the structure peaks. Since narrow-band peaks in the frequency response function of lightly damped mechanical systems occur at the frequencies corresponding to system normal modes (resonance frequencies), peaks in the ASDs and CSDs can be generally assumed to represent either peaks in the excitation spectrum or normal modes of the structure. In order to identify the output spectral peaks which are due to vibration modes, it has to be recalled that all points on a structure responding in a lightly damped normal mode of vibration will be either in phase or 180° out of phase with one another; hence, for well-separated modes, the spectral matrix can be approximated in the neighbourhood of a resonant frequency f_r as a rank-one matrix:

$$\mathbf{G}(f_r) \cong \alpha_r \boldsymbol{\phi}_r \boldsymbol{\phi}_r^H \tag{3.1}$$

where α_r is a scale factor depending on the damping ratio, the natural frequency, the modal participation factor and the excitation spectra.

Equation (3.1) highlights that:

1. each row or column of the spectral matrix at a resonant frequency f_r can be considered as an estimate of the mode shape φ_r at that frequency;

2. the square-root of the diagonal terms of the spectral matrix at a resonant frequency f_r can be considered as an estimate of the mode shape φ_r at that frequency.

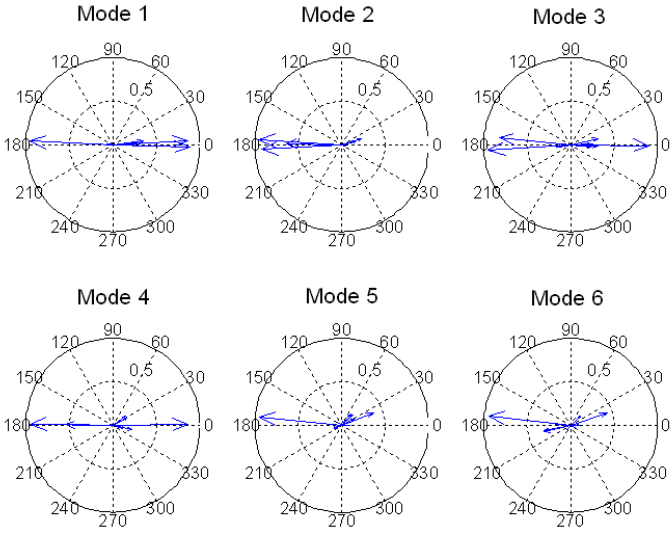

Figure 3.1 Complex modes representation

The corresponding modal damping ratios can be estimated based on half-power bandwith as shown in Equation (3.2).

$$\xi_i = \frac{\omega_{2,i} + \omega_{1,i}}{2\omega_{n,i}} \tag{3.2}$$

where $\omega_{n,i}$ is the i-th natural frequency, $\omega_{1,i}$ and $\omega_{2,i}$ are the frequencies corresponding to magnitude of $H/\sqrt{2}$, where H is the value of the peak Fourier amplitude spectra at the i-th natural frequency. Identified damping from Equation (3.2) depends on the shape of the Fourier spectrum plot (i.e. the sharper the peak is, the smaller is the structure's damping).

In the present application of the PP method, natural frequencies were identified from resonant peaks in the ASDs and in the amplitude of CSDs, for which the cross-spectral phases are 0 or π. The mode shapes were obtained from the amplitude of square-root ASD curves while CSD phases were used to determine directions of relative motion. Drawbacks of the PP method (Abdel-Ghaffar and Housner 1978) are related to the difficulties in identifying closely spaced modes and damping ratios.

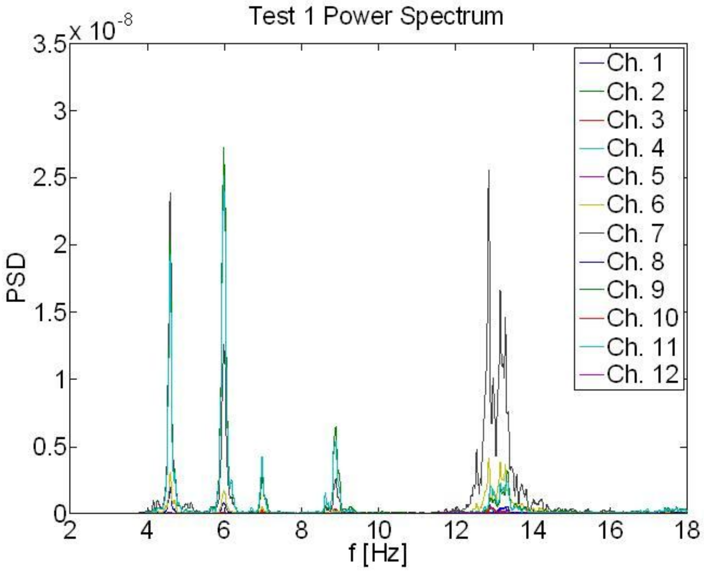

Figure 3.2 Power Spectra example

In the context of ambient vibration measurements the FRF is only replaced by the auto spectra of the ambient outputs. In such a way the natural frequencies are simply determined from the observation of the peaks on the graphs of the averaged normalized power spectral densities (ANPSDs). The ANPSDs are basically obtained by converting the measured accelerations to the frequency domain by a discrete Fourier transform (DFT).

Although the input forces are not measured in ambient vibration testing, this problem has often been circumvented by adopting a derived modal parameter identification technique where the reference sensor (base station) signal is used as an “input” and the FRFs and coherence functions are computed for each measurement point with respect to this reference sensor. It not only helps in the identification of the resonances, but also yields the operational shapes that are not the mode shapes, but almost always correspond to them. The coherence function computed for two simultaneously recorded output signals has values close to one at the resonance frequencies because of the high signal-to-noise ratio at these frequencies. Consequently inspecting the coherence function may assist to select the frequencies. In current Peak-Picking method, the components of the mode shapes are determined by the values of the transfer functions at the natural frequencies. Note that in the context of ambient testing, transfer function does not mean the ratio of response over input force, but rather the ratio of response measured by a roving sensor over response measured by a reference sensor. So every transfer function yields a mode shape component relative to the reference sensor. Here it is assumed that the dynamic response at resonance is only dominated by one mode. The validity of this assumption increases as the modes are better separated and as the damping in the structure is lower.

The Peak-Picking is a kind of frequency domain based technique. Frequency domain algorithms are most popular, mainly due to their simplicity and processing speed, and also for historical reasons. These algorithms, however, involve averaging temporal information, thus discarding most of their details.

Peak-picking technique has some theoretical drawbacks:

- Picking the peaks is always a subjective task;
- Operational deflection shapes are obtained instead of mode shapes;
- Only real modes or proportionally damped structures can be deduced by the method;
- Damping estimates are unreliable.

In spite of these drawbacks many civil engineering cases exist where the eak-picking technique is successfully applied. The popularity of the method is due to its implementation simplicity and its speed.

3.1.2 Identification results

Table 3.1 and Table 3.2 present the natural frequencies and the damping ratios of the six identified modes for each of the 4 April and 4 June five tests, respectively. The modes frequencies have been compared using the coefficient of variation (C_v), defined as: $C_v = \sigma/\mu$. It is a normalized measure of dispersion of a probability distribution. The small coefficient of variation (C_v) for the identified natural frequencies indicates the accuracy of these estimates. However, the same accuracy is not found for the damping ratios. The C_v of the natural frequency estimates are in the range of 0,13-1,6%, while the corresponding coefficient for damping ratios are in the range 0,42-1,09%. However, these identified damping values provide an estimation of the structure's damping. Table 3.1 put in evidence the accuracy of the system identification method, showing precise results especially for Mode 1 and Mode 3, the first vertical deflection and torsional modes respectively.

Table 3.1 April tests Peak Picking identification results

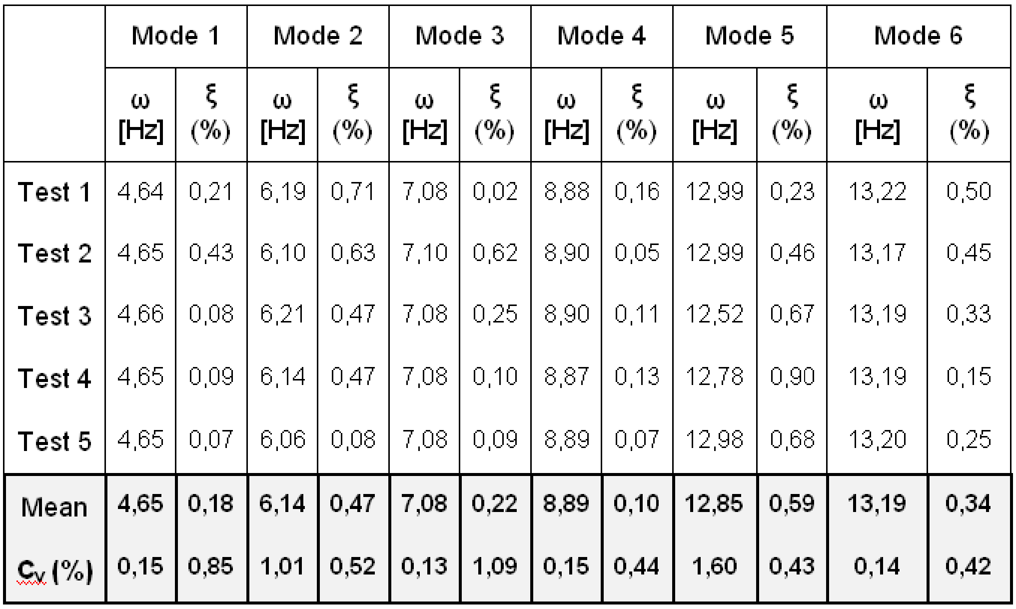

	Mode 1		Mode 2		Mode 3		Mode 4		Mode 5		Mode 6	
	ω [Hz]	ξ (%)	ω [Hz]	ξ (%)	ω [Hz]	ξ (%)	ω [Hz]	ξ (%)	ω [Hz]	ξ (%)	ω [Hz]	ξ (%)
Test 1	4,64	0,21	6,19	0,71	7,08	0,02	8,88	0,16	12,99	0,23	13,22	0,50
Test 2	4,65	0,43	6,10	0,63	7,10	0,62	8,90	0,05	12,99	0,46	13,17	0,45
Test 3	4,66	0,08	6,21	0,47	7,08	0,25	8,90	0,11	12,52	0,67	13,19	0,33
Test 4	4,65	0,09	6,14	0,47	7,08	0,10	8,87	0,13	12,78	0,90	13,19	0,15
Test 5	4,65	0,07	6,06	0,08	7,08	0,09	8,89	0,07	12,98	0,68	13,20	0,25
Mean	**4,65**	**0,18**	**6,14**	**0,47**	**7,08**	**0,22**	**8,89**	**0,10**	**12,85**	**0,59**	**13,19**	**0,34**
C_v (%)	**0,15**	**0,85**	**1,01**	**0,52**	**0,13**	**1,09**	**0,15**	**0,44**	**1,60**	**0,43**	**0,14**	**0,42**

Results from 4 June test are collected in Table 3.2. Data show a good correlation between the six modes identified, with best results for Mode 1 and Mode 3 as the 4 April test results. The influence of the ambient factor can be recognize, in particular the temperature effect on the structure's stiffness variation. The natural frequencies identified on the 4 June test are smaller than the natural frequencies identified on the 4 April test. This fact is due to a warmer temperature on the June test day that provides a less structure's stiffness and so smaller natural frequencies. However, both results from the two tests are really close one to the other, showing the good efficiency of the instrumentation and of the system identification process employed.

Table 3.2 June tests Peak Picking identification results

	Mode 1		Mode 2		Mode 3		Mode 4		Mode 5		Mode 6	
	ω [Hz]	ξ (%)	ω [Hz]	ξ (%)	ω [Hz]	ξ (%)	ω [Hz]	ξ (%)	ω [Hz]	ξ (%)	ω [Hz]	ξ (%)
Test 1	4,58	0,64	5,98	0,95	6,97	0,02	8,89	0,55	12,69	0,40	13,20	0,94
Test 2	4,59	1,31	5,89	0,85	6,99	0,76	8,91	0,17	12,69	0,79	13,15	0,84
Test 3	4,60	0,24	6,00	0,63	6,97	0,31	8,91	0,38	12,23	1,16	13,17	0,62
Test 4	4,59	0,27	5,93	0,63	6,97	0,12	8,88	0,44	12,49	1,55	13,17	0,28
Test 5	4,59	0,21	5,85	0,11	6,97	0,11	8,90	0,24	12,68	1,17	13,18	0,47
Mean	**4,59**	**0,54**	**5,93**	**0,63**	**6,97**	**0,27**	**8,90**	**0,35**	**12,56**	**1,02**	**13,17**	**0,63**
C_V (%)	**0,15**	**0,87**	**1,05**	**0,52**	**0,13**	**1,10**	**0,15**	**0,44**	**1,60**	**0,43**	**0,14**	**0,43**

Figure 3.2 presents the identified mode shapes corresponding to the six identified modes reported in Table 3.2

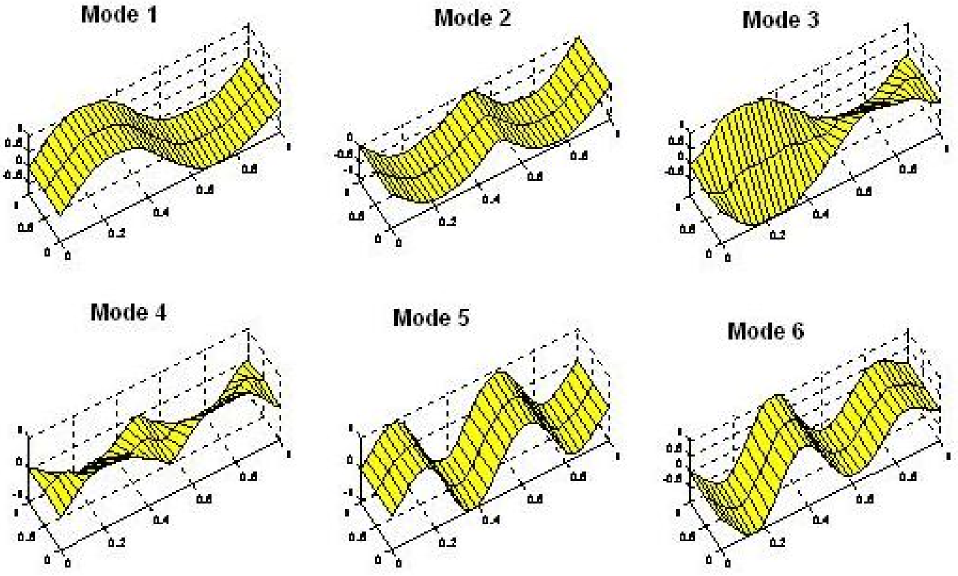

Figure 3.3 Peak Picking mode shapes

3.2 Natural Excitation Technique combined with Eigensystem Realization Algorithm (NExT-ERA)

NExT-ERA is the second method used for system identification of the Dowling Hall footbridge. In the following sections, a brief review of the theoretical bases is provided both for Natural Excitation Technique and Eigensystem Realization Algorithm together with the presentation of system identification result.

3.2.1 Natural Excitation Technique (NExT)

Conventional modal analysis utilizes frequency response functions (FRFs) which require measurements of both input force and the resulting response. However, ambient wind excitation does not lend itself to FRF calculations because the input force cannot be measured. NExT is a four-step process designed to estimate modal parameters of structures excited in their operating environment.

The first step is to acquire response data from the operating structure. Sensors that can measure strain, displacement, velocity, or acceleration response are required. Long time histories of continuous data are desired, provided the operating conditions are relatively stationary.

The second step is to calculate auto- and cross-correlation functions from these time histories using standard techniques. Correlation functions are commonly used to analyze randomly excited systems. As the following section will show, the correlation functions can be expressed as summations of decaying sinusoids. Each decaying sinusoid has a damped natural frequency and damping ratio that is identical to that of a corresponding structural mode.

The third step of NExT uses a time-domain modal identification scheme to estimate the modal parameters by treating the correlation functions as though they were free vibration responses that is, sums of decaying sinusoids. The Eigensystem Realization Algorithm (ERA) have been used as the time-domain modal identification schemes to extract modal frequencies and damping ratios.

The final step of NExT estimates mode shape using the identified modal frequencies and modal damping ratios. An activity closely related to mode shape extraction uses the identified modal parameters to synthesize the auto spectrum from each sensor. This provides a means of visually verifying the accuracy of the estimated modal frequencies and damping ratios.

A theoretical justification of NExT entails proving that a MIMO (multiple input, multiple output), multiple-mode system excited by random inputs produces autocorrelation and cross-correlation functions that are sums of decaying sinusoids.

Furthermore, these decaying sinusoids must have the same damped frequencies and damping ratios as the modes of the system. Consequently, the correlation functions will have the same form as impulse response functions and thus can be used in standard modal analysis algorithms.

The approach is to develop a general solution for a structure with a discrete spatial representation; define the cross-correlation function between two outputs; and solve for the case of random inputs. The theoretical justification of NExT can be developed for a general class of random inputs, fully complex modes, and the presence of known harmonic inputs. However, this development will be limited to the case of white-noise inputs, real modes, and no harmonics, thus allowing the reader to obtain an appreciation for the theoretical background of NExT without the added complexities of the most general case.

The derivation begins by assuming the standard matrix equations of motion:

$$\mathbf{[M]\ \{x(t)\} + [C]\ \{x(t)\} + [K]\ \{X(t)\} = \{f(t)\}} \tag{3.3}$$

Where:

[M] Is the mass matrix

[C] Is the damping matrix

[K] Is the stiffness matrix

{F} is a vector of random forcing functions

{X} is the vector of random displacements.

Equation (3.3) can be expressed in modal coordinates using a standard modal transformation:

$$\{x(t)\} = [\Phi]\{q(t)\} = \sum_{r=1}^{n} \{\phi^r\} q^r(t) \tag{3.4}$$

Where:

[**Φ**] Is the modal matrix

{q(t)} is a vector of modal coordinates

$\{\Phi^T\}$ is the *rth* mode shape.

A premultiplication of Equation (3.4) by $[\Phi]^T$ is also performed. Since real normal modes are assumed, [M], [C], and [K] are simultaneously diagonalized. A set of scalar equations in the modal coordinates result:

$$\ddot{q}^r(t) + 2\zeta^r\omega_n^r\dot{q}^r(t) + \omega_n^{r^2} q^r(t) = \frac{1}{m^r}\{\phi^r\}^T\{f(t)\} \tag{3.5}$$

where:

ω^r is the *rth* modal frequency

ζ^r is the *rth* modal damping ratio

m^r is the *rth* modal mass.

The solution of Equation (3.5), assuming a general {f} and zero initial conditions, is obtained from the convolution or Duharnel integral:

$$q^r(t) = \int_{-\infty}^{t} \{\phi^r\}^T\{f(\tau)\}\, g^r(t-\tau)\, d\tau \tag{3.6}$$

where: $g^r(t) = \frac{1}{m^r\omega_d^r} \exp(-\zeta^r\omega_n^r t)\ \sin(\omega_d^r t)$

Equations (3.4) and (3.6) can now be used to obtain the solution for *{x(t)}*:

$$\{x(t)\} = \sum_{r=1}^{n} \{\phi^{r}\} \cdot \int_{-\infty}^{t} \{\phi^{r}\}^{T} \{f(\tau)\}\, g^{r}(t-\tau)\, d\tau \tag{3.7}$$

where n is the number of modes.

Equation (3.7) will now be specialized for a single output, $x_{ik}(t)$, due to a single input force, $f_k(t)$, at point k.

$$x_{ik}(t) = \sum_{r=1}^{n} \phi_{i}^{r}\, \phi_{k}^{r} \cdot \int_{-\infty}^{t} f_{k}(\tau)\, g^{r}(t-\tau)\, d\tau \tag{3.8}$$

where $\boldsymbol{\Phi}^{T}$ is the *ith* component of mode shape r.

The impulse response function between input k and output i results when $f(\tau)$ in Equation (3.8) is a Dirac delta function at $\tau = O$. The integration is collapsed and the following results:

$$x_{ik}(t) = \sum_{r=1}^{n} \frac{\phi_{i}^{r}\phi_{k}^{r}}{m^{r}\omega_{d}^{r}} \exp(-\zeta^{r}\omega_{n}^{r}t)\, \sin(\omega_{d}^{r}t)\,. \tag{3.9}$$

The next step of the theoretical development is to form the cross-correlation function of two responses (x_{ik} and x_{jk}) due to a white-noise input at a particular input point k. defines the cross-correlation function $R_{ijk}(T)$ as the expected value of the product of two responses evaluated at a time separation of T:

$$R_{ijk}(T) = E[x_{ik}(t+T)\ x_{jk}(t)] \tag{3.10}$$

where E is the expectation operator.

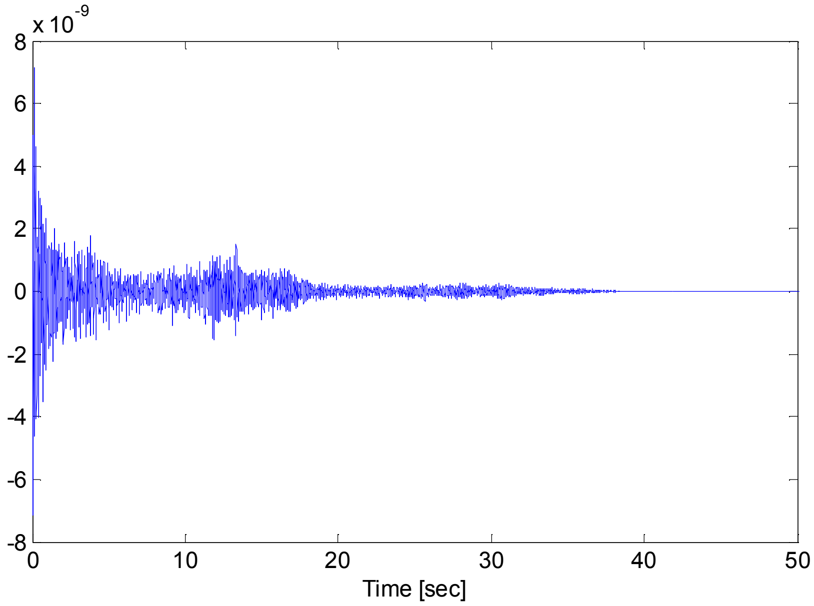

Figure 3.4 Cross-correlation function

Substituting Equation (3.8) into (3.10) results in the following, since $f_k(t)$ is the only random variable:

$$R_{ijk}(T) = \sum_{r=1}^{n} \sum_{s=1}^{n} \phi_i^r \phi_k^r \phi_j^s \phi_k^s \cdot \tag{3.11}$$

$$\int_{-\infty}^{t} \int_{-\infty}^{t+T} g^r(t+T-\sigma)\; g^s(t-\tau)\; E[f_k(\sigma)\, f_k(\tau)]\; d\sigma\; d\tau\ .$$

Using the definition of the autocorrelation function , and assuming f(t) of Equation (3.11) is white noise, then the autocorrelation function of f is:

$$R_{ff}^{k}(\tau-\sigma) = E[f_k(\tau)\;\; f_k(\sigma)] = \alpha_k \delta\,(\tau-\sigma) \tag{3.12}$$

where α_k is a constant and δ (t) is the Dirac delta function.

Substituting Equation (3.12) into Equation (3.11), and collapsing the first integration by using the definition of the delta function produces the following:

$$R_{ijk}(T) = \sum_{r=1}^{n} \sum_{s=1}^{n} \alpha_k \phi_i^r \phi_k^r \phi_j^s \phi_k^s \cdot \int_{-\infty}^{t} g^r(t+T-\tau)\ g^s(t-\tau)\, d\tau\,. \tag{3.13}$$

Equation (3.13) can be further simplified by making a change in the variable of integration. If we let λ = t — τ, then the limits of integration are zero and m. And Equation (3.13) becomes:

$$R_{ijk}(T) = \sum_{r=1}^{n} \sum_{s=1}^{n} \alpha_k \phi_i^r \phi_k^r \phi_j^s \phi_k^s \cdot \int_{0}^{\infty} g^r(\lambda+T)\ g^s(\lambda)\, d\lambda\,. \tag{3.14}$$

Using the definition of g from Equation (3.6) and the trig identity for the sine of a sum results in all the terms involving T separating from those involving λ:

$$\begin{aligned} g^r(\lambda+T) = {} & [\exp(-\zeta^r \omega_n^r T)\ \cos(\omega_d^r T)]\ \frac{\exp(-\zeta^r \omega_n^r \lambda)\ \sin(\omega_d^r \lambda)}{m^r \omega_d^r} \\ & +[\exp(-\zeta^r \omega_n^r T)\ \sin(\omega_d^r T)]\ \frac{\exp(-\zeta^r \omega_n^r \lambda)\ \cos(\omega_d^r \lambda)}{m^r \omega_d^r}\,. \end{aligned} \tag{3.15}$$

Note that substitution of Equation (3.15) into (3.14) along with the corresponding formula for $g^g(\lambda)$ allows terms that depend on T to be factored out of the integral and out of the second summation (the s-index), resulting in:

$$R_{ijk}(T) = \sum_{r=1}^{n} [G_{ijk}^r \exp(-\zeta^r \omega_n^r T)\ \cos(\omega_d^r T) + H_{ijk}^r \exp(-\zeta^r \omega_n^r T)\ \sin(\omega_d^r T)] \tag{3.16}$$

where G_{ijk} and H_{ijk}. k are independent of T, are functions of only the modal parameters, contain completely the summation on s, and are shown below.

$$\begin{Bmatrix} G^r_{ijk} \\ \\ H^r_{ijk} \end{Bmatrix} = \sum_{s=1}^{n} \frac{\alpha_k \phi^r_i \phi^r_k \phi^s_j \phi^s_k}{m^r \omega^r_d m^s \omega^s_d} \cdot \int_0^\infty \exp(-\zeta^r \omega^r_n - \zeta^s \omega^s_n)\,\lambda \cdot \sin(\omega^s_d \lambda) \begin{Bmatrix} \sin(\omega^r_d \lambda) \\ \\ \cos(\omega^r_d \lambda) \end{Bmatrix} d\lambda \tag{3.17}$$

Equation (3.16) is the key result of this derivation. Examining Equation (3.16), we can see that the cross-correlation function is indeed a sum of decaying sinusoids, with the same characteristics as the impulse response function of the original system (see Equation (3.9); thus, cross-correlation functions can be used as impulse response functions in time-domain modal parameter estimation schemes.

Lastly, G_{ijk} and H_{ijk} can be further simplified by evaluating the definite integral, and we have:

$$\begin{aligned} G^r_{ijk} &= \sum_{s=1}^{n} \frac{\alpha_k \phi^r_i \phi^r_k \phi^s_j \phi^s_k}{m^r m^s \omega^r_d} \left[\frac{I_{rs}}{J^2_{rs} + I^2_{rs}}\right] \\ H^r_{ijk} &= \sum_{s=1}^{n} \frac{\alpha_k \phi^r_i \phi^r_k \phi^s_j \phi^s_k}{m^r m^s \omega^r_d} \left[\frac{J_{rs}}{J^2_{rs} + I^2_{rs}}\right] \end{aligned} \tag{3.18}$$

To further illustrate the useful form of these results, define a quantity γ_{rs}, such that:

$$\tan(\gamma_{rs}) = I_{rs} \,/\, J_{rs}\,. \tag{3.19}$$

Using this relationship in Equations (3.18) and (3.19) provides:

$$G^r_{ijk} = \frac{\phi^r_i}{m^r \omega^r_d} \sum_{s=1}^{n} \beta^{rs}_{jk} \left(J^2_{rs} + I^2_{rs}\right)^{-1/2} \sin(\gamma_{rs}) \tag{3.20}$$

and

$$H^{r}_{ijk} = \frac{\phi^{r}_{i}}{m^{r}\omega^{r}_{d}} \sum_{s=1}^{n} \beta^{rs}_{jk} (J^{2}_{rs} + I^{2}_{rs})^{-1/2} \cos(\gamma_{rs}) \qquad (3.21)$$

where $\beta^{rs}_{jk} = \dfrac{\alpha_{k}\, \phi^{r}_{k}\, \phi^{s}_{j}\, \phi^{s}_{k}}{m^{s}}$

Substituting Equation (3.21) into Equation (3.16), and summing over all the input locations, m, to find the cross-correlation function due to all the input, we find:

$$R_{ij}(T) = \sum_{r=1}^{n} \frac{\phi^{r}_{i}}{m^{r}\omega^{r}_{d}} \sum_{s=1}^{n} \sum_{k=1}^{m} \beta^{rs}_{jk} (J^{2}_{rs} + I^{2}_{rs})^{-1/2} \exp(-\zeta^{r}\omega^{r}_{n}T) \sin(\omega^{r}_{d}T + \gamma_{rs}) \qquad (3.22)$$

The inner summations on s and k are merely a summation of constants times the sine function, with variable phase but fixed frequency. Equation (3.22) can therefore be rewritten as a single sine function with a new phase angle (Θ^{r}) and a new constant multiplier (Aj^{r}):

$$R_{ij}(T) = \sum_{r=1}^{n} \frac{\phi^{r}_{i} A^{r}_{j}}{m^{r}\omega^{r}_{d}} \exp(-\zeta^{r}\omega^{r}_{n}T) \sin(\omega^{r}_{d}T + \Theta^{r}) \qquad (3.23)$$

This completes the theoretical development for the single input, multi-output, multi-mode case. It shows that the cross-correlation function (3.23) is a sum of decaying sinusoids of the same form as the impulse response function of the original system in Equation (3.9). This similarity allows the use of time-domain modal parameter identification schemes such as ERA. The next sections illustrate some applications of NExT and further verify NExT using simulated data.

3.2.2 Eigensystem Realization Algorithm (ERA)

The ERA is a time-domain system identification based on the evolution of the method, which introduces the concept of minimum realization. It was developed by Juang and Pappa in 1985 as automate algorithm for modal parameters identification. The minimum realization method identifies a system model with the smallest state dimension that holds an equivalent relationship of input-output as in the real system. The algorithm description starts from the dynamic equation of motion of a damped linear system.

3.2.2.1 Discrete-Time State-Space System Representation

The classical differential equation encountered in problems of linear oscillations is:

$$\mathbf{M}\frac{d^2\mathbf{w}}{dt^2}+\boldsymbol{C}\frac{d\mathbf{w}}{dt}+\mathbf{K}\mathbf{w}=\mathbf{f}(t) \tag{3,24}$$

where **M**, ***C***, **K**, and **f** represent mass, damping, stiffness and force input, respectively. By making the substitutions:

$$\begin{aligned} &\mathbf{x}\equiv\begin{bmatrix}\mathbf{w}\\ \dfrac{d\mathbf{w}}{dt}\end{bmatrix} && \mathbf{f}(t)\equiv\mathbf{B}_0\mathbf{u}(t)\\ &\mathbf{A}_c\equiv\begin{bmatrix}\mathbf{0} & \mathbf{I}\\ -\mathbf{M}^{-1}\mathbf{K} & -\mathbf{M}^{-1}\boldsymbol{C}\end{bmatrix} && \mathbf{B}_c\equiv\begin{bmatrix}\mathbf{0}\\ \mathbf{M}^{-1}\mathbf{B}_0\end{bmatrix}\end{aligned} \tag{3.25}$$

the equation of motion can be written as a first-order system in state space:

$$\frac{d\mathbf{x}}{dt}=\mathbf{A}_c\mathbf{x}+\mathbf{B}_c\mathbf{u} \tag{3.26}$$

The general solution to (3.26) is:

$$\mathbf{x}(t) = e^{\mathbf{A}_c(t-t_0)}\mathbf{x}(t_0) + \int_{t_0}^{t} e^{\mathbf{A}_c(t-\tau)}\mathbf{B}_c\mathbf{u}(\tau)d\tau \tag{3.27}$$

We wish to use (3.27) to represent the system in discrete time by relating the present state to the state at a time Δt in the future. By making the substitutions:

$$t \equiv (k+1)\Delta t \qquad t_0 \equiv k\Delta t \tag{3.28}$$

(3.27) becomes:

$$\mathbf{x}((k+1)\Delta t) = e^{\mathbf{A}_c\Delta t}\mathbf{x}(k\Delta t) + \int_{k\Delta t}^{(k+1)\Delta t} e^{\mathbf{A}_c((k+1)\Delta t-\tau)}\mathbf{B}_c\mathbf{u}(\tau)d\tau \tag{3.29}$$

By making a change of variables $\tau' = (k+1)\Delta t - \tau$, and assuming $\mathbf{u}(t)$ is constant over the time interval, (3.29) simplifies to:

$$\mathbf{x}((k+1)\Delta t) = e^{\mathbf{A}_c\Delta t}\mathbf{x}(k\Delta t) + \int_{0}^{\Delta t} e^{\mathbf{A}_c\tau'}d\tau'\,\mathbf{B}_c\mathbf{u}(k\Delta t) \tag{3.30}$$

By defining:

$$\mathbf{A} \equiv e^{\mathbf{A}_c\Delta t} \qquad \mathbf{B} \equiv \int_{0}^{\Delta t} e^{\mathbf{A}_c\tau'}d\tau'\,\mathbf{B}_c \tag{3.31}$$

the discrete-time state space system equations become:

$$\begin{aligned} \mathbf{x}(k+1) &= \mathbf{A}\mathbf{x}(k) + \mathbf{B}\mathbf{u}(k) \\ \mathbf{y}(k) &= \mathbf{C}\mathbf{x}(k) + \mathbf{D}\mathbf{u}(k) \end{aligned} \tag{3.32}$$

In this notation $\mathbf{x}(k)$ refers to the internal state of the system while $\mathbf{y}(k)$ refers to measurements of the system. The system matrix **A** determines the evolution of the system with time. The input matrix **B** transfers the input **u** to the system. The output matrix **C** represents measurement of the system state and the feed-through matrix **D** represents direct measurement of the input **u**.

3.2.2.2 *Markov Parameters and Weighting Sequence*

Consider the output measurement of a system at rest subjected to a pulse input ($\mathbf{u}(0) = \mathbf{u}_0$ and $\mathbf{u}(k) = 0$ for $k>0$). By (3.32), the system state and measured output are:

$$\begin{aligned} &\mathbf{x}(0) = \mathbf{0} && \mathbf{y}(0) = \mathbf{D}\mathbf{u}_0 \\ &\mathbf{x}(1) = \mathbf{B}\mathbf{u}_0 && \mathbf{y}(1) = \mathbf{C}\mathbf{B}\mathbf{u}_0 \\ &\mathbf{x}(2) = \mathbf{A}\mathbf{B}\mathbf{u}_0 && \mathbf{y}(2) = \mathbf{C}\mathbf{A}\mathbf{B}\mathbf{u}_0 \\ &\quad\vdots && \quad\vdots \\ &\mathbf{x}(k) = \mathbf{A}^{k-1}\mathbf{B}\mathbf{u}_0 && \mathbf{y}(k) = \mathbf{C}\mathbf{A}^{k-1}\mathbf{B}\mathbf{u}_0 \end{aligned} \tag{3.33}$$

The output pulse response $\mathbf{y}(k)$ is completely determined by the sequence:

$$\mathbf{Y}_0 \equiv \mathbf{D} \quad \mathbf{Y}_1 \equiv \mathbf{C}\mathbf{B} \quad \mathbf{Y}_2 \equiv \mathbf{C}\mathbf{A}\mathbf{B} \quad \ldots \quad \mathbf{Y}_k \equiv \mathbf{C}\mathbf{A}^{k-1}\mathbf{B} \tag{3.34}$$

The sequence of $\mathbf{Y}_i$ is the unit pulse response sequence and is often referred to as the Markov parameter sequence.

The response to an arbitrary input signal can be cast in terms of the Markov parameters as follows:

$$\begin{aligned} &\mathbf{x}(0) = \mathbf{0} && \mathbf{y}(0) = \mathbf{D}\mathbf{u}(0) \\ &\mathbf{x}(1) = \mathbf{B}\mathbf{u}(0) && \mathbf{y}(1) = \mathbf{C}\mathbf{B}\mathbf{u}(0) + \mathbf{D}\mathbf{u}(1) \\ &\mathbf{x}(2) = \mathbf{A}\mathbf{B}\mathbf{u}(0) + \mathbf{B}\mathbf{u}(1) && \mathbf{y}(2) = \mathbf{C}\mathbf{A}\mathbf{B}\mathbf{u}(0) + \mathbf{C}\mathbf{B}\mathbf{u}(1) + \mathbf{D}\mathbf{u}(2) \\ &\quad\vdots && \quad\vdots \\ &\mathbf{x}(k) = \sum_{i=1}^{k} \mathbf{A}^{i-1}\mathbf{B}\mathbf{u}(k-i) && \mathbf{y}(k) = \sum_{i=1}^{k} \mathbf{C}\mathbf{A}^{i-1}\mathbf{B}\mathbf{u}(k-i) \\ & && \qquad = \sum_{i=1}^{k} \mathbf{Y}_i\mathbf{u}(k-i) \end{aligned} \tag{3.35}$$

This is sometimes known as the weighting sequence. Note the similarity between this formulation and the continuous-time case in which the response to an arbitrary forcing function is the convolution of the impulse response and the forcing function.

3.2.2.3 Controllability and Observability

The subject of controllability arises from considering what internal state $\mathbf{x}(p)$ is reached when a sequence of inputs $\mathbf{u}(k)$, $k=0..p-1$ is applied to the system. (3.35) gives the internal state as:

$$\mathbf{x}(p)=\sum_{i=1}^{p}\mathbf{A}^{i-1}\mathbf{B}\mathbf{u}(p-i) \tag{3.36}$$

This can be written as:

$$\mathbf{x}(p)=\mathbf{Q}_p\begin{bmatrix}\mathbf{u}(p-1)\\ \mathbf{u}(p-2)\\ \vdots\\ \mathbf{u}(0)\end{bmatrix} \tag{3.37}$$

where the controllability matrix $\mathbf{Q}_\mathrm{p}$ is defined as

$$\mathbf{Q}_p\equiv\begin{bmatrix}\mathbf{B} & \mathbf{AB} & \cdots & \mathbf{A}^{p-1}\mathbf{B}\end{bmatrix} \tag{3.38}$$

Note the sequence of inputs $\mathbf{u}$ is arranged in reverse-time order. If the rank of the controllability matrix is equal to the order of the system, any internal state can be reached with the proper input and the system is said to be ‘controllable.’

The subject of observability arises from considering whether an internal state $\mathbf{x}(0)$ can be determined by observing its free response $\mathbf{y}(k)$, $k=0..p-1$. The free response is given by:

$$\begin{aligned}\mathbf{y}(0)&=\mathbf{C}\mathbf{x}(0)\\ \mathbf{y}(1)&=\mathbf{CA}\mathbf{x}(0)\\ &\vdots\\ \mathbf{y}(p-1)&=\mathbf{C}\mathbf{A}^{p-1}\mathbf{x}(0)\end{aligned} \tag{3.39}$$

This can be written as:

$$\begin{bmatrix} \mathbf{y}(0) \\ \mathbf{y}(1) \\ \vdots \\ \mathbf{y}(p-1) \end{bmatrix} = \mathbf{P}_p \mathbf{x}(0) \tag{3.40}$$

where the observability matrix $\mathbf{P}_\mathrm{p}$ is defined as:

$$\mathbf{P}_p \equiv \begin{bmatrix} \mathbf{C} \\ \mathbf{CA} \\ \vdots \\ \mathbf{CA}^{p-1} \end{bmatrix} \tag{3.41}$$

If the rank of the observability matrix is equal to the order of the system, any initial internal state can be determined by observing its free response. Such a system is said to be ‘observable.”

3.2.2.4 Hankel Matrices

System identification algorithms commonly use a Hankel matrix composed of the Markov parameters (pulse response) of the system. The Hankel matrix is given as:

$$\mathbf{H}(k-1) \equiv \begin{bmatrix} \mathbf{Y}_k & \mathbf{Y}_{k+1} & \cdots & \mathbf{Y}_{k+\beta-1} \\ \mathbf{Y}_{k+1} & \mathbf{Y}_{k+2} & \cdots & \mathbf{Y}_{k+\beta} \\ \vdots & \vdots & \ddots & \vdots \\ \mathbf{Y}_{k+\alpha-1} & \mathbf{Y}_{k+\alpha} & \cdots & \mathbf{Y}_{k+\alpha+\beta-2} \end{bmatrix} = \begin{bmatrix} \mathbf{CA}^{k-1}\mathbf{B} & \mathbf{CA}^{k}\mathbf{B} & \cdots & \mathbf{CA}^{k+\beta-2}\mathbf{B} \\ \mathbf{CA}^{k}\mathbf{B} & \mathbf{CA}^{k+1}\mathbf{B} & \cdots & \mathbf{CA}^{k+\beta-1}\mathbf{B} \\ \vdots & \vdots & \ddots & \vdots \\ \mathbf{CA}^{k+\alpha-2}\mathbf{B} & \mathbf{CA}^{k+\alpha-1}\mathbf{B} & \cdots & \mathbf{CA}^{k+\alpha+\beta-3}\mathbf{B} \end{bmatrix} \tag{3.42}$$

where α and β are arbitrary indices which determine the size of the matrix.

The Hankel matrix can be factored in the following useful form:

$$\mathbf{H}(k) = \mathbf{P}_\alpha \mathbf{A}^k \mathbf{Q}_\beta \tag{3.43}$$

where $\mathbf{P}_\alpha$ and $\mathbf{Q}_\beta$ are the observability and controllability matrices defined in (3.38) and (3.41), respectively.

Hankel matrices are frequently formed but rarely interpreted. A simple interpretation is offered here. Consider the following experiment: A system is subjected to arbitrary input $\mathbf{f}(k)$, $k=0..\ \beta\text{-}1$. Once the input has been completed (after β time steps), the output $\mathbf{y}(k)$ is measured for α time steps (that is, for $k=\beta..\alpha+\beta\text{-}1$).

Following the form of the weighting sequence in (3.35), the input-output relation of the experiment described is:

$$\begin{aligned}
\mathbf{y}(\beta) &= \mathbf{Y}_1\mathbf{f}(\beta-1)+\mathbf{Y}_2\mathbf{f}(\beta-2)+\cdots+\mathbf{Y}_\beta\mathbf{f}(0)\\
\mathbf{y}(1+\beta) &= \mathbf{Y}_2\mathbf{f}(\beta-1)+\mathbf{Y}_3\mathbf{f}(\beta-2)+\cdots+\mathbf{Y}_{1+\beta}\mathbf{f}(0)\\
&\vdots\\
\mathbf{y}(\alpha+\beta-1) &= \mathbf{Y}_\alpha\mathbf{f}(\beta-1)+\mathbf{Y}_{\alpha+1}\mathbf{f}(\beta-2)+\cdots+\mathbf{Y}_{\alpha+\beta-1}\mathbf{f}(0)
\end{aligned} \tag{3.44}$$

Note that the input $\mathbf{f}(k)$ is zero for $k>\beta\text{-}1$ and that the output $\mathbf{y}(k)$ is only measured for $k>\ \beta\text{-}1$. (3.44) can therefore be rewritten in matrix form as:

$$\begin{bmatrix}\mathbf{y}(\beta)\\ \mathbf{y}(1+\beta)\\ \vdots\\ \mathbf{y}(\alpha+\beta-1)\end{bmatrix}=\begin{bmatrix}\mathbf{Y}_1 & \mathbf{Y}_2 & \cdots & \mathbf{Y}_\beta\\ \mathbf{Y}_2 & \mathbf{Y}_3 & \cdots & \mathbf{Y}_{1+\beta}\\ \vdots & \vdots & \ddots & \vdots\\ \mathbf{Y}_\alpha & \mathbf{Y}_{\alpha+1} & \cdots & \mathbf{Y}_{\alpha+\beta-1}\end{bmatrix}\begin{bmatrix}\mathbf{f}(\beta-1)\\ \mathbf{f}(\beta-2)\\ \vdots\\ \mathbf{f}(0)\end{bmatrix} \tag{3.45}$$

By identifying the rectangular matrix in (3.45) as $\mathbf{H}(0)$, it is seen that the Hankel matrix $\mathbf{H}(0)$ provides the input-output relationship for the experiment described. Note that in (3.45) (as in (3.37)), the input $\mathbf{f}$ is arranged in reverse-time order.

In the same fashion, the general Hankel matrix $\mathbf{H}(k)$ can be understood as the input-output relationship for a similar experiment in which the measurement begins an additional k time steps after the excitation has ended.

3.2.2.5 *The Eigensystem Realization Algorithm (ERA)*

The ERA begins by finding the singular values and vectors of the Hankel matrix **H**(0). In brief, the singular valued decomposition (SVD) finds matrices **U**, **Σ**, and **V** such that:

$$\mathbf{\Sigma} = \mathbf{U}^T \mathbf{H}(0)\mathbf{V} \qquad \mathbf{H}(0) = \mathbf{U}\mathbf{\Sigma}\mathbf{V}^T \tag{3.46}$$

where **U** and **V** are orthogonal matrices containing the left and right singular vectors, and **Σ** is a diagonal matrix.

For a (normalized) right singular vector **v**, the system output is **H**(0)**v** = σ**u**, where **u** is the corresponding (normalized) left singular vector and σ is the gain factor. The singular value decomposition of **H**(0) represents the solutions to the maximization of the output/input gain factor σ for the Hankel matrix **H**(0). These maxima are resonance conditions and correspond to the modes of the system.

Having found the SVD of **H**(0) (as in (3.46)), a decision must be made regarding the effective order of the system. For an observable noise-free system, the rank of the Hankel matrix will equal the order of the system. In the case of significant noise, the Hankel matrix will usually have a larger number of singular values, many of which are nearly zero. These small singular values correspond to noise in the signal. Modes with low input or observability may be masked by this noise.

An order *n* is chosen for the system such that the *n* largest singular values are judged to be true modes and the remaining smaller singular values are judged to be noise. At this point, the Hankel matrix may be re-formed using only the significant singular values:

$$\mathbf{H}_n(0) = \mathbf{U}_n \mathbf{\Sigma}_n \mathbf{V}_n^T \tag{3.47}$$

where $\mathbf{U}_n$, $\mathbf{\Sigma}_n$, and $\mathbf{V}_n$ have been truncated to only *n* singular values.
It was shown previously (3.43) that **H**(k) = $\mathbf{P}_\alpha \mathbf{A}^k \mathbf{Q}_\beta$, or **H**(0) = $\mathbf{P}_\alpha \mathbf{Q}_\beta$. The ERA proceeds by making the identifications:

$$\mathbf{P}_\alpha = \mathbf{U}_n \mathbf{\Sigma}_n^{1/2} \qquad \mathbf{Q}_\beta = \mathbf{\Sigma}_n^{1/2} \mathbf{V}_n^T \tag{3.48}$$

This is not the only possible factorization but it is the most obvious one.

By examining (3.38) and (3.41), the input and output matrices (**B** and **C**) can be identified as the first blocks of the controllability and observability matrices ($\mathbf{P}_\alpha$ and $\mathbf{Q}_\beta$).

The state matrix **A** is extracted using the shifted Hankel matrix **H**(1). It is known (3.43) that $\mathbf{H}(1) = \mathbf{P}_\alpha \mathbf{A} \mathbf{Q}_\beta$. By forming the pseudo-inverses of $\mathbf{P}_\alpha$ and $\mathbf{Q}_\beta$ as:

$$\mathbf{P}_\alpha^\dagger = \mathbf{\Sigma}_n^{-\frac{1}{2}} \mathbf{U}_n^T \qquad \mathbf{Q}_\beta^\dagger = \mathbf{V}_n \mathbf{\Sigma}_n^{-\frac{1}{2}} \tag{3.49}$$

the state matrix **A** is found to be:

$$\mathbf{A} = \mathbf{P}_\alpha^\dagger \mathbf{P}_\alpha \mathbf{A} \mathbf{Q}_\beta \mathbf{Q}_\beta^\dagger = \mathbf{P}_\alpha^\dagger \mathbf{H}(1) \mathbf{Q}_\beta^\dagger = \mathbf{\Sigma}_n^{-\frac{1}{2}} \mathbf{U}_n^T \mathbf{H}(1) \mathbf{V}_n \mathbf{\Sigma}_n^{-\frac{1}{2}} \tag{3.50}$$

3.2.2.6 Transformation of ERA Realization to Continuous Time

Once the system, input, and output matrices **A**, **B**, and **C** are found the realization is in principle complete. However, these matrices represent the system in discrete-time state space. The results must be transformed into continuous time and geometric space in order to determine the system parameters (natural frequencies, damping ratios, and mode shapes).

Equation (3.31), repeated here, states that:

$$\begin{aligned} &\mathbf{x} \equiv \begin{bmatrix} \mathbf{w} \\ \dfrac{d\mathbf{w}}{dt} \end{bmatrix} && \mathbf{f}(t) \equiv \mathbf{B}_0 \mathbf{u}(t) \\ &\mathbf{A}_c \equiv \begin{bmatrix} \mathbf{0} & \mathbf{I} \\ -\mathbf{M}^{-1}\mathbf{K} & -\mathbf{M}^{-1}C \end{bmatrix} && \mathbf{B}_c \equiv \begin{bmatrix} \mathbf{0} \\ \mathbf{M}^{-1}\mathbf{B}_0 \end{bmatrix} \end{aligned} \tag{3.51}$$

And

$$\mathbf{A} = e^{\mathbf{A}_c \Delta t} \tag{3.52}$$

Solving for $\mathbf{A}_c$, we find:

$$\mathbf{x} \equiv \begin{bmatrix} \mathbf{w} \\ \dfrac{d\mathbf{w}}{dt} \end{bmatrix} \qquad \mathbf{f}(t) \equiv \mathbf{B}_0 \mathbf{u}(t)$$
$$\mathbf{A}_c \equiv \begin{bmatrix} \mathbf{0} & \mathbf{I} \\ -\mathbf{M}^{-1}\mathbf{K} & -\mathbf{M}^{-1}C \end{bmatrix} \quad \mathbf{B}_c \equiv \begin{bmatrix} \mathbf{0} \\ \mathbf{M}^{-1}\mathbf{B}_0 \end{bmatrix} \tag{3.53}$$

And

$$\mathbf{A}_c = \frac{\ln(\mathbf{A})}{\Delta t} \tag{3.54}$$

It is most convenient to compute the eigenvalues and eigenvectors of **A** before attempting to compute ln(**A**):

$$\mathbf{x} \equiv \begin{bmatrix} \mathbf{w} \\ \dfrac{d\mathbf{w}}{dt} \end{bmatrix} \qquad \mathbf{f}(t) \equiv \mathbf{B}_0 \mathbf{u}(t)$$
$$\mathbf{A}_c \equiv \begin{bmatrix} \mathbf{0} & \mathbf{I} \\ -\mathbf{M}^{-1}\mathbf{K} & -\mathbf{M}^{-1}C \end{bmatrix} \quad \mathbf{B}_c \equiv \begin{bmatrix} \mathbf{0} \\ \mathbf{M}^{-1}\mathbf{B}_0 \end{bmatrix} \tag{3.55}$$

And

$$\mathbf{\Lambda} = \mathbf{\Psi}^T \mathbf{A} \mathbf{\Psi} \tag{3.56}$$

By the properties of the matrix exponential function, $\mathbf{A}_c$ has the same eigenvector matrix, $\boldsymbol{\psi}$, as **A** does. The eigenvalues of $\mathbf{A}_c$ are:

$$\mathbf{x} \equiv \begin{bmatrix} \mathbf{w} \\ \dfrac{d\mathbf{w}}{dt} \end{bmatrix} \qquad \mathbf{f}(t) \equiv \mathbf{B}_0 \mathbf{u}(t)$$
$$\mathbf{A}_c \equiv \begin{bmatrix} \mathbf{0} & \mathbf{I} \\ -\mathbf{M}^{-1}\mathbf{K} & -\mathbf{M}^{-1}C \end{bmatrix} \quad \mathbf{B}_c \equiv \begin{bmatrix} \mathbf{0} \\ \mathbf{M}^{-1}\mathbf{B}_0 \end{bmatrix} \tag{3.57}$$

And

$$\mathbf{\Lambda}_c = \frac{\ln(\mathbf{\Lambda})}{\Delta t} \tag{3.58}$$

Because the state-space representation is a first-order differential equation while the standard formulation (3.24) is a second-order differential equation, there are twice as many eigenvalues of **A** and $\mathbf{A}_c$ (that is, λ_i and $\lambda_{c,i}$) as there are system modes. These values occur as complex conjugate pairs for each mode. It is therefore sufficient to consider only alternating eigenvalues to determine the system parameters.

The natural frequencies and damping ratios are found using the eigenvalues $\lambda_{c,i}$, which are the poles of the system in Laplace's s-space. The natural frequency is the magnitude of the eigenvalue and the damping ratio is the cosine of the angle with the negative real axis.

$$\begin{aligned} &\mathbf{x} \equiv \begin{bmatrix} \mathbf{w} \\ \dfrac{d\mathbf{w}}{dt} \end{bmatrix} && \mathbf{f}(t) \equiv \mathbf{B}_0 \mathbf{u}(t) \\ &\mathbf{A}_c \equiv \begin{bmatrix} \mathbf{0} & \mathbf{I} \\ -\mathbf{M}^{-1}\mathbf{K} & -\mathbf{M}^{-1}\mathcal{C} \end{bmatrix} && \mathbf{B}_c \equiv \begin{bmatrix} \mathbf{0} \\ \mathbf{M}^{-1}\mathbf{B}_0 \end{bmatrix} \end{aligned} \tag{3.59}$$

And

$$\begin{aligned} &\omega_{n,i} = \left|\lambda_{c,2i-1}\right| \\ &\xi_i = -\cos\left(\tan^{-1}\left(\frac{\mathrm{Re}(\lambda_{c,2i-1})}{\mathrm{Im}(\lambda_{c,2i-1})}\right)\right) = -\frac{\mathrm{Re}(\lambda_{c,2i-1})}{\omega_{n,i}} \end{aligned} \tag{3.60}$$

The mode shapes (as detected by the sensors) are simply the measurements associated with the eigenvectors $\boldsymbol{\psi}$. The ^ symbol indicates that the matrix **C** has been estimated in the realization:

$$\begin{aligned} &\mathbf{x} \equiv \begin{bmatrix} \mathbf{w} \\ \dfrac{d\mathbf{w}}{dt} \end{bmatrix} && \mathbf{f}(t) \equiv \mathbf{B}_0 \mathbf{u}(t) \\ &\mathbf{A}_c \equiv \begin{bmatrix} \mathbf{0} & \mathbf{I} \\ -\mathbf{M}^{-1}\mathbf{K} & -\mathbf{M}^{-1}\mathcal{C} \end{bmatrix} && \mathbf{B}_c \equiv \begin{bmatrix} \mathbf{0} \\ \mathbf{M}^{-1}\mathbf{B}_0 \end{bmatrix} \end{aligned} \tag{3.61}$$

And

$$\boldsymbol{\varphi} = \hat{\mathbf{C}}_{\text{modal}} = \hat{\mathbf{C}}\boldsymbol{\psi} \tag{3.62}$$

The eigenvectors occur as complex conjugate pairs for the same reasons that the eigenvalues do. The mode shapes therefore usually consist of complex numbers. For a noise-free system with classical damping, all components of a mode are collinear in the complex plane. Due to noise, experimental components will not be exactly collinear even in the case of classical damping. However, for modes which display nearly collinear shape, real-valued mode shapes can be found by projecting the complex-valued components onto the mode shape's principal axis. The individual mode shapes can then be normalized by one of the standard methods, giving a normalized modal matrix $\boldsymbol{\Phi}$.

3.2.2.7 Advantages of the ERA realization

It has been previously stated that there are many realizations which give the same system parameters, that is, there is not a unique valid realization. The first step in system realization as performed by the ERA is identifying $\mathbf{P} = \mathbf{U}\boldsymbol{\Sigma}^{1/2}$ and $\mathbf{Q} = \boldsymbol{\Sigma}^{1/2}\mathbf{V}^{\mathrm{T}}$. This step seems arbitrary at first glance. It is worthwhile to consider this realization in more detail. Recall the roles of the observability and controllability matrices ((3.40) and (3.37), repeated below):

$$\begin{aligned} \mathbf{x} &\equiv \begin{bmatrix} \mathbf{w} \\ \dfrac{d\mathbf{w}}{dt} \end{bmatrix} & \mathbf{f}(t) &\equiv \mathbf{B}_0\mathbf{u}(t) \\ \mathbf{A}_c &\equiv \begin{bmatrix} \mathbf{0} & \mathbf{I} \\ -\mathbf{M}^{-1}\mathbf{K} & -\mathbf{M}^{-1}\boldsymbol{C} \end{bmatrix} & \mathbf{B}_c &\equiv \begin{bmatrix} \mathbf{0} \\ \mathbf{M}^{-1}\mathbf{B}_0 \end{bmatrix} \end{aligned} \tag{3.63}$$

And

$$\begin{bmatrix} \mathbf{y}(0) \\ \mathbf{y}(1) \\ \vdots \\ \mathbf{y}(p-1) \end{bmatrix} = \mathbf{P}_p \mathbf{x}(0) \qquad \mathbf{x}(p) = \mathbf{Q}_p \begin{bmatrix} \mathbf{f}(p-1) \\ \mathbf{f}(p-2) \\ \vdots \\ \mathbf{f}(0) \end{bmatrix} \tag{3.64}$$

There is some freedom in the realization of **P** and **Q**; any realization which preserves the relation **H**(*0*) = **PQ** will preserve the eigenvalues of the system matrix **A** and give the same system parameters. Considering that the right singular vectors **v** of the Hankel matrix **H**(*0*) represent resonant input, we would expect the input **v** to also maximize the final internal state **x**(*p*). **Q** is therefore chosen such that its right singular vectors are the same as those of **H**(*0*):

$$\begin{gathered} \mathbf{x} \equiv \begin{bmatrix} \mathbf{w} \\ \dfrac{d\mathbf{w}}{dt} \end{bmatrix} \qquad \mathbf{f}(t) \equiv \mathbf{B}_0 \mathbf{u}(t) \\ \mathbf{A}_c \equiv \begin{bmatrix} \mathbf{0} & \mathbf{I} \\ -\mathbf{M}^{-1}\mathbf{K} & -\mathbf{M}^{-1}C \end{bmatrix} \quad \mathbf{B}_c \equiv \begin{bmatrix} \mathbf{0} \\ \mathbf{M}^{-1}\mathbf{B}_0 \end{bmatrix} \end{gathered} \tag{3.65}$$

And

$$\mathbf{K} = \mathbf{M}^T \mathbf{Q} \mathbf{V} \qquad \mathbf{Q} = \mathbf{M} \mathbf{K} \mathbf{V}^T \tag{3.66}$$

where **K** is a diagonal matrix containing singular values of **Q** and **M** is an undetermined orthogonal matrix. **V** is understood to be the same right singular matrix as for **H**(*0*).

In the same manner, the left singular vectors **u** of the Hankel matrix **H**(*0*) represent modal free decay. We would expect the output **u** to correspond to a minimized (i.e. one-mode) initial internal state **x**(*0*). **P** is therefore chosen such that its left singular vectors are the same as those of **H**(*0*):

$$\mathbf{x} \equiv \begin{bmatrix} \mathbf{w} \\ \dfrac{d\mathbf{w}}{dt} \end{bmatrix} \qquad \mathbf{f}(t) \equiv \mathbf{B}_0\mathbf{u}(t)$$

$$\mathbf{A}_c \equiv \begin{bmatrix} \mathbf{0} & \mathbf{I} \\ -\mathbf{M}^{-1}\mathbf{K} & -\mathbf{M}^{-1}C \end{bmatrix} \quad \mathbf{B}_c \equiv \begin{bmatrix} \mathbf{0} \\ \mathbf{M}^{-1}\mathbf{B}_0 \end{bmatrix} \tag{3.67}$$

And

$$\mathbf{\Lambda} = \mathbf{U}^T\mathbf{P}\mathbf{N} \qquad \mathbf{P} = \mathbf{U}\mathbf{\Lambda}\mathbf{N}^T \tag{3.68}$$

where $\mathbf{\Lambda}$ is a diagonal matrix containing singular values of $\mathbf{P}$ and $\mathbf{N}$ is an undetermined orthogonal matrix. $\mathbf{U}$ is understood to be the same left singular matrix as for $\mathbf{H}(0)$.

Forming the Hankel matrix $\mathbf{H}(0)$ from the decompositions of $\mathbf{P}$ and $\mathbf{Q}$, we have $\mathbf{H}(0) = \mathbf{PQ} = \mathbf{U\Lambda N}^\mathrm{T}\mathbf{MKV}^\mathrm{T}$. From the singular value decomposition of $\mathbf{H}(0)$ we also know that $\mathbf{H}(0) = \mathbf{U\Sigma V}^\mathrm{T}$. $\mathbf{\Lambda N}^\mathrm{T}\mathbf{MK}$ is therefore identified as the (diagonal) singular value matrix $\mathbf{\Sigma}$.

Because $\mathbf{\Lambda N}^\mathrm{T}\mathbf{MK}$ is diagonal and $\mathbf{\Lambda}$ and $\mathbf{K}$ are each separately diagonal, $\mathbf{N}^\mathrm{T}\mathbf{M}$ must also be diagonal. Because $\mathbf{N}$ and $\mathbf{M}$ are each separately orthogonal, $\mathbf{N}^\mathrm{T}\mathbf{M}$ must also be orthogonal. $\mathbf{N}^\mathrm{T}\mathbf{M}$ is therefore a diagonal orthogonal matrix – the identity matrix – $\mathbf{N}^\mathrm{T}\mathbf{M} = \mathbf{I}$ and $\mathbf{N} = \mathbf{M}$. We therefore have $\mathbf{\Lambda N}^\mathrm{T}\mathbf{MK} = \mathbf{\Lambda K} = \mathbf{\Sigma}$. $\mathbf{\Lambda}$ and $\mathbf{K}$ are chosen to be equal in order to balance the input and output gains: $\mathbf{\Lambda} = \mathbf{K} = \mathbf{\Sigma}^{½}$.

With the above identifications made, we can write $\mathbf{P} = \mathbf{U\Sigma}^{½}\mathbf{M}^\mathrm{T}$ and $\mathbf{Q} = \mathbf{M\Sigma}^{½}\mathbf{V}^\mathrm{T}$, where $\mathbf{M}$ is yet to be identified. To make the best choice for $\mathbf{M}$, consider the observability and controllability Gramians: $\mathbf{P}^\mathrm{T}\mathbf{P} = \mathbf{M\Sigma M}^\mathrm{T}$ and $\mathbf{QQ}^\mathrm{T} = \mathbf{M\Sigma M}^\mathrm{T}$. If $\mathbf{M}$ is chosen as the identity matrix, the observability and controllability Gramians will be simultaneously equal and diagonal, with both being equal to the singular values $\mathbf{\Sigma}$ of the Hankel matrix.

By substituting $\mathbf{M} = \mathbf{I}$ we have the realization $\mathbf{P} = \mathbf{U\Sigma}^{½}$ and $\mathbf{Q} = \mathbf{\Sigma}^{½}\mathbf{V}^\mathrm{T}$.

3.2.3 Identification results

Table 3.3 and Table 3.4 present the natural frequencies and the damping ratios of the six identified modes for each of the 4 April and 4 June five tests, respectively. The modes frequencies have been compared using the coefficient of variation (C_v), defined as: $C_v=\sigma/\mu$. It is a normalized measure of dispersion of a probability distribution. The small coefficient of variation (C_v) for the identified natural frequencies indicates the accuracy of these estimates. However, the same accuracy is not found for the damping ratios. The C_v of the natural frequency estimates are in the range of 0,13-1,6%, while the corresponding coefficient for damping ratios are in the range 0,42-1,09%. However, these identified damping values provide an estimation of the structure’s damping. Table 3.3 put in evidence the accuracy of the system identification method, showing precise results especially for Mode 1 and Mode 3, the first vertical deflection and torsional modes respectively.

Table 3.3 April tests NExT-ERA identification results

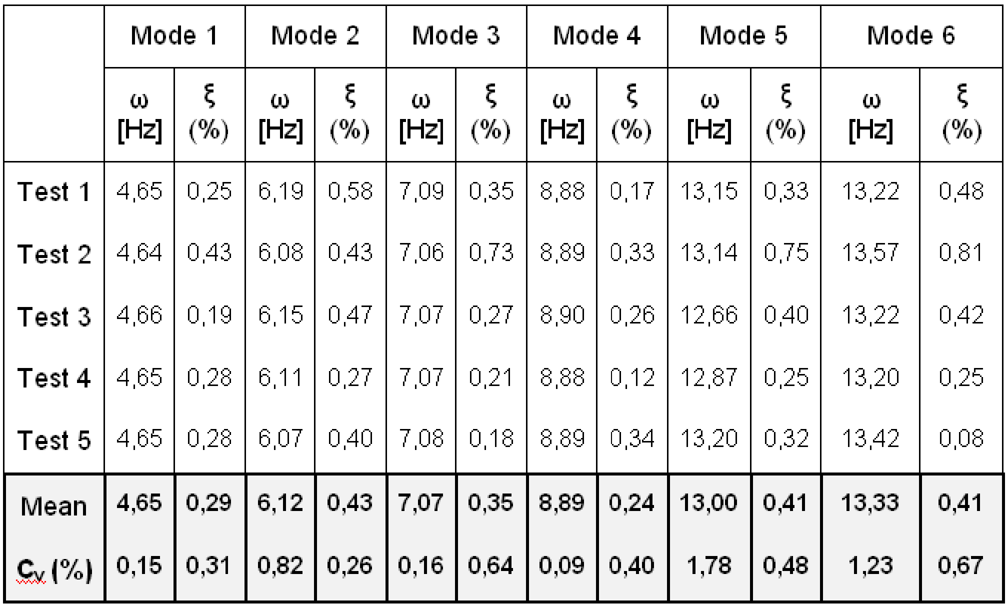

	Mode 1		Mode 2		Mode 3		Mode 4		Mode 5		Mode 6	
	ω [Hz]	ξ (%)	ω [Hz]	ξ (%)	ω [Hz]	ξ (%)	ω [Hz]	ξ (%)	ω [Hz]	ξ (%)	ω [Hz]	ξ (%)
Test 1	4,65	0,25	6,19	0,58	7,09	0,35	8,88	0,17	13,15	0,33	13,22	0,48
Test 2	4,64	0,43	6,08	0,43	7,06	0,73	8,89	0,33	13,14	0,75	13,57	0,81
Test 3	4,66	0,19	6,15	0,47	7,07	0,27	8,90	0,26	12,66	0,40	13,22	0,42
Test 4	4,65	0,28	6,11	0,27	7,07	0,21	8,88	0,12	12,87	0,25	13,20	0,25
Test 5	4,65	0,28	6,07	0,40	7,08	0,18	8,89	0,34	13,20	0,32	13,42	0,08
Mean	**4,65**	**0,29**	**6,12**	**0,43**	**7,07**	**0,35**	**8,89**	**0,24**	**13,00**	**0,41**	**13,33**	**0,41**
C_V (%)	**0,15**	**0,31**	**0,82**	**0,26**	**0,16**	**0,64**	**0,09**	**0,40**	**1,78**	**0,48**	**1,23**	**0,67**

Results from 4 June test are collected in Table 3.4. Data show a good correlation between the six modes identified, with best results for

Mode 1 and Mode 3 as the 4 April test results. The influence of the ambient factor can be recognize, in particular the temperature effect on the structure's stiffness variation. The natural frequencies identified on the 4 June test are smaller than the natural frequencies identified on the 4 April test. This fact is due to a warmer temperature on the June test day that provides a less structure's stiffness and so smaller natural frequencies. However, both results from the two tests are really close one to the other, showing the good efficiency of the instrumentation and of the system identification process employed.

Table 3.4 June tests NExT-ERA identification results

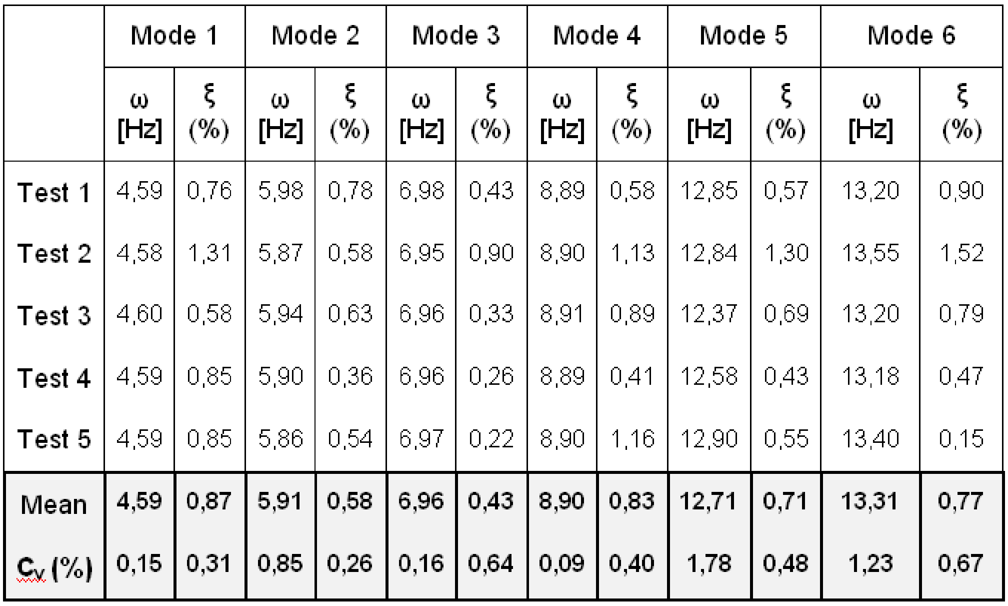

	Mode 1		Mode 2		Mode 3		Mode 4		Mode 5		Mode 6	
	ω [Hz]	ξ (%)	ω [Hz]	ξ (%)	ω [Hz]	ξ (%)	ω [Hz]	ξ (%)	ω [Hz]	ξ (%)	ω [Hz]	ξ (%)
Test 1	4,59	0,76	5,98	0,78	6,98	0,43	8,89	0,58	12,85	0,57	13,20	0,90
Test 2	4,58	1,31	5,87	0,58	6,95	0,90	8,90	1,13	12,84	1,30	13,55	1,52
Test 3	4,60	0,58	5,94	0,63	6,96	0,33	8,91	0,89	12,37	0,69	13,20	0,79
Test 4	4,59	0,85	5,90	0,36	6,96	0,26	8,89	0,41	12,58	0,43	13,18	0,47
Test 5	4,59	0,85	5,86	0,54	6,97	0,22	8,90	1,16	12,90	0,55	13,40	0,15
Mean	**4,59**	**0,87**	**5,91**	**0,58**	**6,96**	**0,43**	**8,90**	**0,83**	**12,71**	**0,71**	**13,31**	**0,77**
C_V (%)	**0,15**	**0,31**	**0,85**	**0,26**	**0,16**	**0,64**	**0,09**	**0,40**	**1,78**	**0,48**	**1,23**	**0,67**

Figure 3.5 presents the identified mode shapes corresponding to the six identified modes reported in Table 3.4

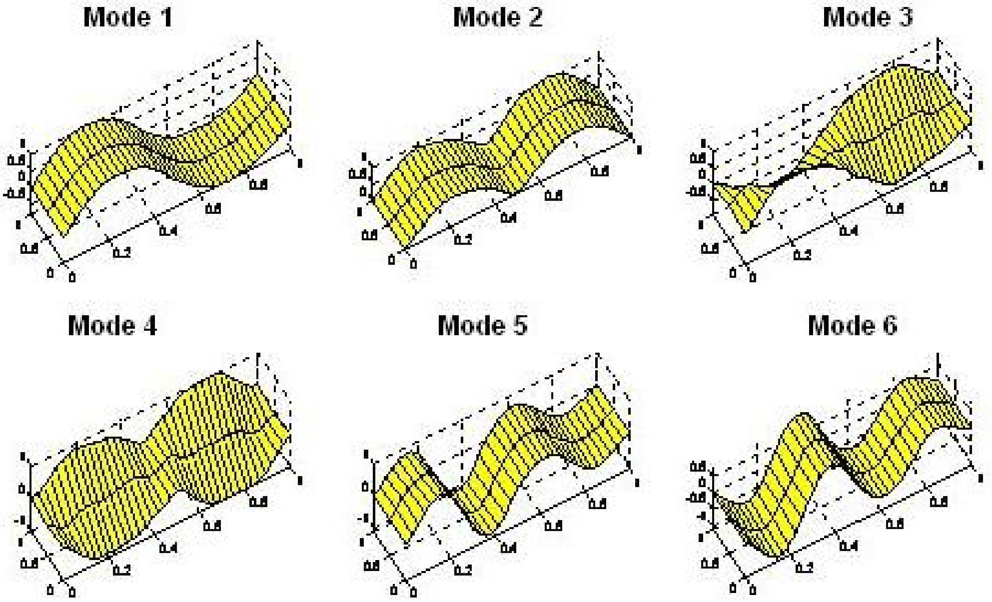

Figure 3.5 NExT-ERA mode shapes

3.3 Comparison of the April and June tests experimentally identified modal parameters

Once the modal identification phase was completed, the two sets of mode shapes resulting from the application of PP and NExT-ERA were compared using the Modal Assurance Criterion (MAC, Allemang and Brown 1982). The MAC is probably the most commonly used procedure to correlate two sets of mode shape vectors and is defined as:

$$MAC\ (\phi_{A,k}, \phi_{B,j}) = \frac{(\phi_{A,k}^{T}\phi_{B,j})^{2}}{(\phi_{A,k}^{T}\phi_{A,k})(\phi_{B,j}^{T}\phi_{B,j})}$$

where $\phi_{A,k}$ is the k-th mode of data set A and $\phi_{B,j}$ the j-th mode of the data set B. The MAC is a coefficient analogous to the correlation coefficient in statistics and ranges from 0 to 1; a value of 1 implies perfect correlation of the two mode shape vectors while a value close to 0 indicates uncorrelated (orthogonal) vectors. In general, a MAC value greater than 0.80 is considered a good match while a MAC value less than 0.40 is considered a poor match.

Table 3.5 summarizes, the modal parameters identified from the PP and the NExT-ERA techniques and the mode classification. Specifically, Table 3.5 compares the corresponding mode shapes and scaled modal vectors obtained from the two different output-only identification techniques through the frequency discrepancy $D_F = |(f_{\text{NExT-ERA}} - f_{\text{PP}}) / f_{\text{NExT-ERA}}|$ and the MAC.

Table 3.5 Peak Picking, NExT-ERA identification results

April Test		D_F (%)	June Test		D_F (%)	MAC	Vibration modes
f_{PP} (Hz)	$f_{NExT\text{-}ERA}$ (Hz)		f_{PP} (Hz)	$f_{NExT\text{-}ERA}$ (Hz)			
4,65	4,65	0,00	4,59	4,59	0,00	1,00	1st vertical anti-symmetric
6,14	6,12	0,33	5,93	5,91	0,34	0,99	2st vertical symmetric
7,08	7,07	0,14	6,97	6,96	0,14	0,98	1st torsional anti-symmetric
8,89	8,89	0,00	8,90	8,90	0,00	0,99	2st torsional symmetric
12,85	13,00	1,15	12,56	12,71	1,18	0,98	3st vertical anti-symmetric
13,19	13,33	1,05	13,17	13,31	1,05	0,98	4st vertical symmetric

Table (3.5) shows the results of the two system identification in terms of natural frequencies. The output-only analysis results are referred to the 4 April and 4 June tests.

The D_f coefficients shows the good correlation between the PP and the NExT-ERA results, both for the 4 April and for the 4 June tests. The identified natural frequencies are close one to each other for the two dynamic tests. The MAC coefficients relate the mode shapes: it puts in evidence the matching between the mode shapes identification performed with the PP and the NExT-ERA methods. The two system idendification methods are capable of providing a complete modal analysis, returning similar results. As shown in Table 3.5, the 4 April test and the 4 June test natural frequencies are close but not the same. This fact shows the influence of ambient parameters (temperature and humidity) on the structure’s dynamic behavior. In fact, temperature and humidity modify the stiffness of the structural elements, producing changes in the dynamic response. 4 June test natural frequencies are smaller than the 4 April test natural frequencies because the higher temperature situation performing the 4 June test, decrease the stiffness of the bridge, resulting in a more deformable structure’s behavior.

The PP and the NExT-ERA have shown to be powerful tools for modal analysis and dynamic parameters identification, providing similar results for the two dynamic tests performed.

4. TEST-ANALYSIS CORRELATION

4.1 Finite element model

Since the early 70s, many finite element models have been proposed for the analysis of structural elements. They were mainly devoted to the design of any types of complex structures in civil engineering fields. During the last two decades, several review papers and bibliographies have appeared in the open literature on the finite element technology and modeling of structural elements (beams, plates, shells, continua).

In modern times the finite element method has become established as the universally accepted analysis method in structural design. The method leads to the construction of a discrete system of matrix equations to represent the mass and stiffness effects of a continuous structure. The matrices are usually banded and symmetric. No restriction is placed upon the geometrical complexity of the structure because the mass and stiffness matrices area assembled from the contributions of the individual finite elements with simple shapes. Thus, each finite element possesses a mathematical formula which is associated with a simple geometrical description, irrespective of the overall geometry of the structure. Accordingly, the structure is divided into discrete areas or volumes known as elements. Element boundaries are defined when nodal pointes are connected by a unique polynomial curve or surface. In the most popular (isoperimetric, displacement type) elements, the same polynomial description is used to relate the internal, element displacements to the displacement of the nodes. This process is generally known as shape function interpolation. Since the boundary nodes are shared between neighboring elements, the displacement field is usually continuous across the element boundaries

The mathematical formulation of the finite element method can be posed as a variational problem with an element-wise Rayleigh-Ritz treatment and shape function discretisation. Alternatively the finite element equations may be obtained directly from the differential equations using a Galerkin approach weighted by the element shape functions. It is undoubtedly the combination of mathematical versatility with a simple geometric interpolation which has led to the immense popularity of the method across wide areas of engineering and sconce. The well known texts by Zienkiewicz and Taylor (1988) and Irons and Ahmad (1980) provide details of the formulation of element matrices for various structural element types (beams, plates, shells, continua). NAFEMS (1986) produced A Finite Element Primer which is an. excellent introduction to finite element methodology.

For model updating, the influence of the shape function upon the distribution of mass and stiffness must be understood if the result is to be an improvement in the physical parameterization, as well as a closer agreement between test results and numerical predictions. The discretisation using shape functions affects both the eigendata and the sensitivities of the numerical model.

The experimental investigation was preceded by the development of a 3D finite element model (Figure 4.1), based on as-built drawings of the bridge and on-site geometric survey. The model was formulated using the following assumptions:

a) two-nodes beam elements were used to represent the steel trusses structure;

b) the Dowling Hall, the main campus and the center pier supports were considered as fixed;

c) the concrete slabs were modeled with plate elements ;

d) an equivalent weight per unit volume of 26 kN/m3 was assumed for the deck concrete slab in order to account for the effects of the heated system.

The model results in a total of 76 nodes, 197 beam elements and 18 plate elements.

A preliminary dynamic analysis was performed to check the similarity between experimental and theoretical modal parameters.

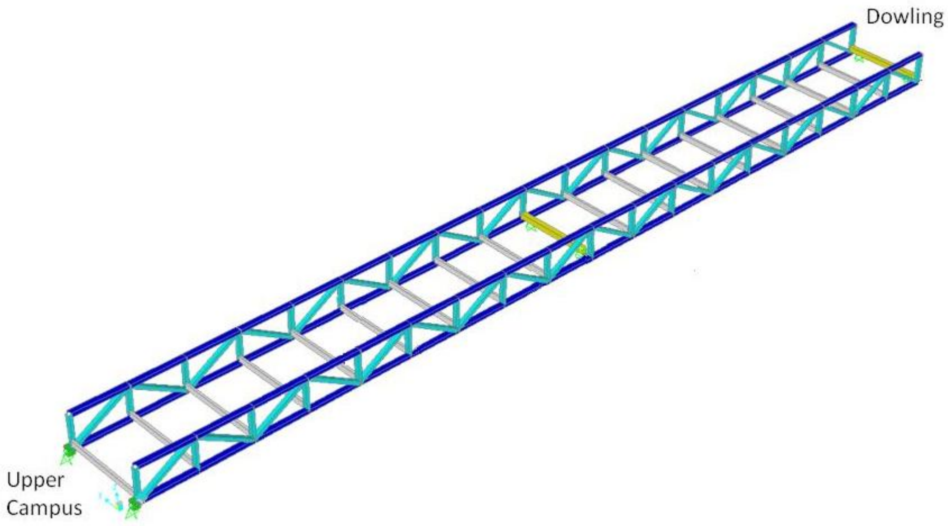

Figure 4.1 Dowling Hall footbridge finite element model

4.2 Calibration of the finite element model based upon the analytical experimental correlation study

Finite element model updating has emerged in the 1990s as a subject of immense importance to the design, construction and maintenance of mechanical systems and civil engineering structures. Computer based analysis techniques (especially the finite element method) have had a huge impact on engineering design and product development since the 1960s. In the case of many engineering products, we now stand at the point where more detailed finite element models are not capable of delivering the improvements in product performance that are demanded. Clearly, the approach of numerical predictions to the behavior of a physical system is limited by the assumptions used in the development of the mathematical model. Model updating, at its most ambitious, is about correcting invalid assumptions by processing vibration test results. Updating is a process fraught with numerical difficulties. These arise from inaccuracy in the model and imprecision and lack of information in the measurements. An understanding of the purpose of the updated model is necessary before an answer to the above question can be given. In some cases, the only requirement of the updated model is that it should replicate the physical test data. The extent to which a numerical model can be improved by updating depends upon the richness of information on the test structure contained in measurements. In general, the measurements will be both imprecise and incomplete. The imprecision takes the form of random and systematic noise.

Signal processing errors, such as aliasing and leakage, may be reduced by the correct choice of filters and excitation signals. Systematic errors can occur when, for example, the suspension system fails to replicate free-free conditions, or when the mass of a roving accelerometer causes changes in measured natural frequencies. Rigidly clamped boundary conditions are usually very difficult to obtain in a physical test. Extreme care is necessary to either eliminate systematic errors, or to obtain an assessment of them which can be used in subsequent processing. The measurements will be incomplete in the sense that the measurement frequency range (determined by the sampling rate) will be much shorter than that of the numerical model which might typically contain tens or hundreds of thousands of degrees of freedom. An extreme case of incompleteness occurs when the inputs, or response sensors, are located at, or close to, vibration nodes so that the effect of one or more modes is obscured by measurement noise. In addition to modal incompleteness, the measurements will also be spatially incomplete. This arises because the number of measurement stations is generally very much smaller than the number of degrees of freedom in the finite element model. Rotational degrees of freedom are usually not measured and some degrees of freedom will be inaccessible. Spatial incompleteness often requires either the reduction of the model or the expansion of measured eigenvectors.

Analysis results obtained by experimental dynamic tests were compared with those given modal analysis performed by the numerical FE model. Experimental results represent the baseline figures to update the FE model. In fact, being affected by the mathematical model assumptions and errors of fact concerning the mechanical characteristics and constraints of structural elements, they should be targeted according to the findings resulting from the experimental tests.

The calibration process allowed the model to be updated in the mass estimated of the concrete deck's elements and to optimize the stiffness of the supports, particularly the central pier. However, the mathematical modeling confirmed the results of the experimental analysis, both for the natural frequencies and the mode shapes, avoiding blunders in experimental analysis.

The mode shapes obtained from FE model are shown in Figure (4.2):

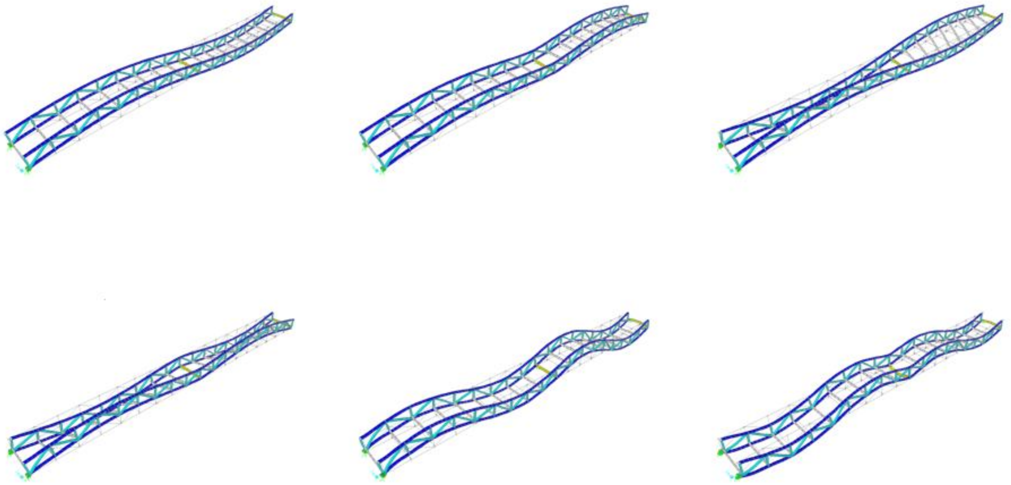

Figure 4.2 Finite element model mode shapes

4.3 Comparison of FE predicted and experimentally identified modal parameters

Once the modal identification phase was completed, the two sets of mode shapes resulting from the application of PP and NExT-ERA were compared using the Modal Assurance Criterion (MAC, Allemang and Brown 1982). The MAC is probably the most commonly used procedure to correlate two sets of mode shape vectors and is defined as:

$$MAC\ (\phi_{A,k}, \phi_{B,j}) = \frac{(\phi_{A,k}^{T}\phi_{B,j})^2}{(\phi_{A,k}^{T}\phi_{A,k})(\phi_{B,j}^{T}\phi_{B,j})}$$

where $\phi_{A,k}$ is the k-th mode of data set A and $\phi_{B,j}$ the j-th mode of the data set B. The MAC is a coefficient analogous to the correlation coefficient in statistics and ranges from 0 to 1; a value of 1 implies perfect correlation of the two mode shape vectors while a value close to 0 indicates uncorrelated (orthogonal) vectors. In general, a MAC value greater than 0.80 is considered a good match while a MAC value less than 0.40 is considered a poor match.

Table 4.1 summarizes, the modal parameters identified from the PP and the NExT-ERA techniques and the mode classification. Specifically, Table 4.1 compares the corresponding mode shapes and scaled modal vectors obtained from the two different output-only identification techniques through the frequency discrepancy $D_F = |(f_{NExT-ERA} - f_{FEM})/f_{NExT-ERA}|$ and the MAC.

Table 4.1 Peak Picking, NExT-ERA and FEM identification results

f_{PP} (Hz)	$f_{NExT-ERA}$ (Hz)	f_{FEM} (Hz)	D_F (%)	MAC	Vibration modes
4,59	4,59	4,58	0,22	1,00	1st vertical anti-symmetric
5,93	5,91	6,13	3,72	0,99	2st vertical symmetric
6,97	6,96	7,80	6,75	0,98	1st torsional anti-symmetric
8,90	8,90	9,21	3,48	0,99	2st torsional symmetric
12,56	12,71	14,21	11,80	0,98	3st vertical anti-symmetric
13,17	13,31	15,33	15,18	0,98	4st vertical symmetric

Table (4.1) shows the results of experimental and FE model analysis in terms of natural frequencies. The output-only analysis results are referred to the 4 June test. However, the natural frequencies are variable throughout the year depending on environmental conditions (particularly temperature, humidity) that influence the stiffness characteristics of the structure.

The comparison shows that the FE model results are correct and faithfully approximate the dynamic characteristics of the real structure. In particular, the discrepancy of the natural frequencies is on the order of 6% for the first two vertical and torsional deflections and not exceeds 15% for the next modes. The MAC coefficient confirms the accuracy of the modal shapes obtained by experimental analysis and numerical simulation.

In agreement with the results, the FE model provides a representation of the structure's actual situation and can be used for future analysis of static and dynamic.

Future work: the continuous monitoring system project

Structural Health Monitoring (SHM) provides a vital link between monitored structures and a central monitoring site. This allows many structures to be monitored at a central site, with information transmitted via the Internet, thereby eliminating costly permanent site installation and reducing the number of site visits. SHM also provide a structured approach to assessing the performance of various ISIS technologies and reporting on successes based on monitoring a number of field projects over extended periods of time. In addition to field projects, numerical modeling and identification of damage using the finite element method and, alternatively, damage detection algorithms, are also being developed. Acceptance of intelligent sensing and structural health monitoring as an essential part of infrastructure design.

Long-term continuous monitoring of structures may be helpful in many aspects of structural engineering when parameters of interest can be affected significantly over time. Such monitoring systems require high-speed data acquisition systems, highly sensitive sensors, and efficient operating software, and remote control and transfer mechanisms for data collection. Such remote monitoring systems are now possible. To test the idea of continuous monitoring for bridge structures and to examine the sensitivity of vibration properties to structural damage or deterioration, specifications for remote bridge-monitoring systems were developed.

They were implemented on bridges for experimental monitoring of conditions. Although intended for use in monitoring bridge structures, they may also be used where remote monitoring is appropriate for such civil engineering structures as dams, retaining walls, buildings, pavements, drainage structures, and traffic signal and sign structures.

Starting from the results of the dynamic tests, the experimental and numerical modeling analysis, and a continuous monitoring system is being design and installing on the Dowling Hall Footbridge. The dynamic tests design allowed selecting the proper instrumentation properties and the most suitable sensors locations.

The NExT-ERA algorithm provided good results in identifying the dynamic characteristics, starting from the output-only measurements. The NExT-ERA identification process has been automated for the continuous acquisition system compatibility, in order to process the continuous sensors' measurements. The continuous system data acquisition instrumentation will employ a Wi-Fi internet connection device, allowing data to be transfer directly to the central analysis location. The data acquisition system will be similar to the one employed for 4 April and 4 June dynamic testing and will be placed close to the Dowling Hall side, providing the sensors connection along the structure. PCB accelerometers proved their effectiveness performing the two dynamic tests. Therefore, the same kind of sensors will be employed for the continuous monitoring system design.

The continuous monitoring system will provide all the information for controlling the dynamic characteristics evolution across the years, correlating the dynamic behavior with the ambient parameters (temperature, humidity). Through the system, future structural damages and failures will be identified by the observation of the dynamic characteristics change, especially evidences in the natural frequencies alteration will suggest global troubles and the mode shapes allow the identification of local damages.

CONCLUSIONS

This work was focused on the design and realization of two dynamic tests and on the structural identification of the Dowling Hall footbridge, starting from the results of these tests.

The development of the project started with the process of evaluating and identifying the most appropriate instrumentation for tests achievement, planning and carrying out the test and the acquisition and processing of recorded data. First, a data processing step was performed, allowing deleting errors in the acquisition phase and provide a good quality data set for future analysis.

Two different algorithms were designed to identify the dynamic characteristics: the Peak Picking (PP) method and the Natural Excitation Technique combined with Eigensystem Realization Algorithm (NExT-ERA). The two methods made it possible to automate the process of natural frequencies, the damping ratios and mode shapes extraction. Both methods have proved to be effective and properly corrected for modal identification, as shown in Table 3.5, which compares the results obtained with both methods in terms of natural frequencies and modal shapes correlation (through the MAC coefficients). The two algorithms have a different implementation complexity and computational honor. The PP method was found to be lighter and more manageable. Nevertheless, the results it produces are quite comparable with those obtained employing the NExT-ERA. The latter is certainly a more complex, both during deployment and in runtime. However the advantage of allowing fully automatic analysis of data obtained from recordings made directly on the structure of the instrumentation (time history), producing as a result of the dynamic characteristics.

The results of the experimental analysis were compared and validated with those produced by a numerical analysis carried out through the creation of a finite element model. Once certified that the data from the experimental analysis were not infected by fundamental error, they were used as the basis for calibrating and updating the numerical model, so that it could better reflect the behavior of the real structure. This adjustment has resulted in a model that can be used for future analysis without the need to implement any experimental tests.

The results produced by both the experimental analysis that those using the numerical model were taken as a basis for designing of a continuous monitoring system that will be developed and installed in the near future. The complete automation of the identification system that uses the NExT-ERA for the dynamic analysis has allowed the selection of that method as a tool for processing data that will be used in the continuous monitoring system, allowing data acquisition and processing in time real and the identification of anomalies that may indicate the presence of problems or structural damage.

REFERENCES

Abdel-Ghaffar, A. M., and Housner, G. W. (1978) "*Ambient vibration tests of suspension bridge.*" Journal of the Engineering Mechanics Division, ASCE, 104(5), 983-999.

Alan V. Oppenheim, Alan S. Willsky, S. Hamid Nawab. (1997) *Signals and systems."* Prentice Hall, Upper Saddle River, New Jersey, U.S.A.

Bendat J. S., Piersol A. G. (1993), *"Engineering Applications of Correlation and Spectral Analysis",* Wiley.

Cunha, A., Caetano, E., and Delgado, R. (2001) "*Dynamic tests on large cable-stayed bridge."* Journal of Bridge Engineering, ASCE, 6(1), 54-62.

Farrar C. R., James. G. H. (1997) "System identification from ambient vibration measurements on a bridge." Journal of Sound and Vibration, 205(1), 1-18, MS P946 Sandia National Laboratories, Albuquerque, New Mexico, U.S.A.

James, G. H., Carne, T.G., Lauffer, J.P. Nard, A. R. (1992) "*Modal Testing Using Natural Excitation,"* Proc. of the 10-th IMAC, San Diego, CA, U.S.A.

James, G. H., Carne, T. G., and Lauffer, J. P. (1993) *"The natural excitation technique for modal parameters extraction from operating wind turbines."* Report No. SAND92-1666, UC-261, Sandia National Laboratories, Sandia, New Mexico.

Jer-Nan Juang. (1994) *"Applied system identification."* NASA Langley Research Centre, Prentice Hall, Upper Saddle River, New Jersey, U.S.A.

Joel P. Conte, Xianfei He, Babak Moaveni, Sami F. Masri, John P. Caffrey, Mazen Wahbeh, Farzad Tasbihgoo, Daniel H. Whang, and Ahmed Elgamal (2008) *"Dynamic Testing of Alfred Zampa Memorial Bridge."* Journal of Structural Engineering, ASCE. 134 (6), pp. 1006-1015. 10.1061. eScholarship Repository, University of California.

Juan M. Caicedo, Johannio Marulanda, Peter Thomson and Shirley J. Dyke (2001) *"Monitoring of Bridges to Detect Changes in Structural Health."* Proceedings of the 2001 American Control Conference, Arlington, Virginia.

Juang, J. N., and Pappa, R. S. (1985) *"An eigensystem realization algorithm for modal parameter identification and model reduction."* Journal of Guidance, Control and Dynamics, 8(5), 620-627.

Kalman, R. E. (1963) *"Mathematical description of linear dynamical systems."* SIAM J. Control, 1(2), 152-192.

Moaveni, B., Barbosa, A.R., Conte, J.P., and Hemez, F.M. (2007). "Uncertainty Analysis of Modal Parameters Obtained from Three System Identification Methods." Proc. of International Conference on Modal Analysis *(IMAC-XXV)*, Orlando, USA.

Oppenheim, A. V., and Schafer R. W. (1989) *"Discrete-time signal processing,"* Prentice Hall, Englewood Cliffs, New Jersey.

Phan, M., Juang, J. N., and Longman, R. W. (1991) *"On Markov parameters in system identification."* NASA Technical Memorandum 104156, Langley Research Center, Hampton, Virginia.

Raymond A. De Callafon, Babak Moaveni, Joel P. Conte, Xianfei He, and Eric Udd, (2008) *"General Realization Algorithm for Modal*

Identification of Linear Dynamic Systems." Journal of Engineering Mechanics, ASCE. 134 (9), pp. 712-722. 10.1061/(ASCE), eScholarship Repository, University of California.

Sohn, H., Farrar, C. R., Hemez, F. M., Shunk, D. D., Stinemates, D. W., and Nadler, B. R. (2003) *"A review of structural health monitoring literature: 1996-2001."* Report No. LA-13976-MS, Los Alamos National Laboratory, Los Alamos, New Mexico.

Vandewalle, J., and de Moor, B. (1988) *"On the use of the singular value decomposition in identification and signal processing."* Proc. of the workshop of the NATO Advanced Study Institute on Numerical Linear Algebra, Digital Signal Processing and Parallel Algorithms, Leuven, Belgium, 321-360.

Ward Heylen, Stefan Lammens, Paul Sas. (1997) *"Modal analysis theory and testing."* KUL Press, Leuven, Belgium.

APPENDIX A :

4 April Test

Time history, Fourier amplitude spectra and Power Spectral Density for all the channel and all the performed tests.

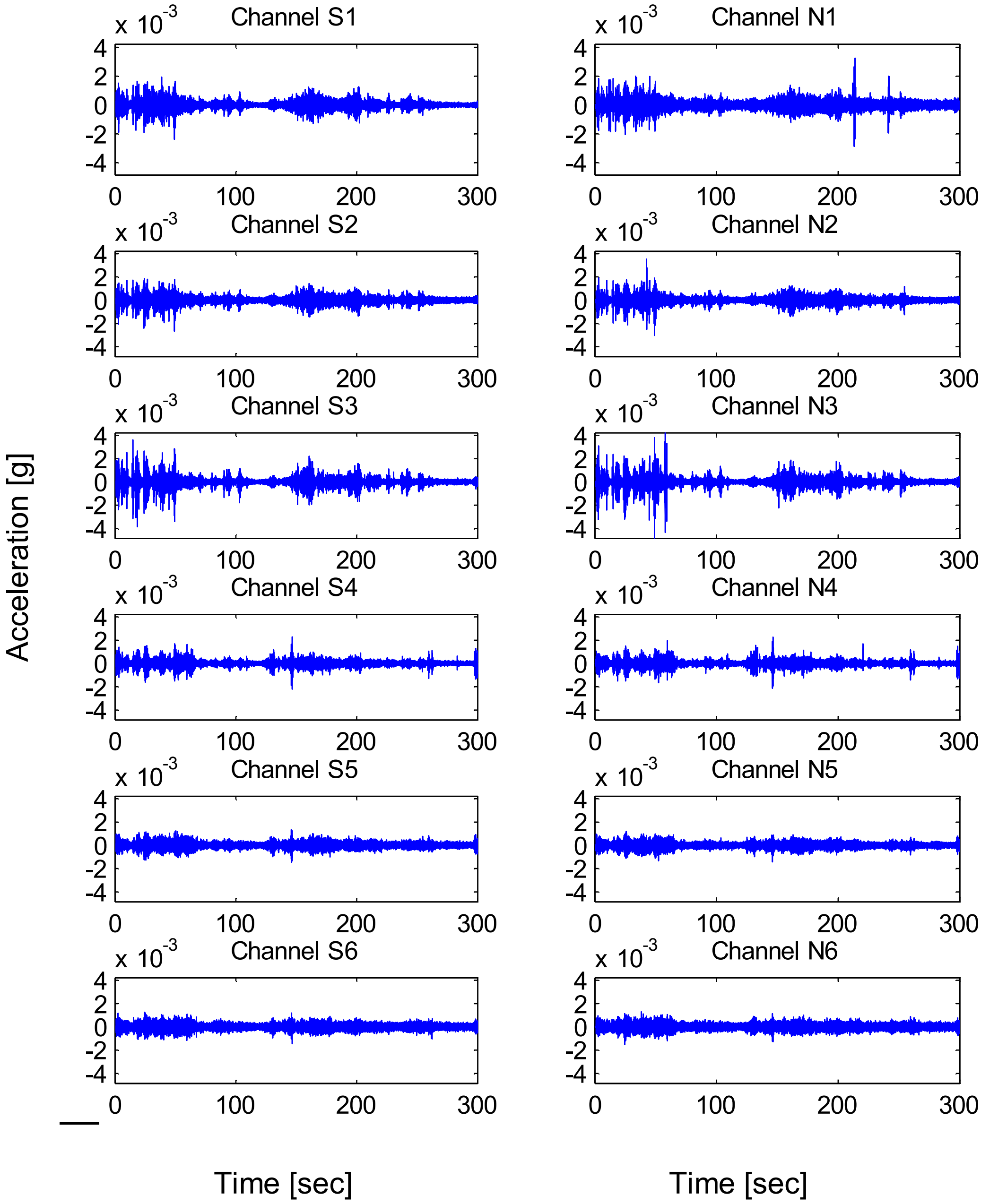

Figure A-1. Time history of the 12 channels recorded during Test 1

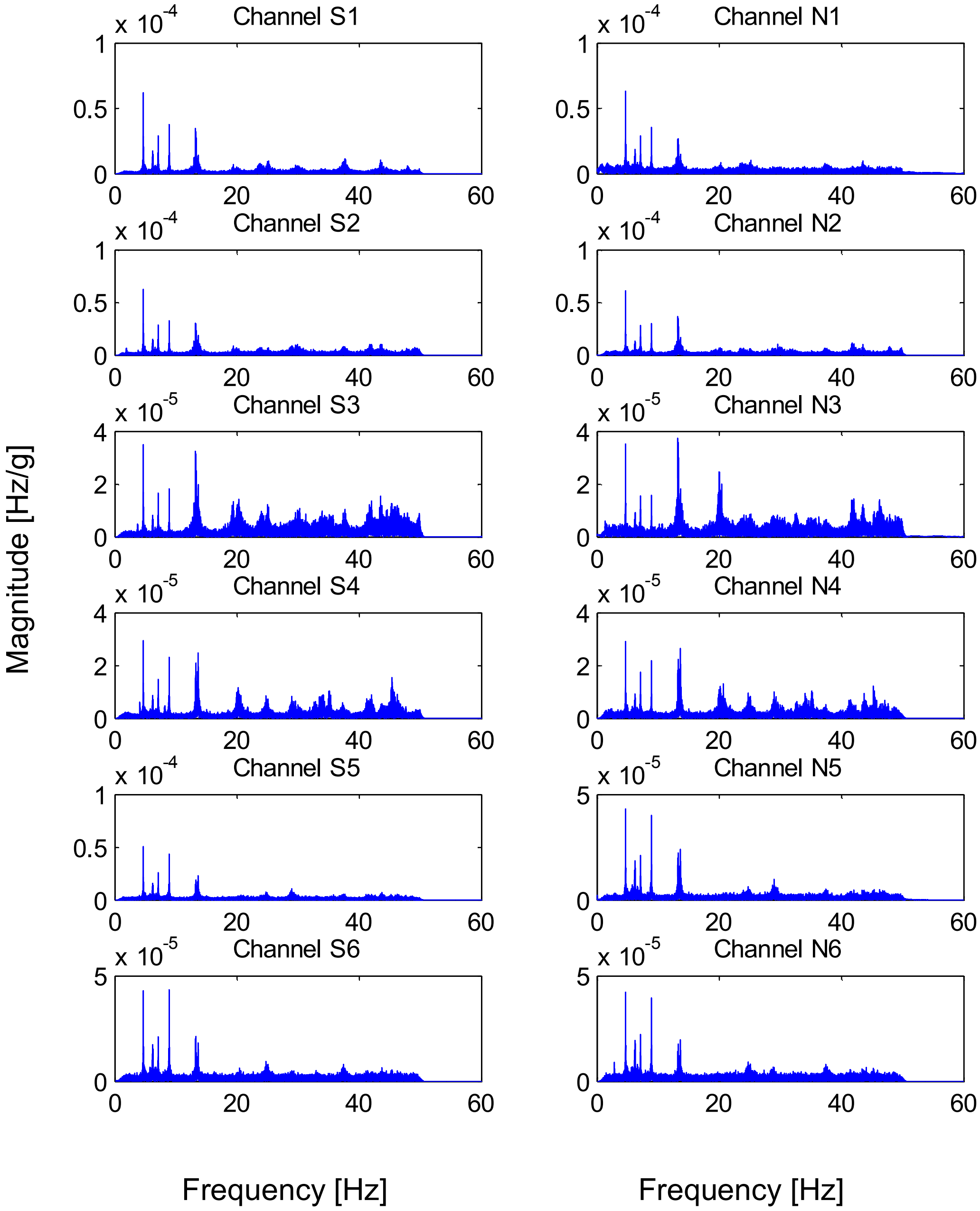

Figure A-2. Fourier amplitude spectra of the 12 channels recorded during Test 1

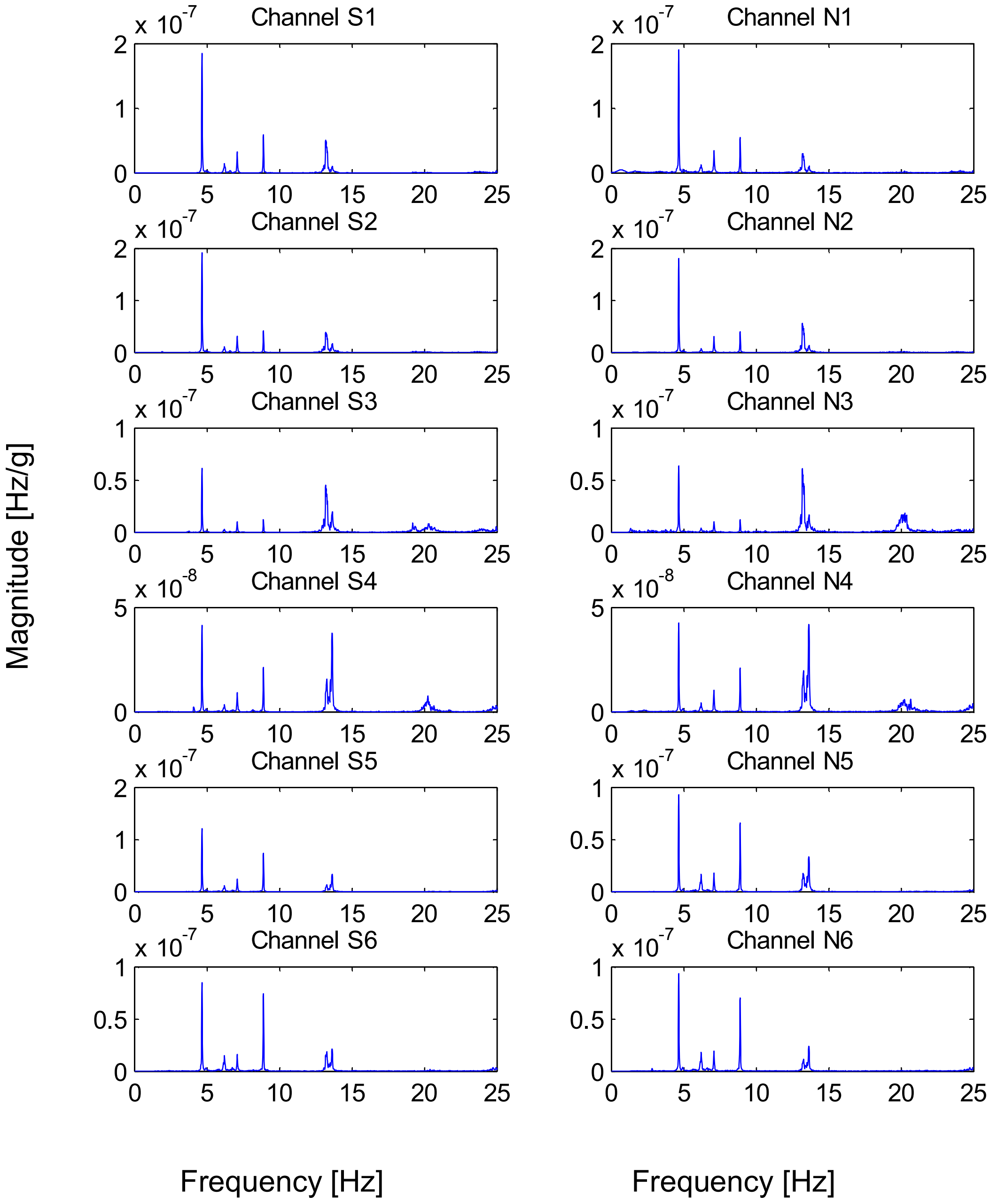

Figure A-3. Power Spectra Density of the 12 channels recorded during Test 1

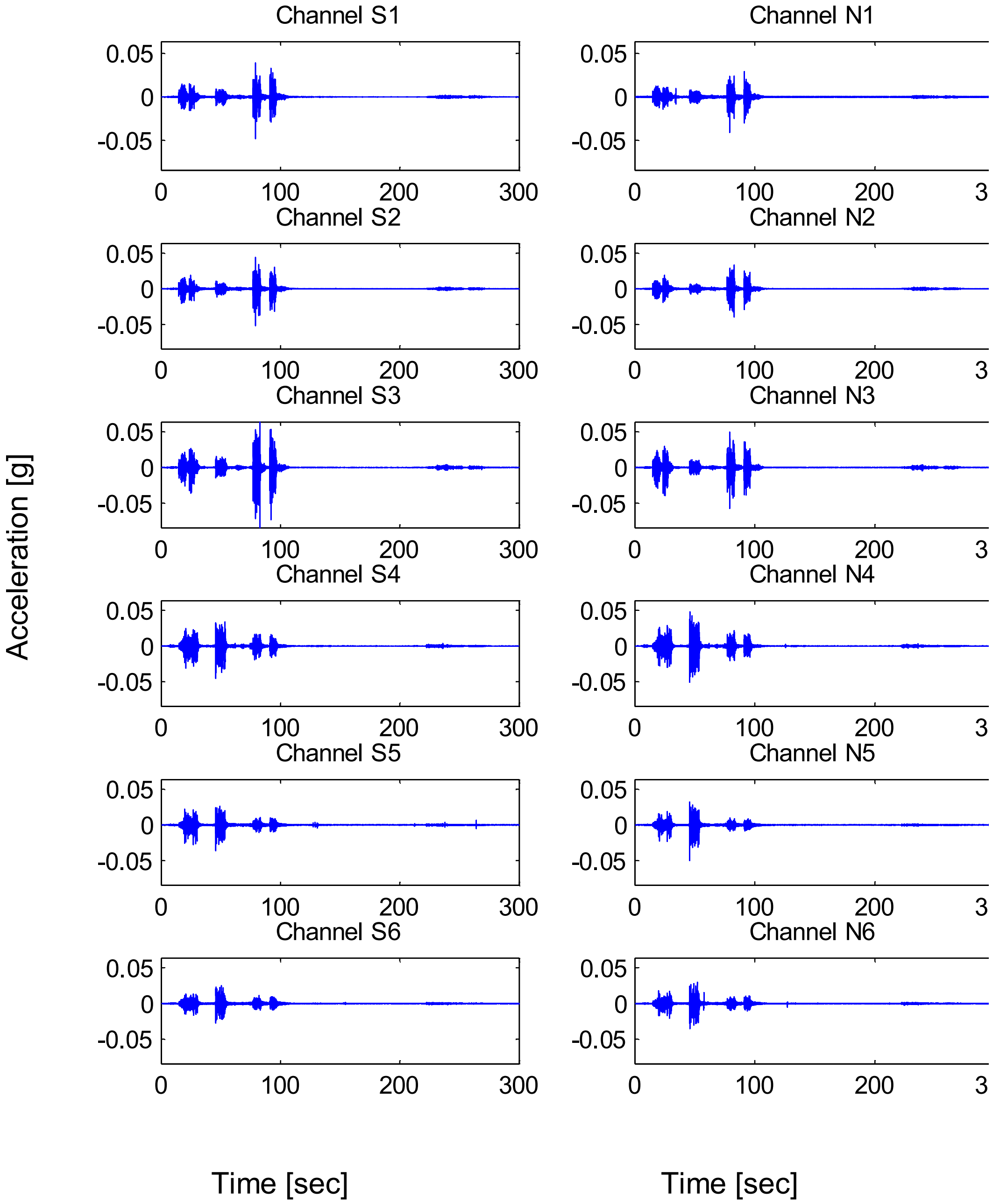

Figure A-4. Time history of the 12 channels recorded during Test 2

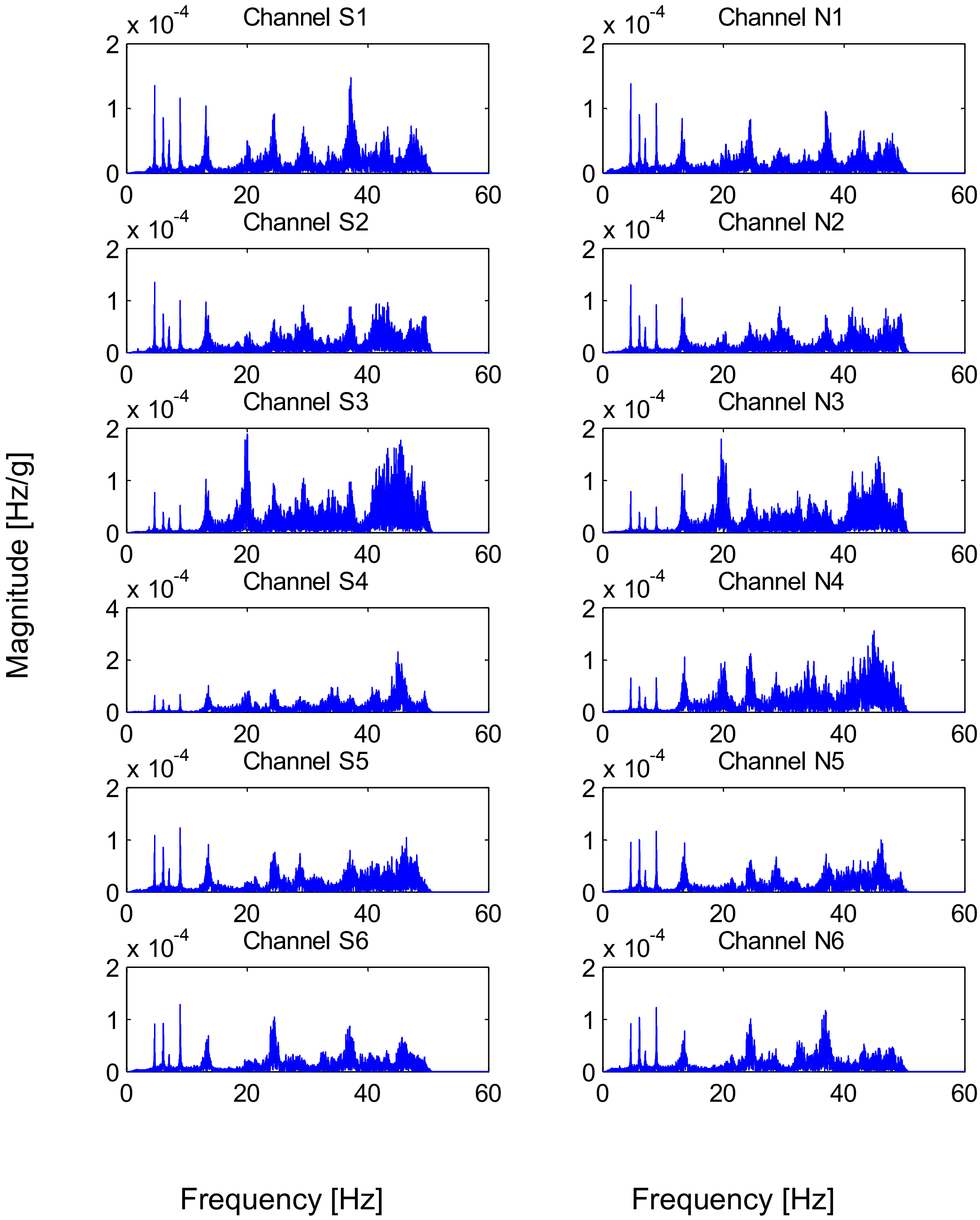

Figure A-5. Fourier amplitude spectra of the 12 channels recorded during Test 2

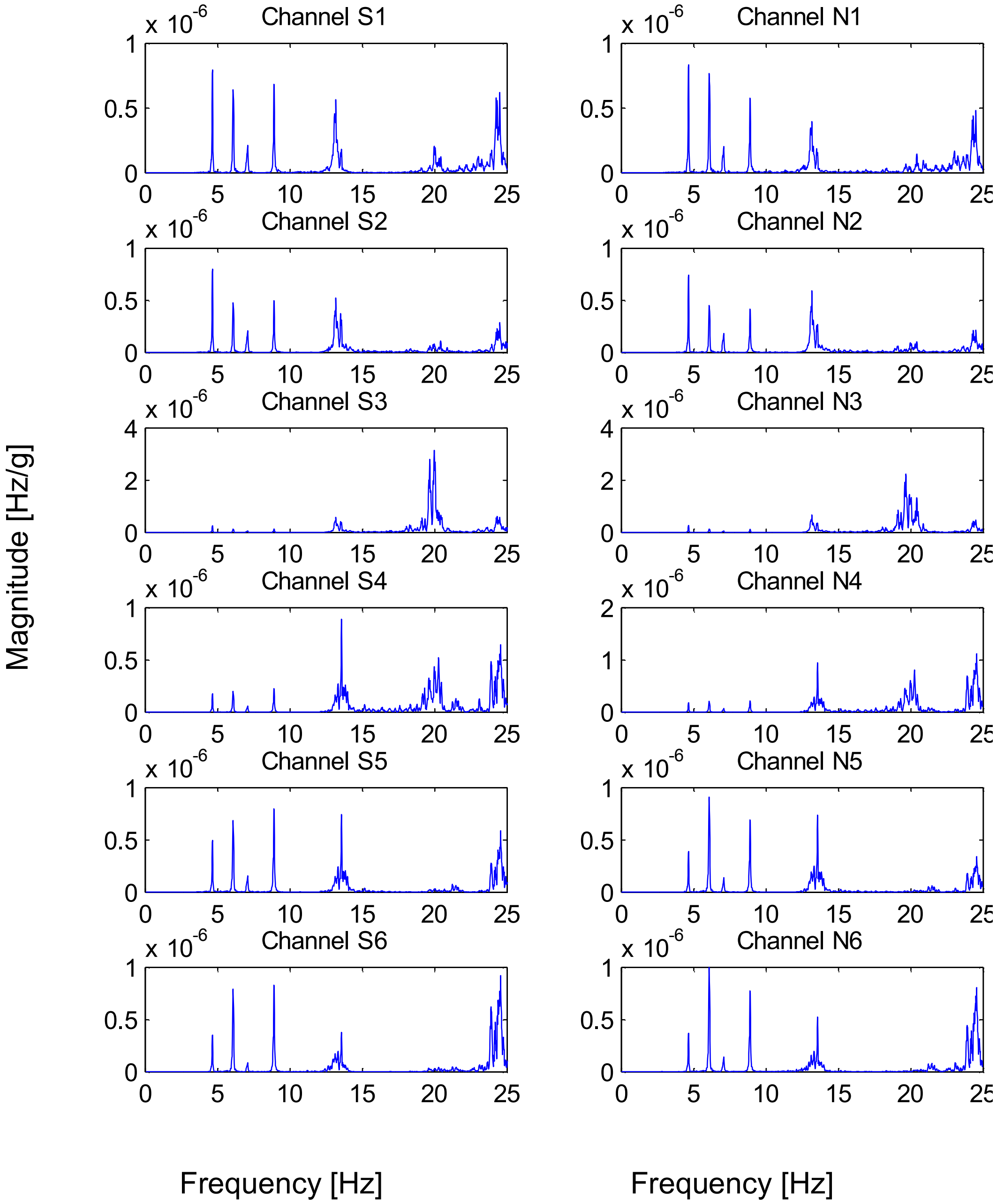

Figure A-6. Power Spectra Density of the 12 channels recorded during Test 2

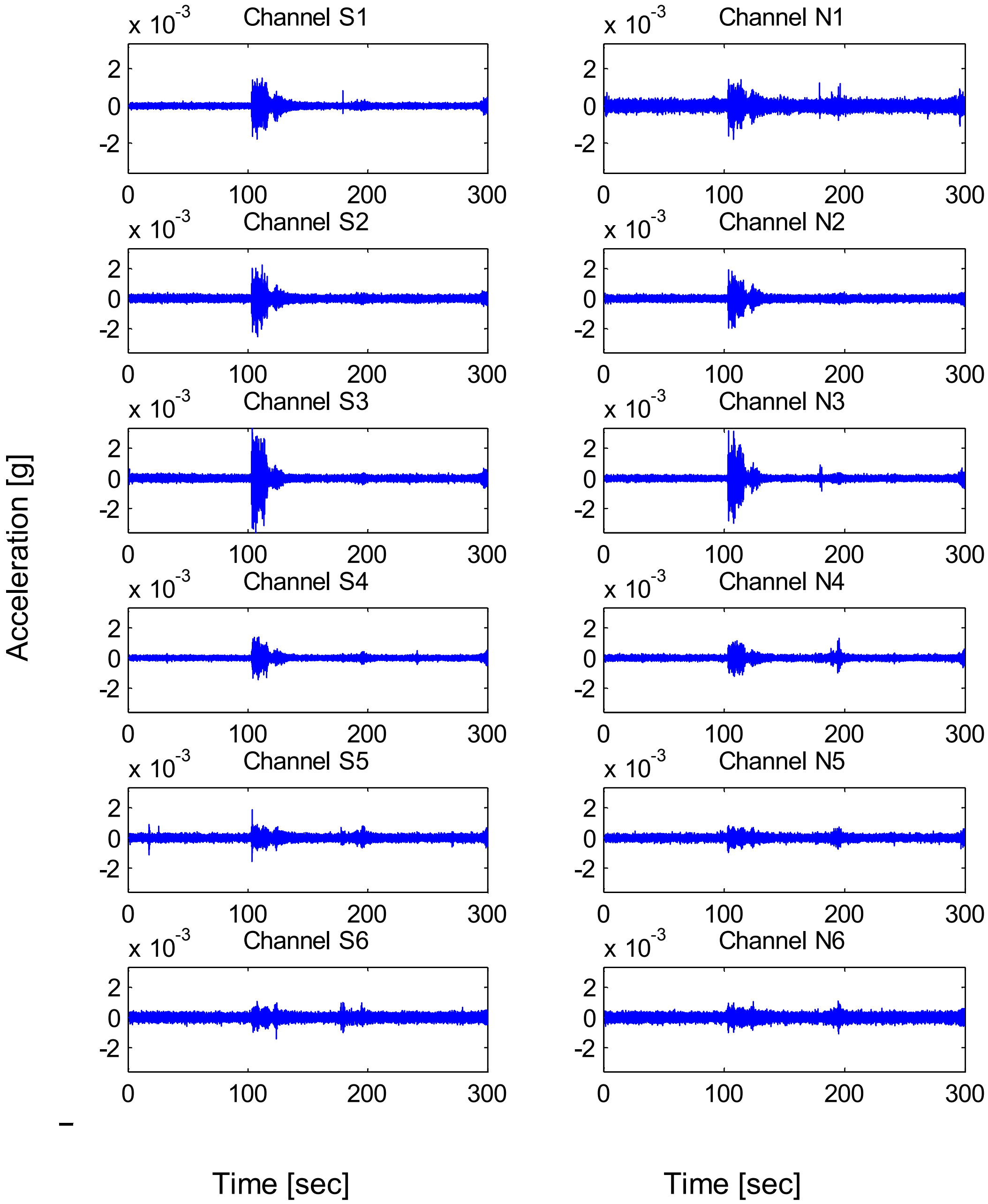

Figure A-7. Time history of the 12 channels recorded during Test 3

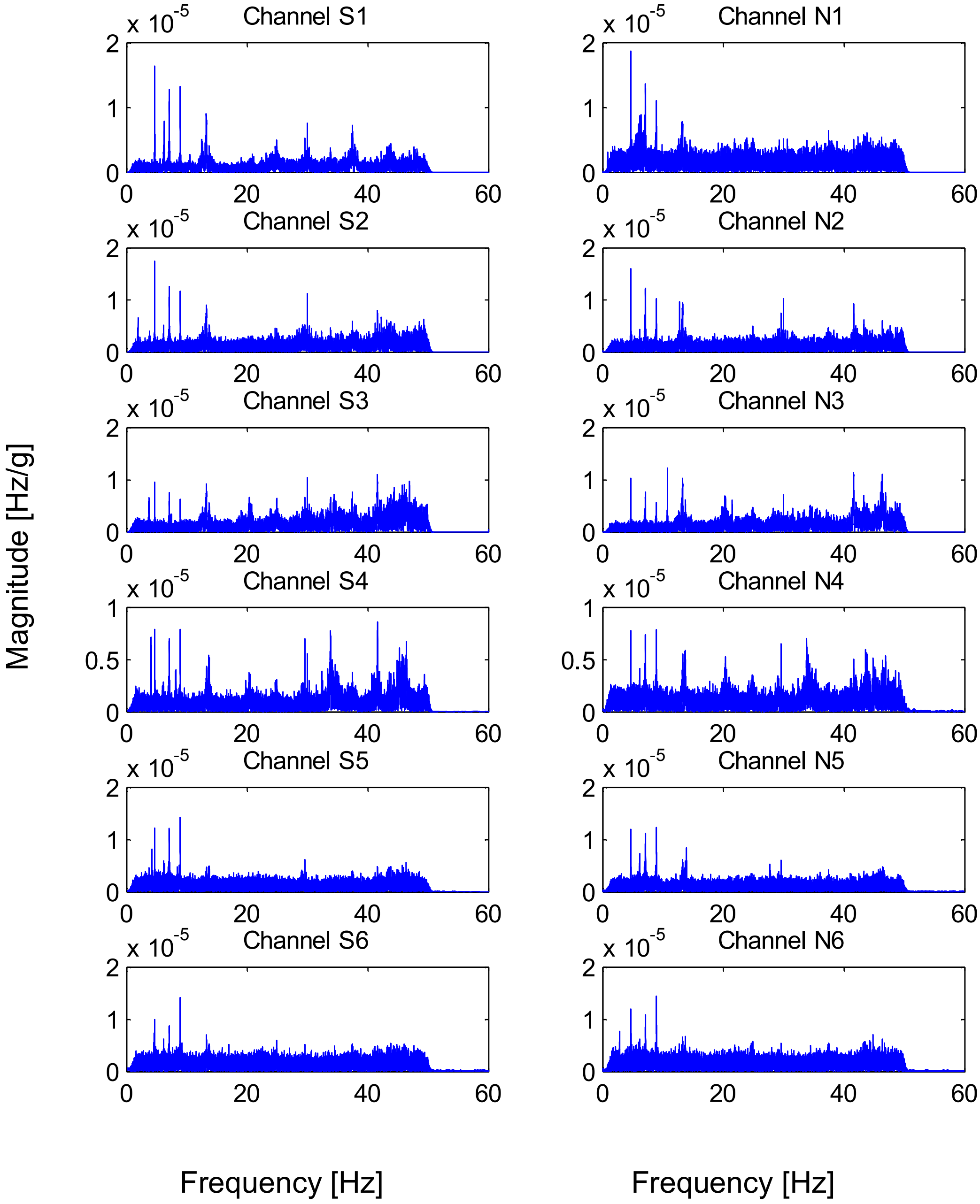

Figure A-8. Fourier amplitude spectra of the 12 channels recorded during Test 3

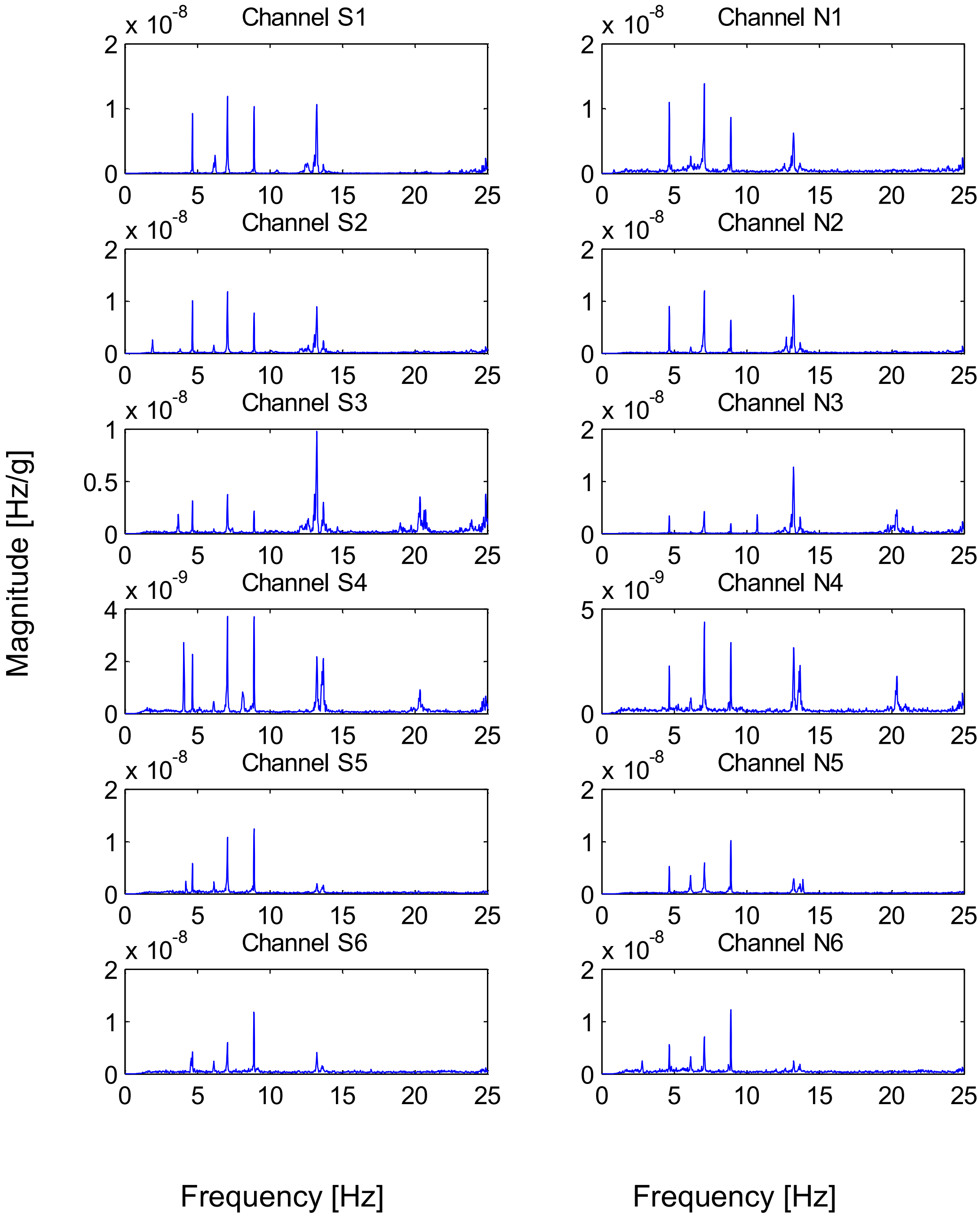

Figure A-9. Power Spectra Density of the 12 channels recorded during Test 3

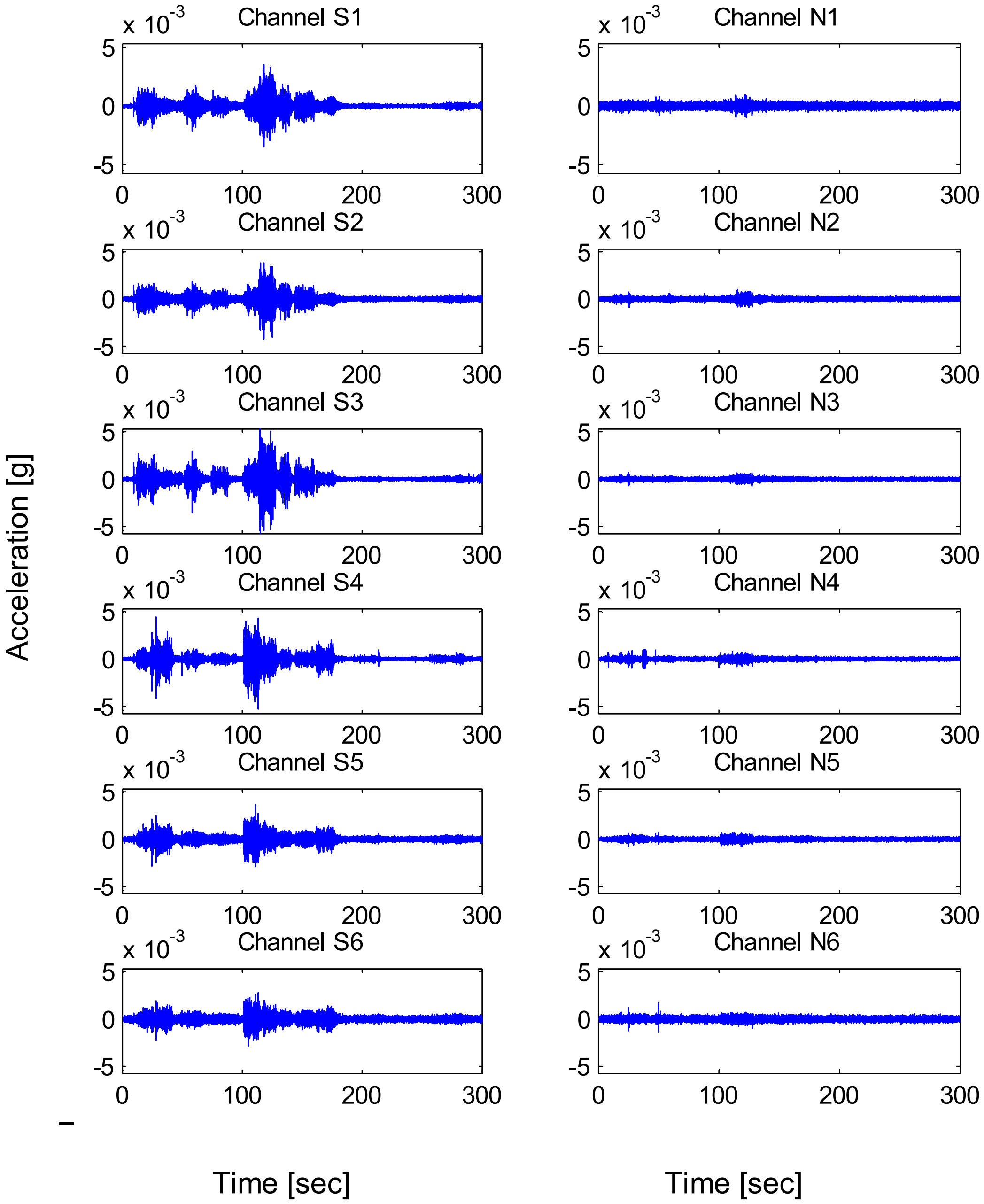

Figure A-10. Time history of the 12 channels recorded during Test 4

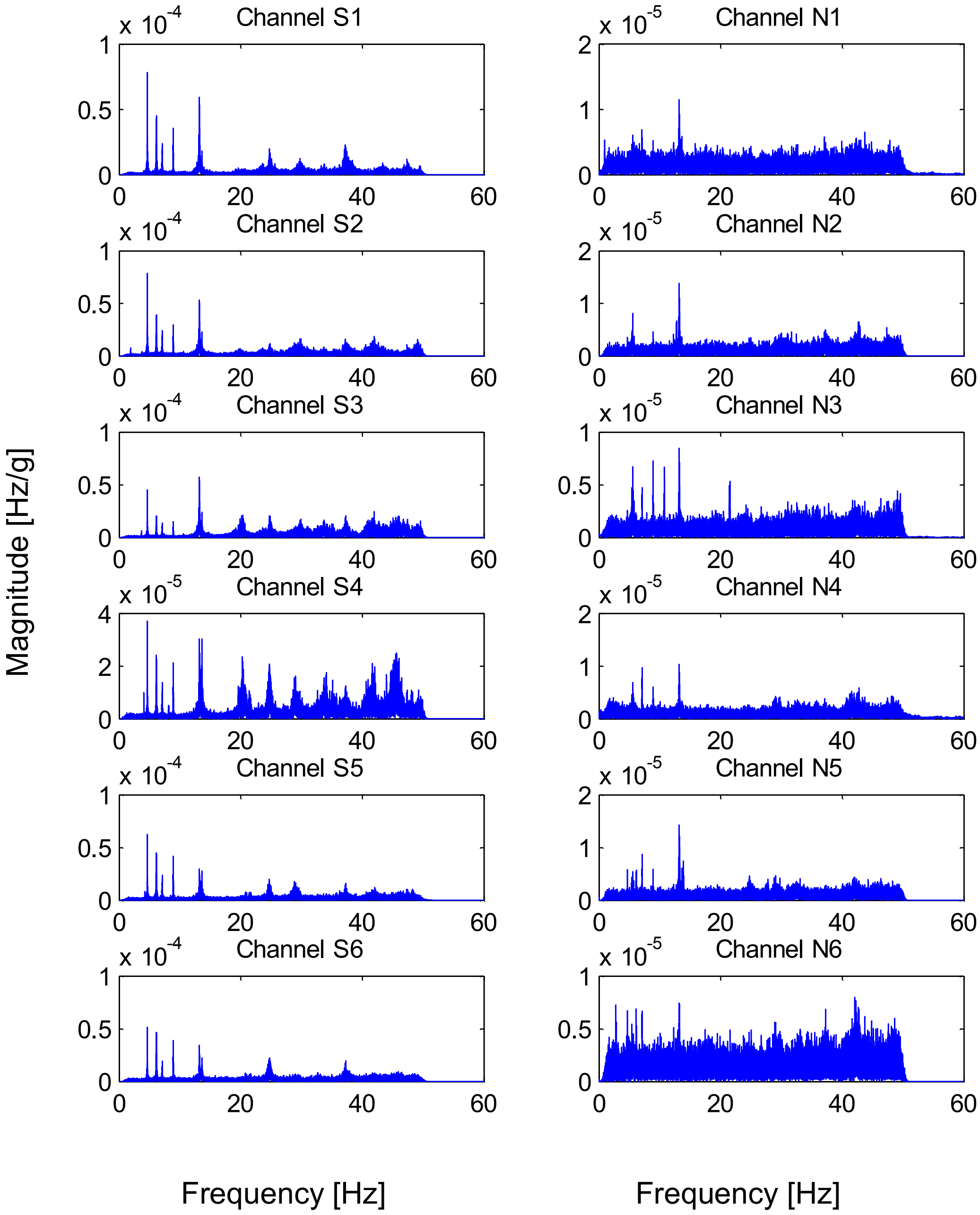

Figure A-11. Fourier amplitude spectra of the 12 channels recorded during Test 4

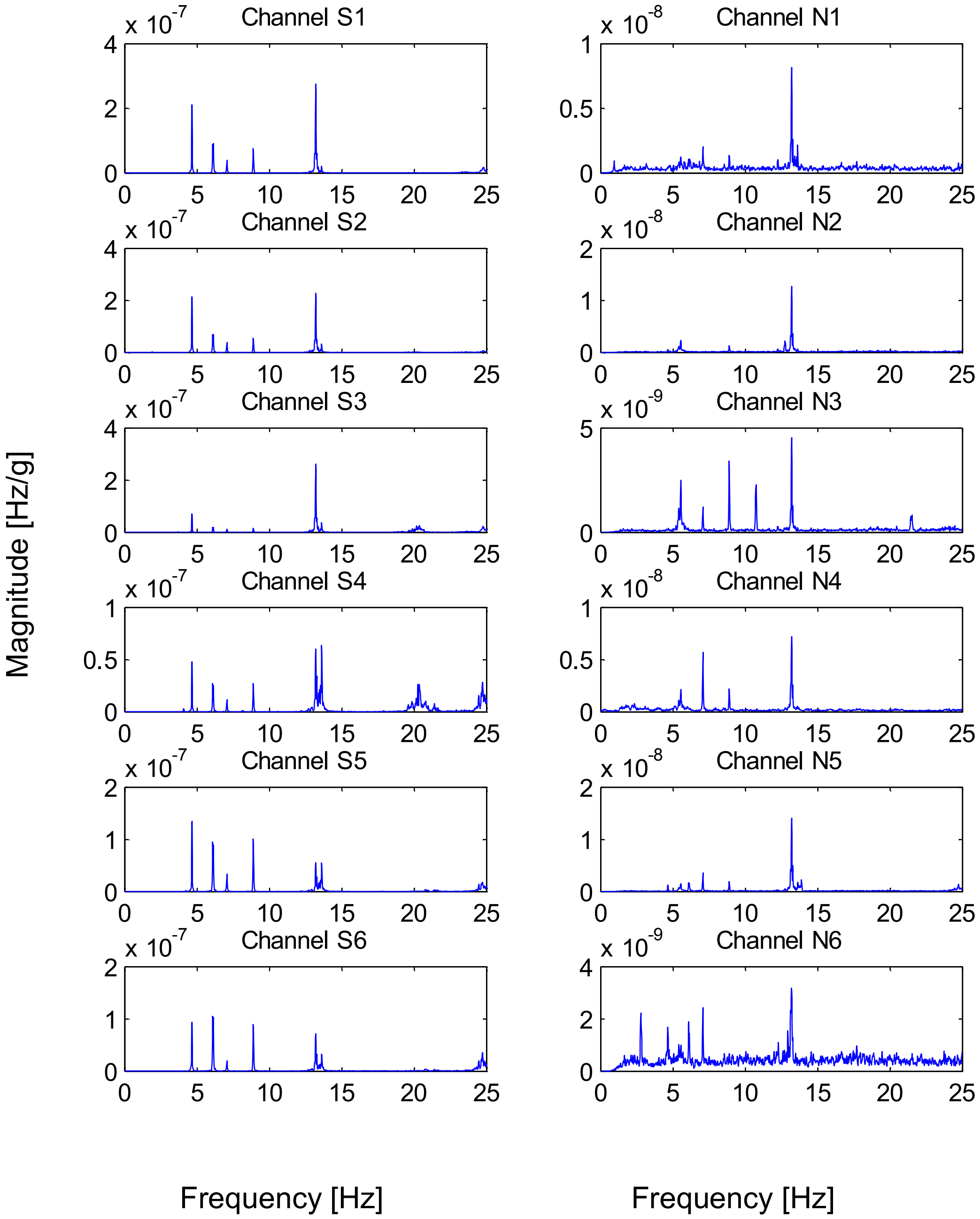

Figure A-12. Power Spectra Density of the 12 channels recorded during Test 4

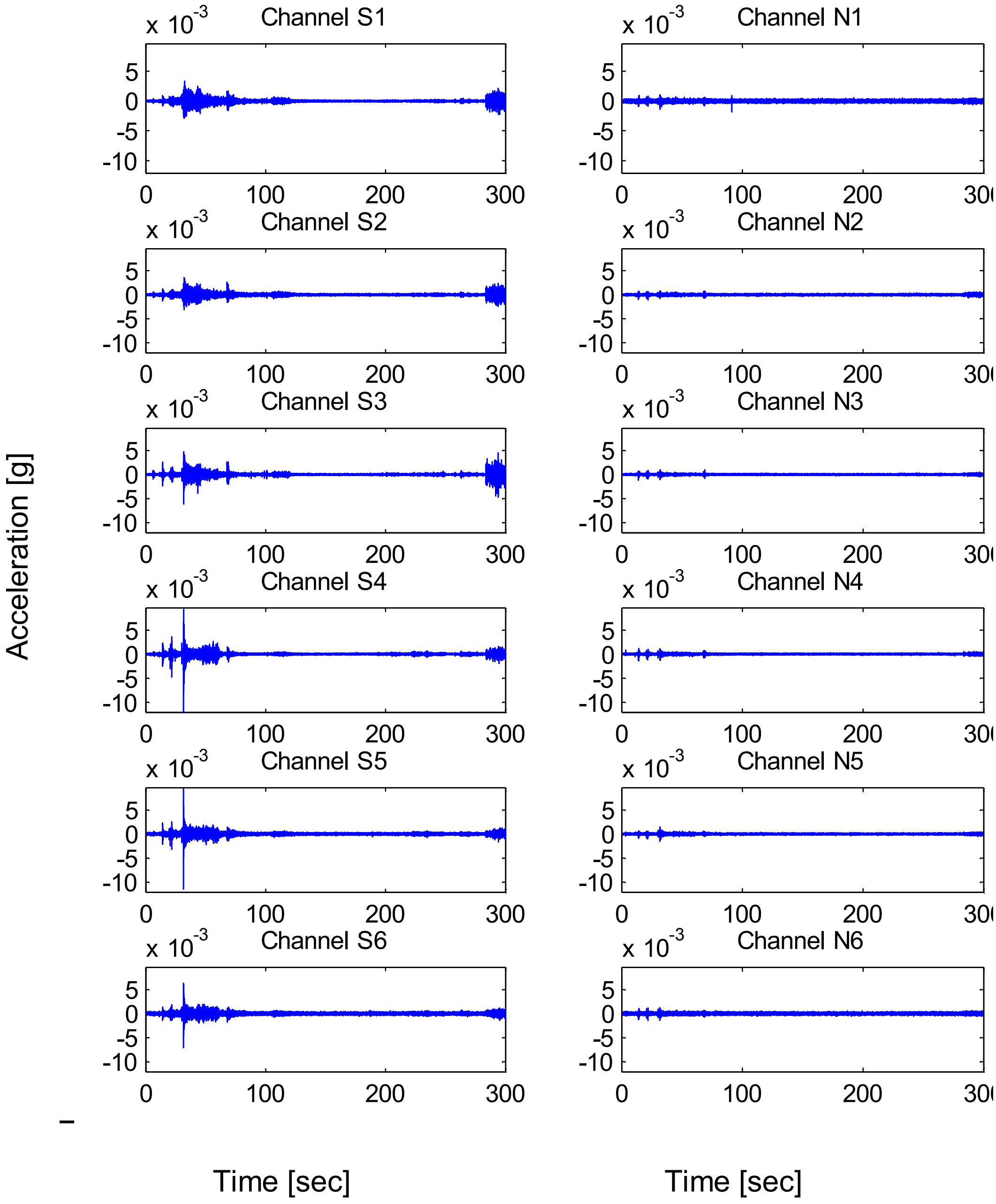

Figure A-13. Time history of the 12 channels recorded during Test 5

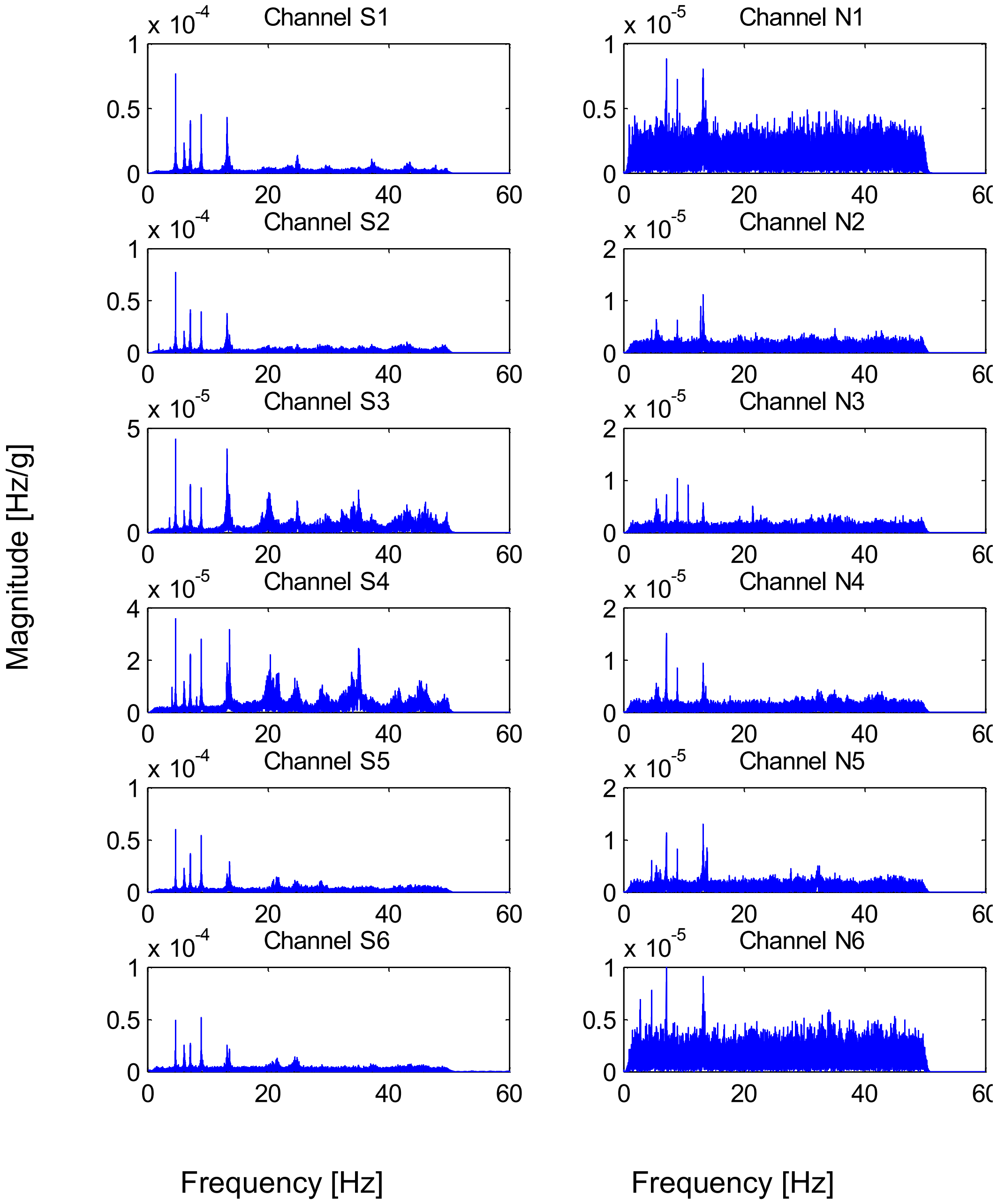

Figure A-14. Fourier amplitude spectra of the 12 channels recorded during Test 5

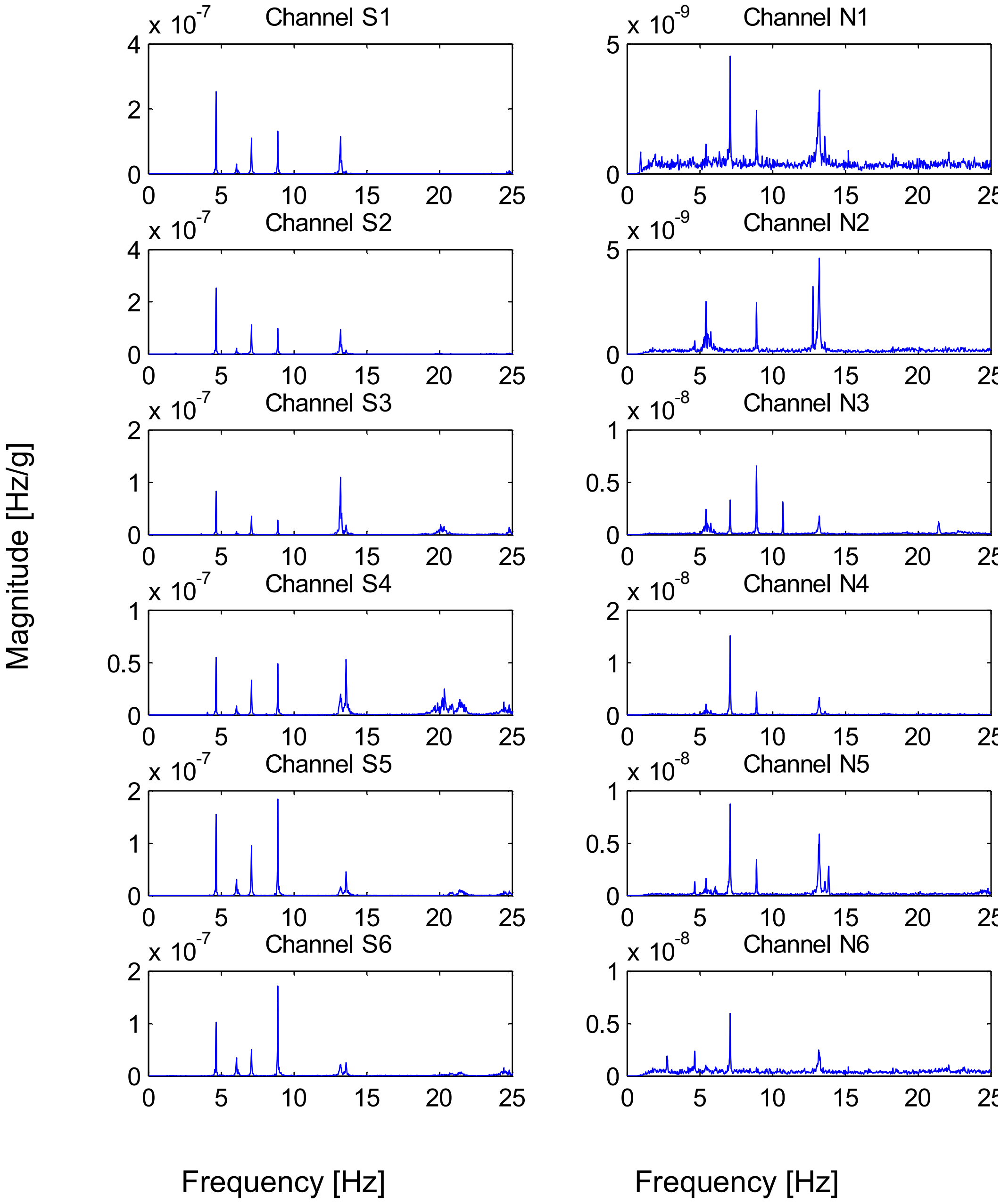

Figure A-15. Power Spectra Density of the 12 channels recorded during Test 5

APPENDIX B :

4 June Test

Time history, Fourier amplitude spectra and Power Spectral Density for all the channel and all the performed tests.

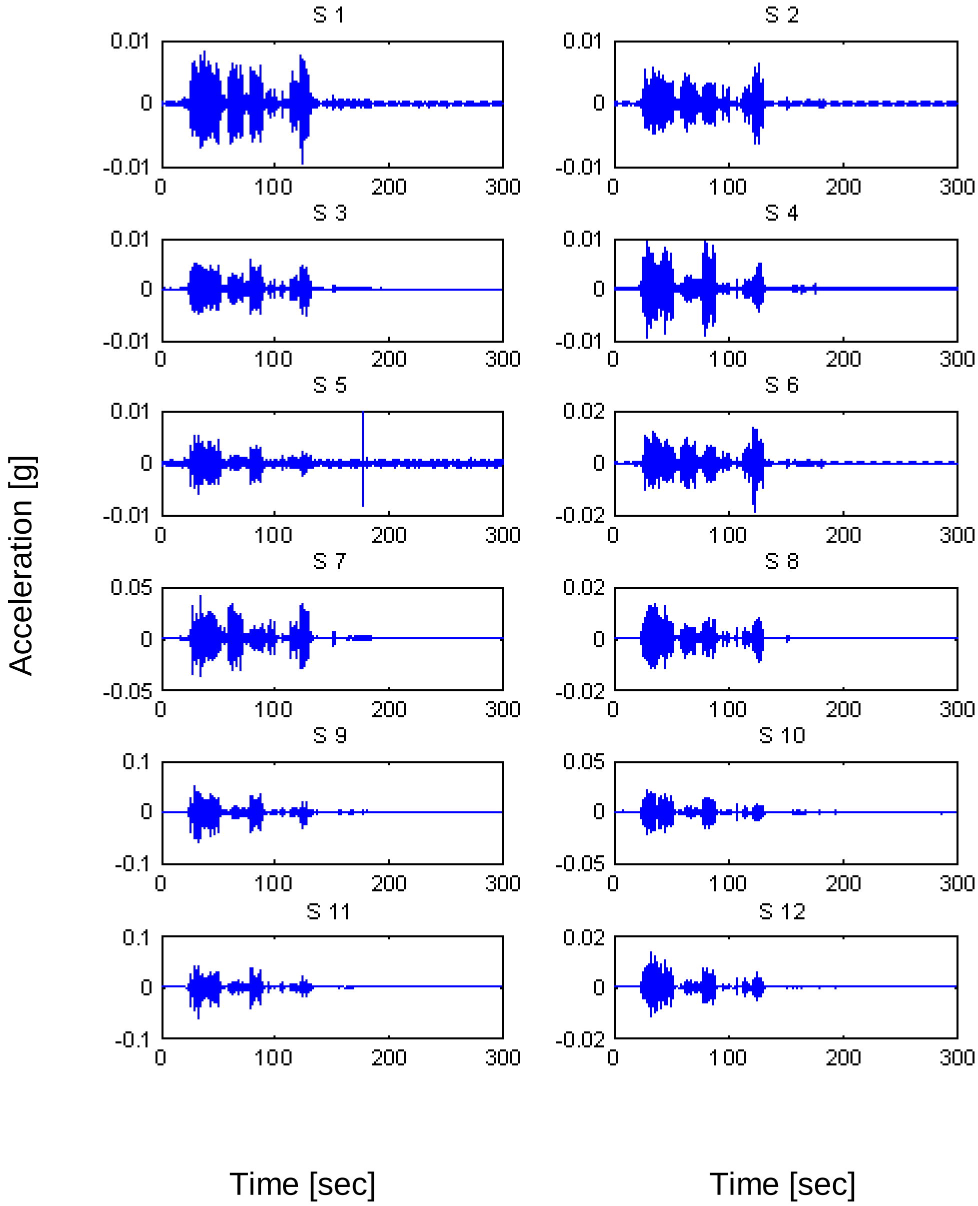

Figure B-1. Time history of the 12 channels recorded during Test 1

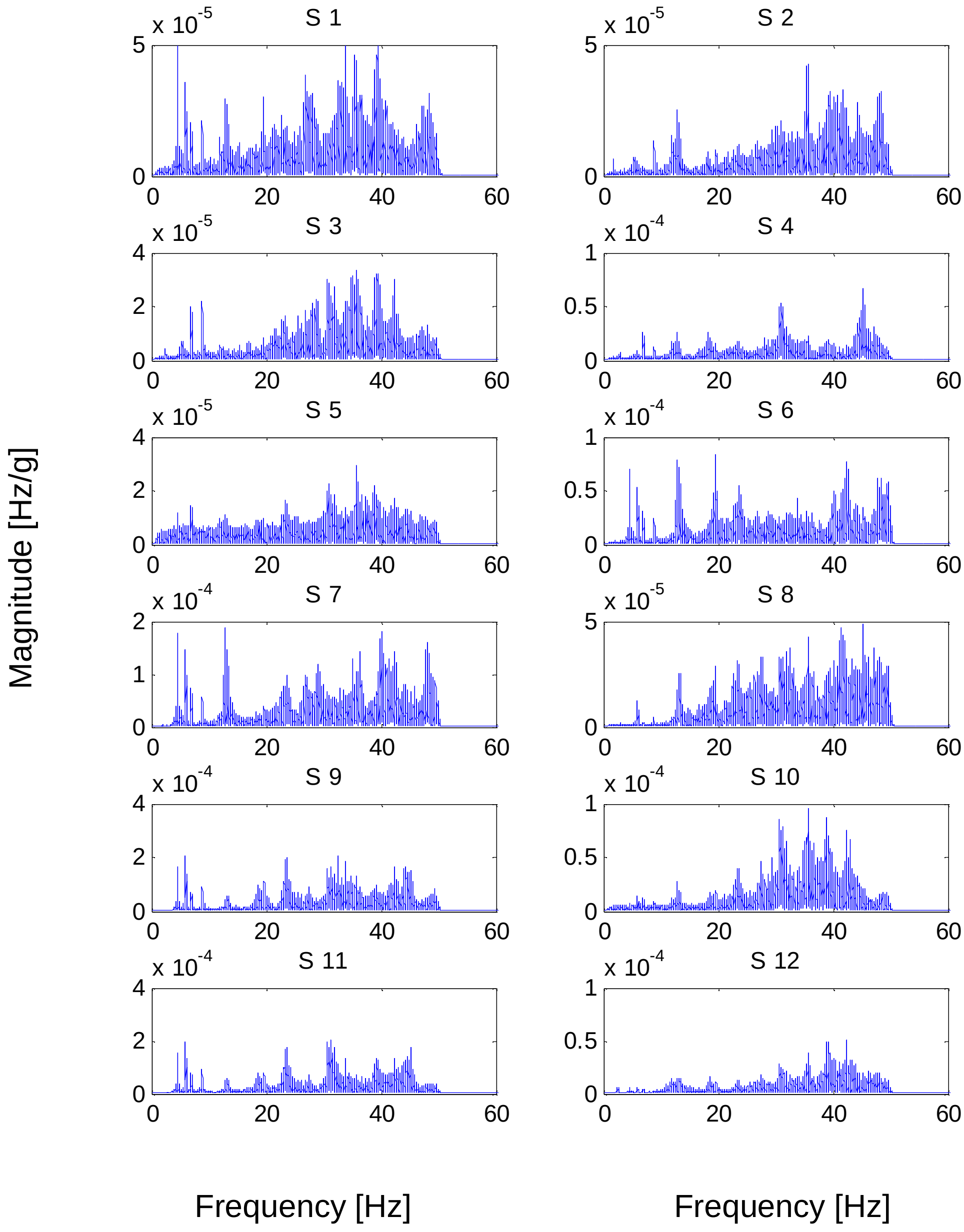

Figure B-2. Fourier amplitude spectra of the 12 channels recorded during Test 1

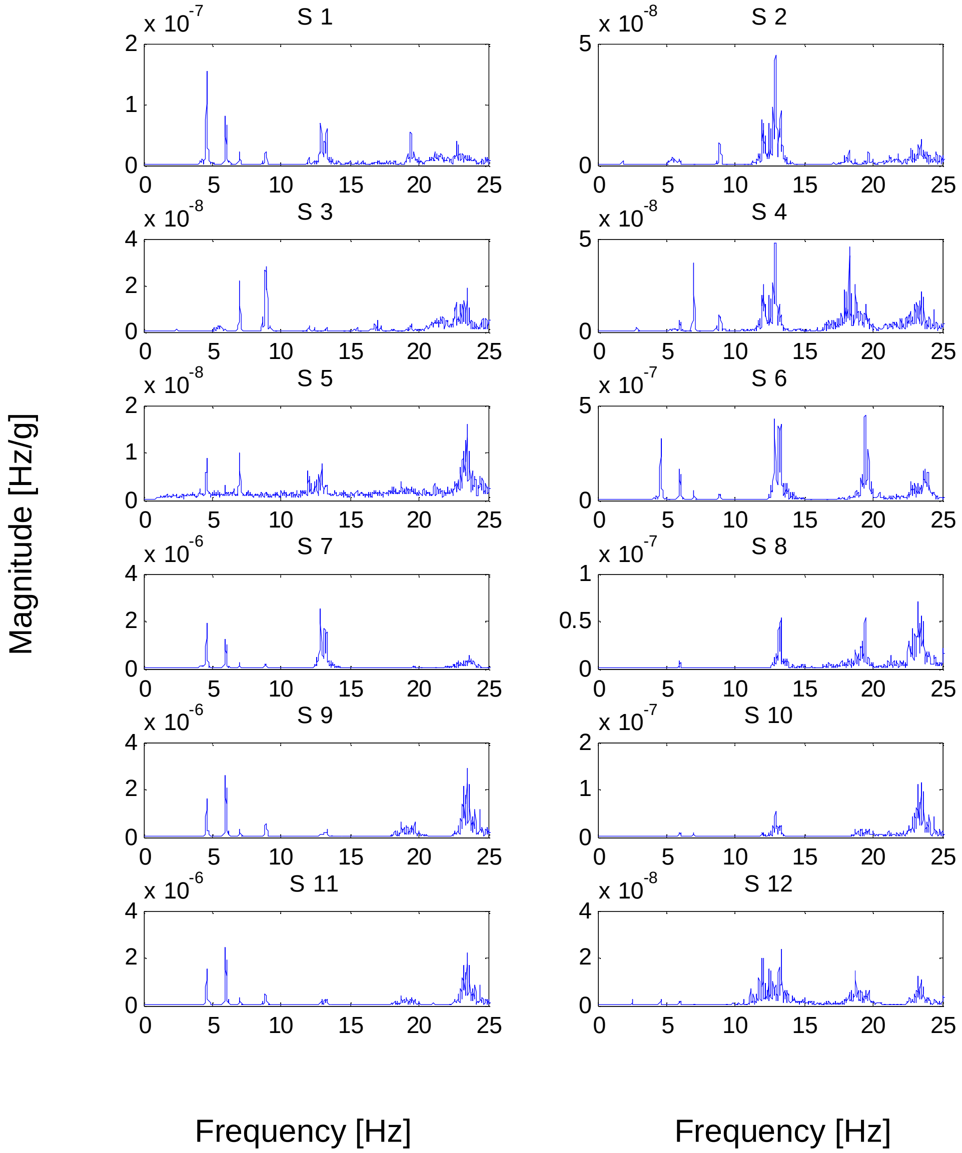

Figure B-3. Power Spectra Density of the 12 channels recorded during Test 1

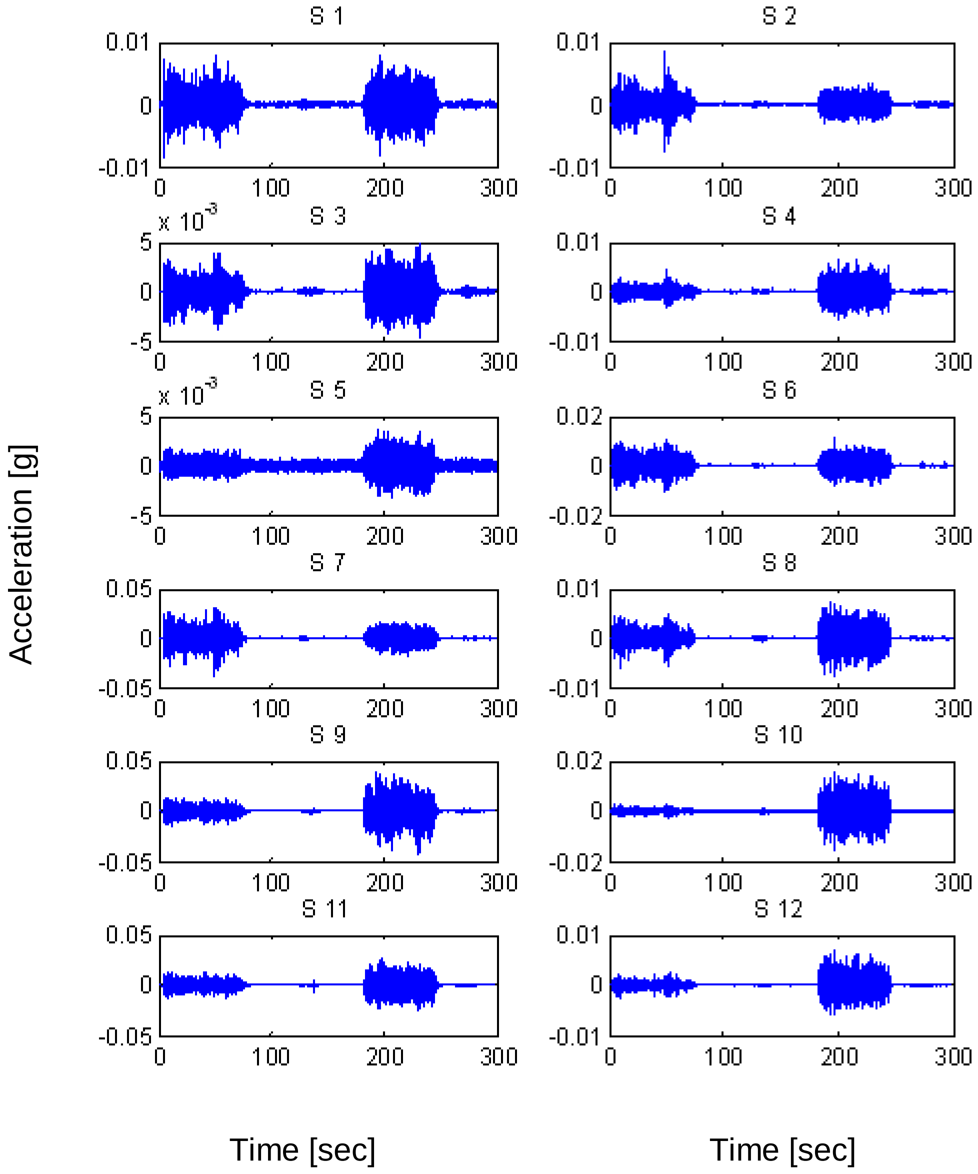

Figure B-4. Time history of the 12 channels recorded during Test 2

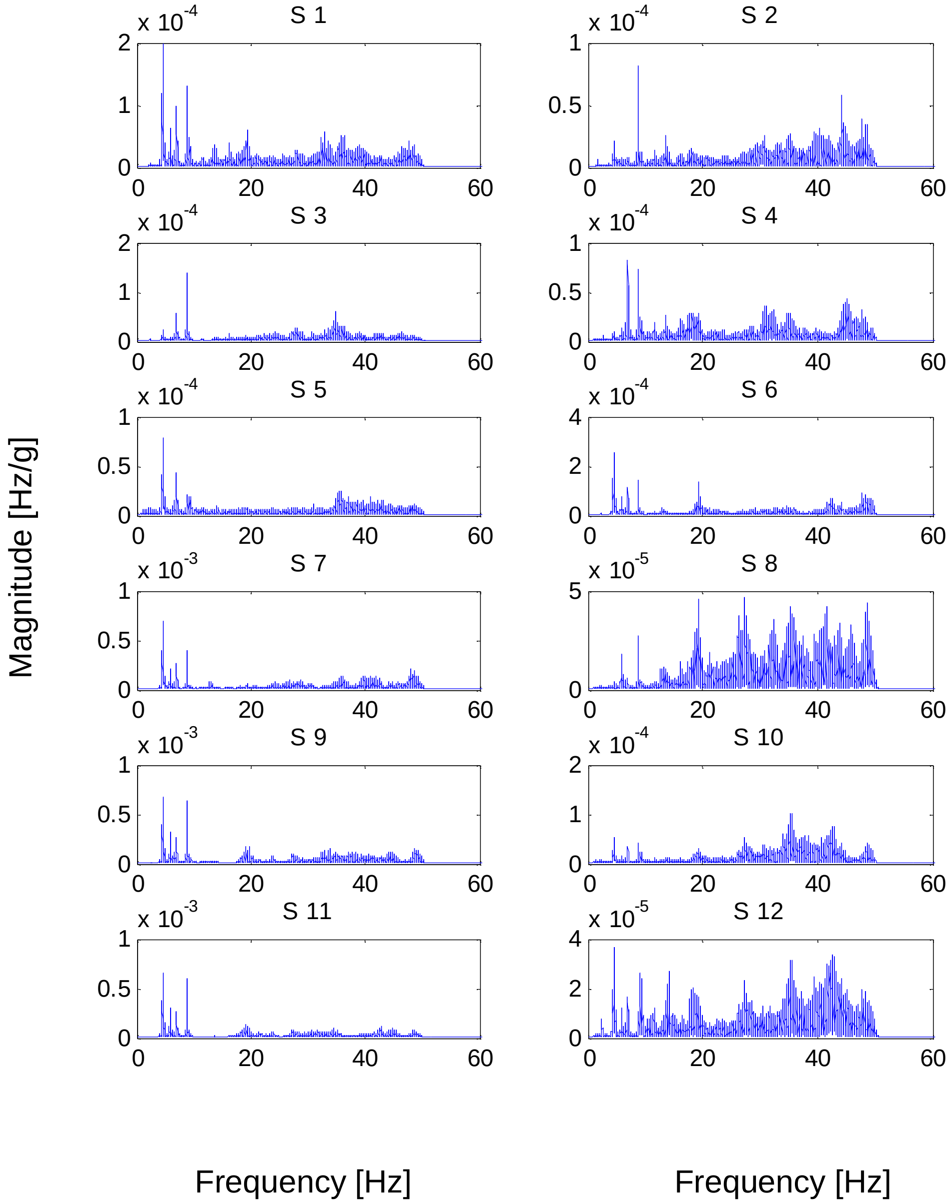

Figure B-5. Fourier amplitude spectra of the 12 channels recorded during Test 2

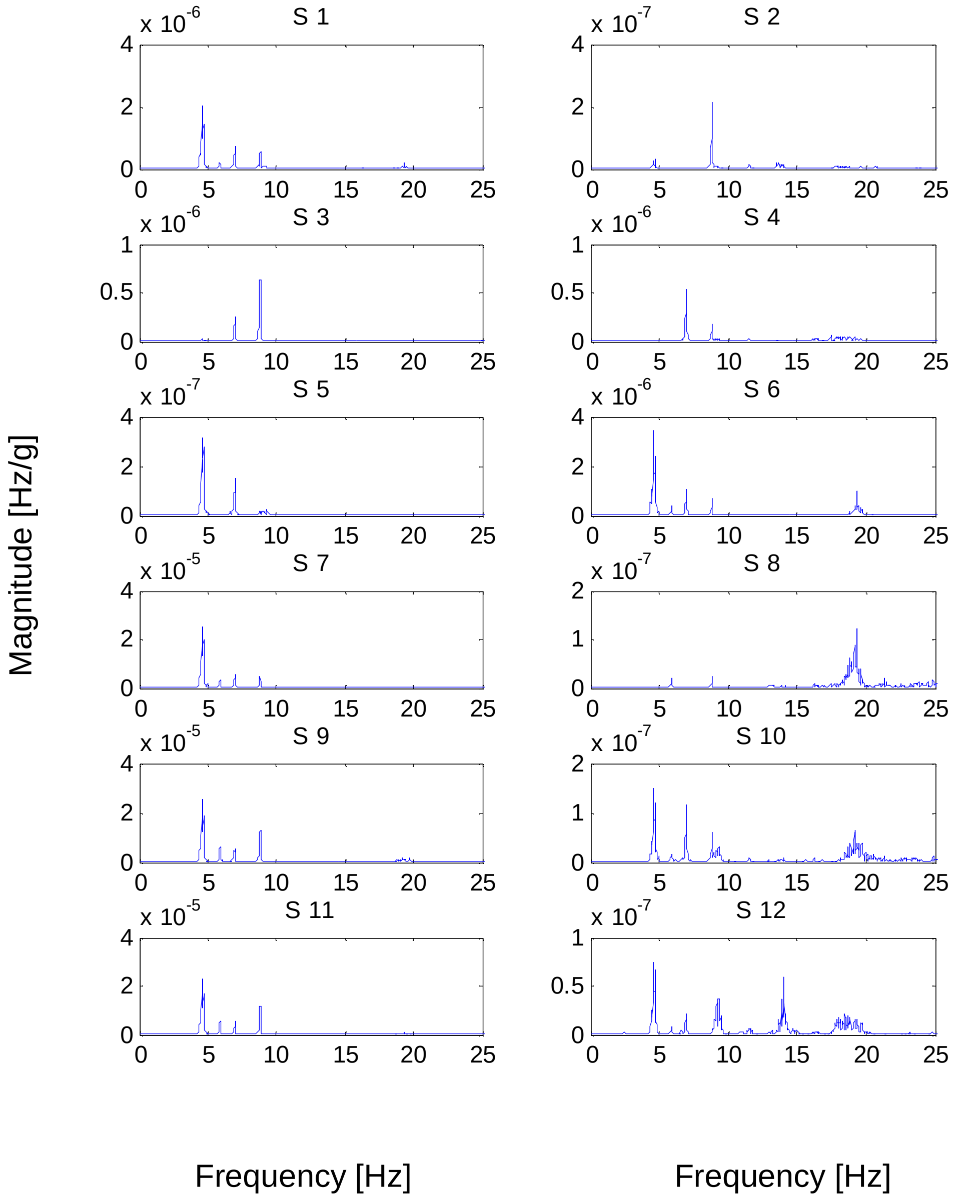

Figure B-6. Power Spectra Density of the 12 channels recorded during Test 2

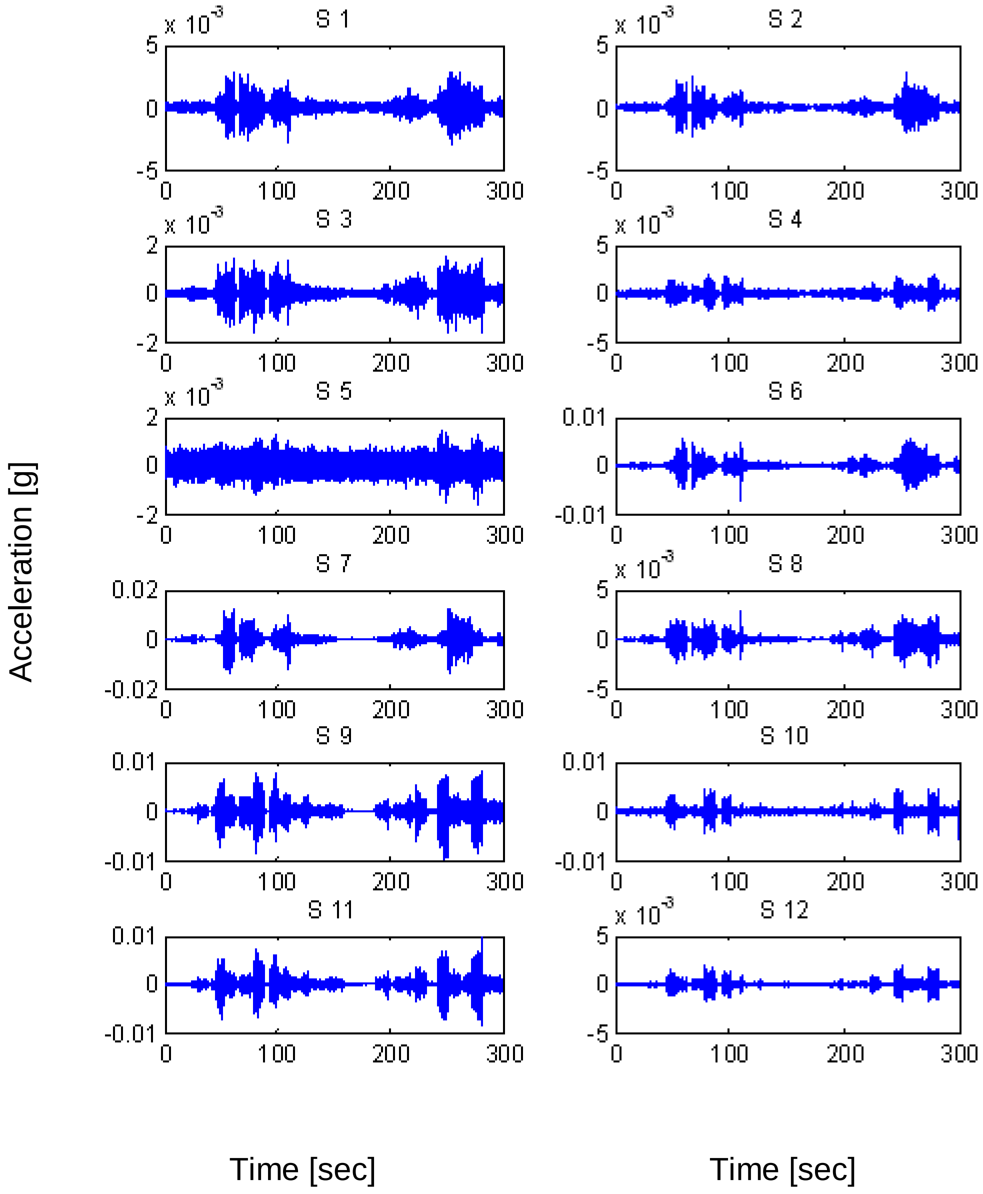

Figure B-7. Time history of the 12 channels recorded during Test 3

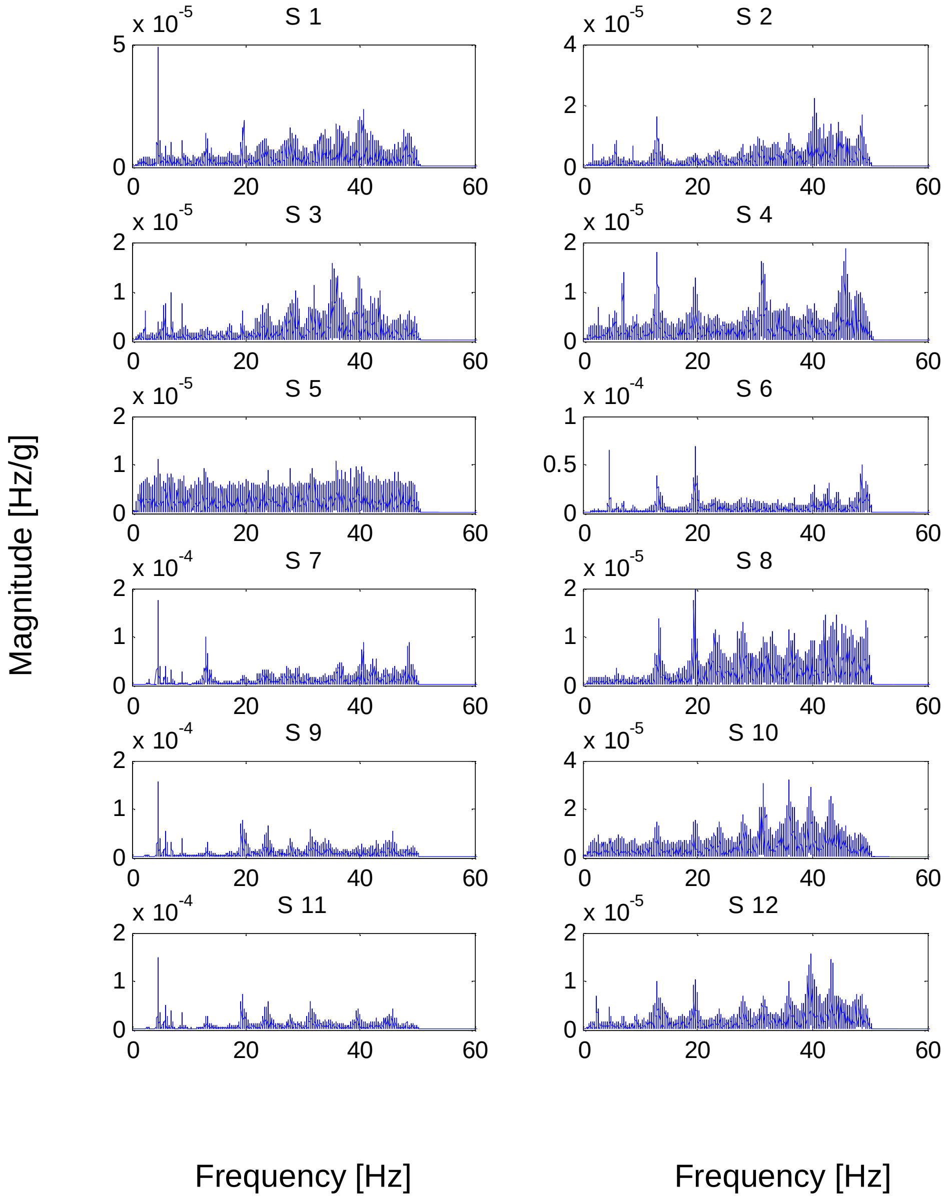

Figure B-8. Fourier amplitude spectra of the 12 channels recorded during Test 3

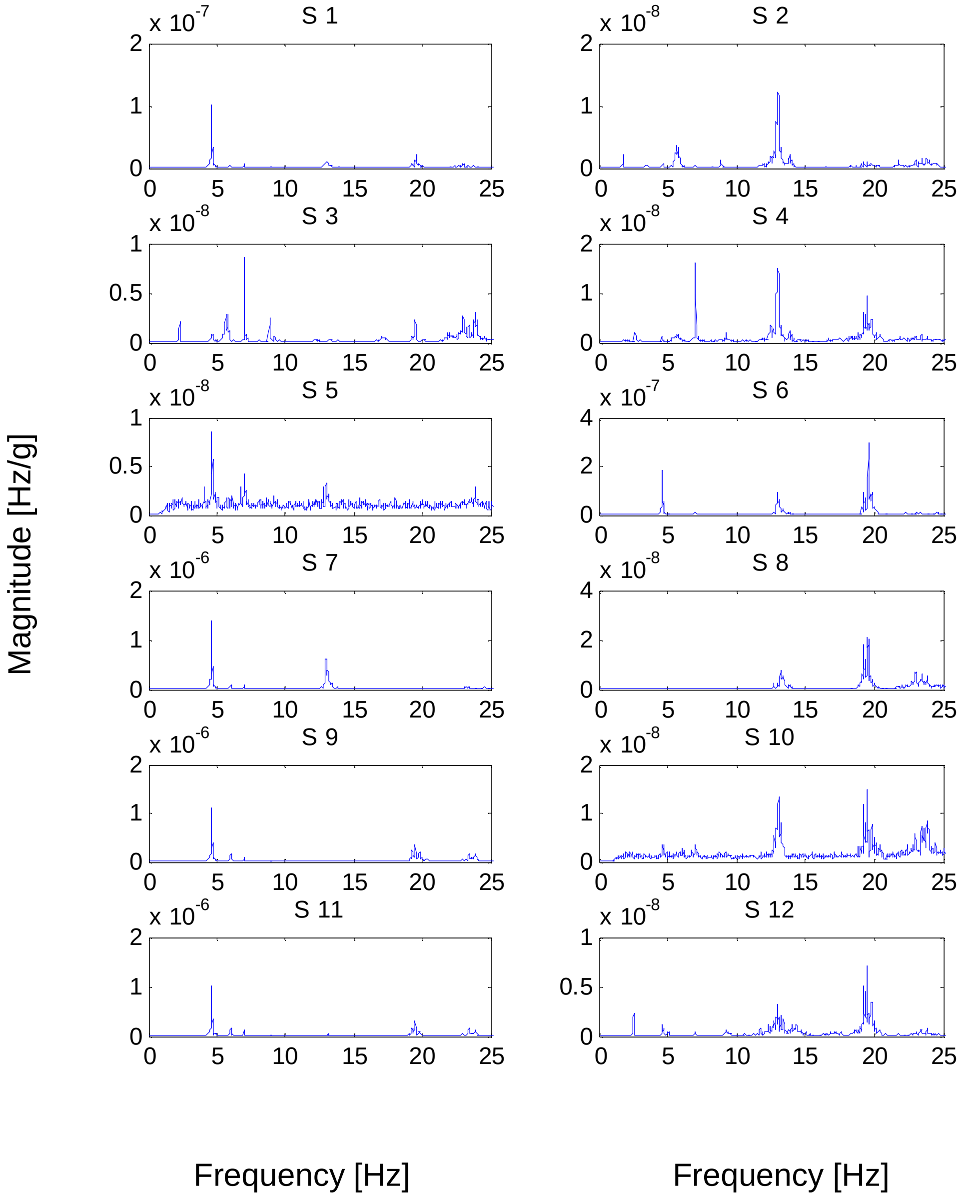

Figure B-9. Power Spectra Density of the 12 channels recorded during Test 3

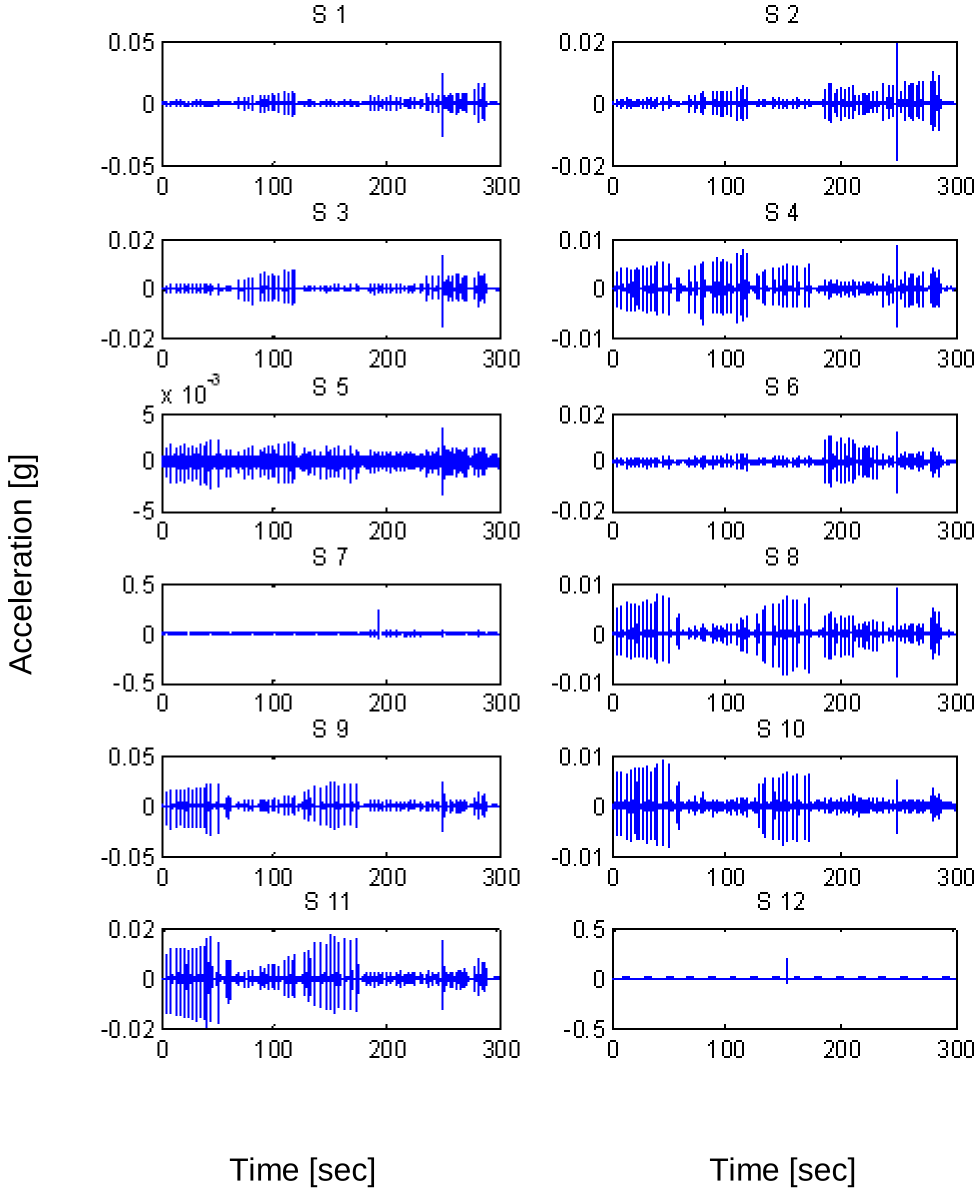

Figure B-10. Time history of the 12 channels recorded during Test 4

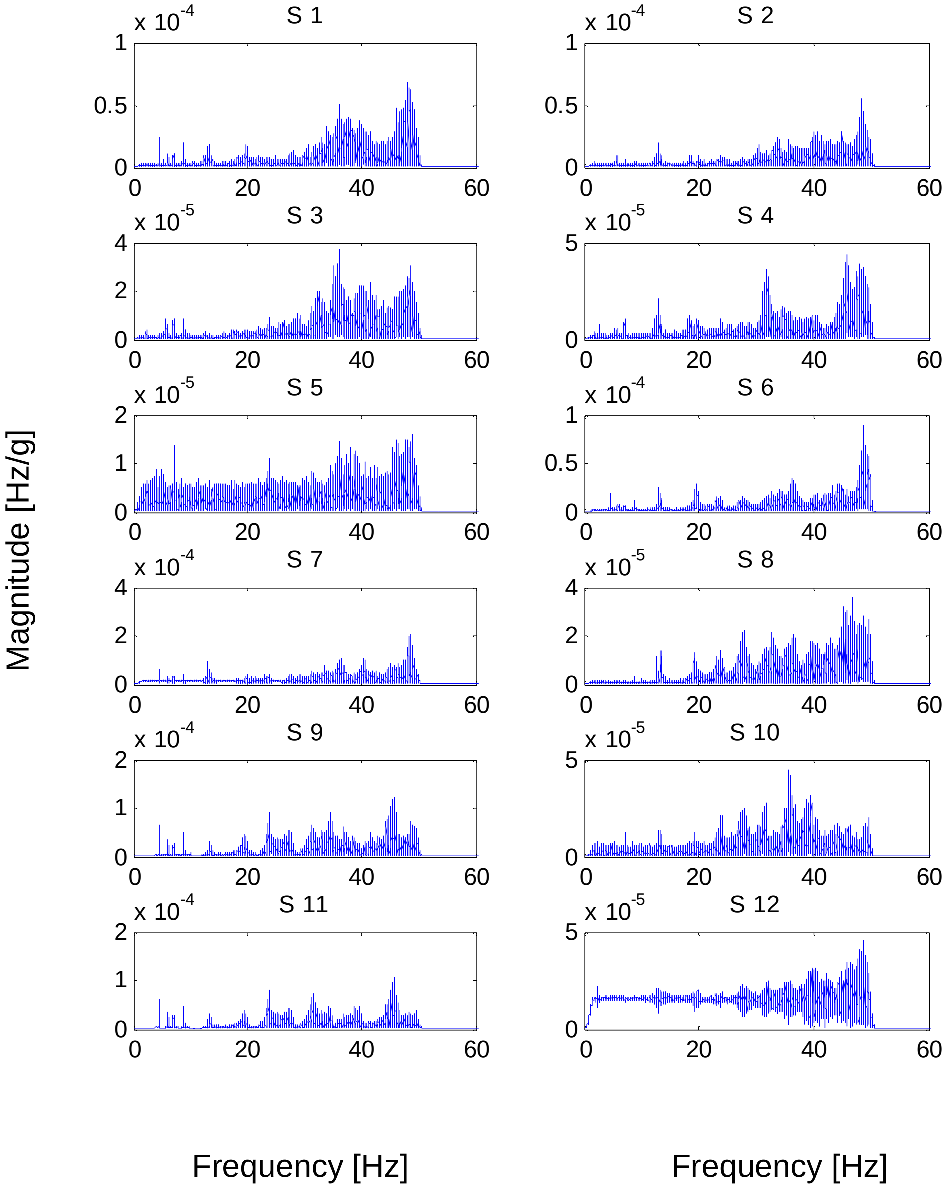

Figure B-11. Fourier amplitude spectra of the 12 channels recorded during Test 4

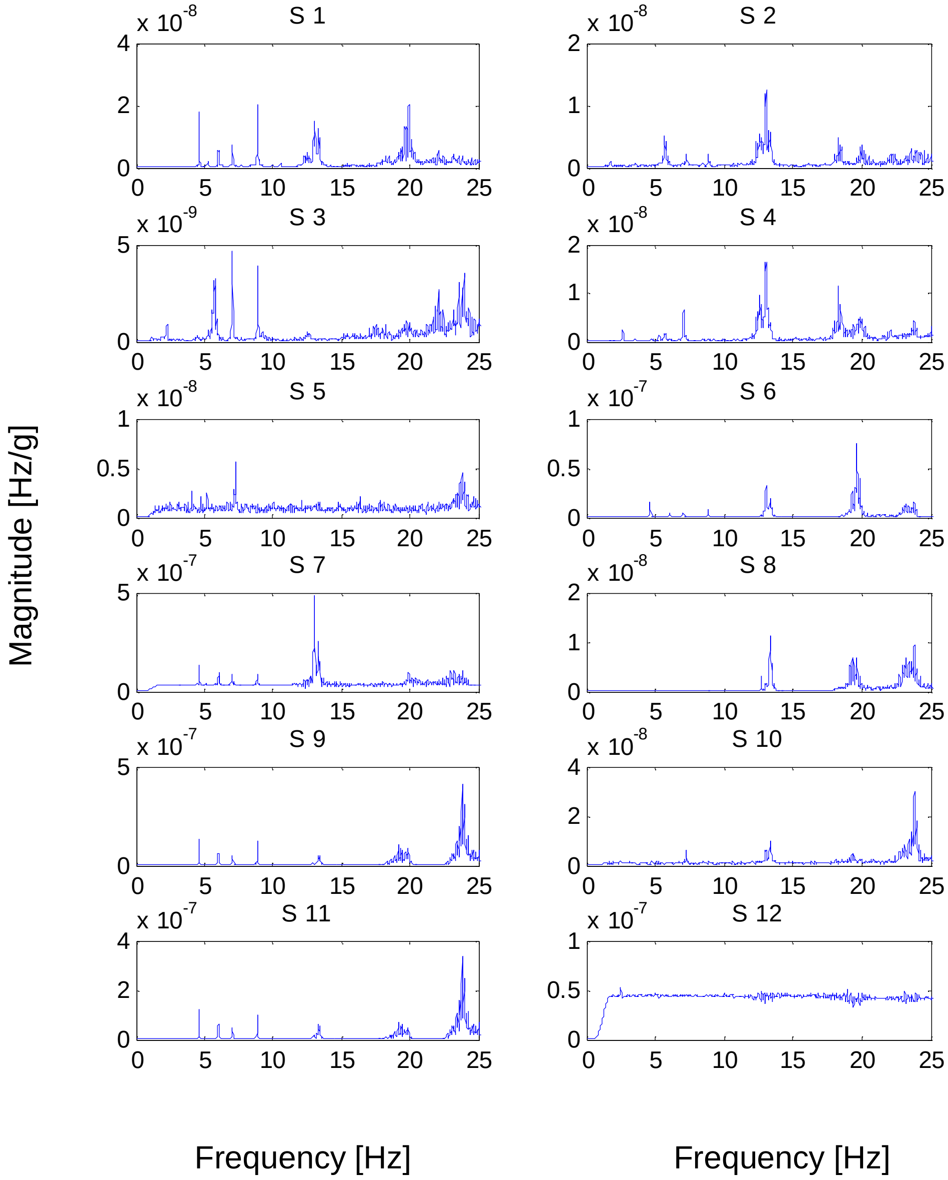

Figure B-12. Power Spectra Density of the 12 channels recorded during Test 4

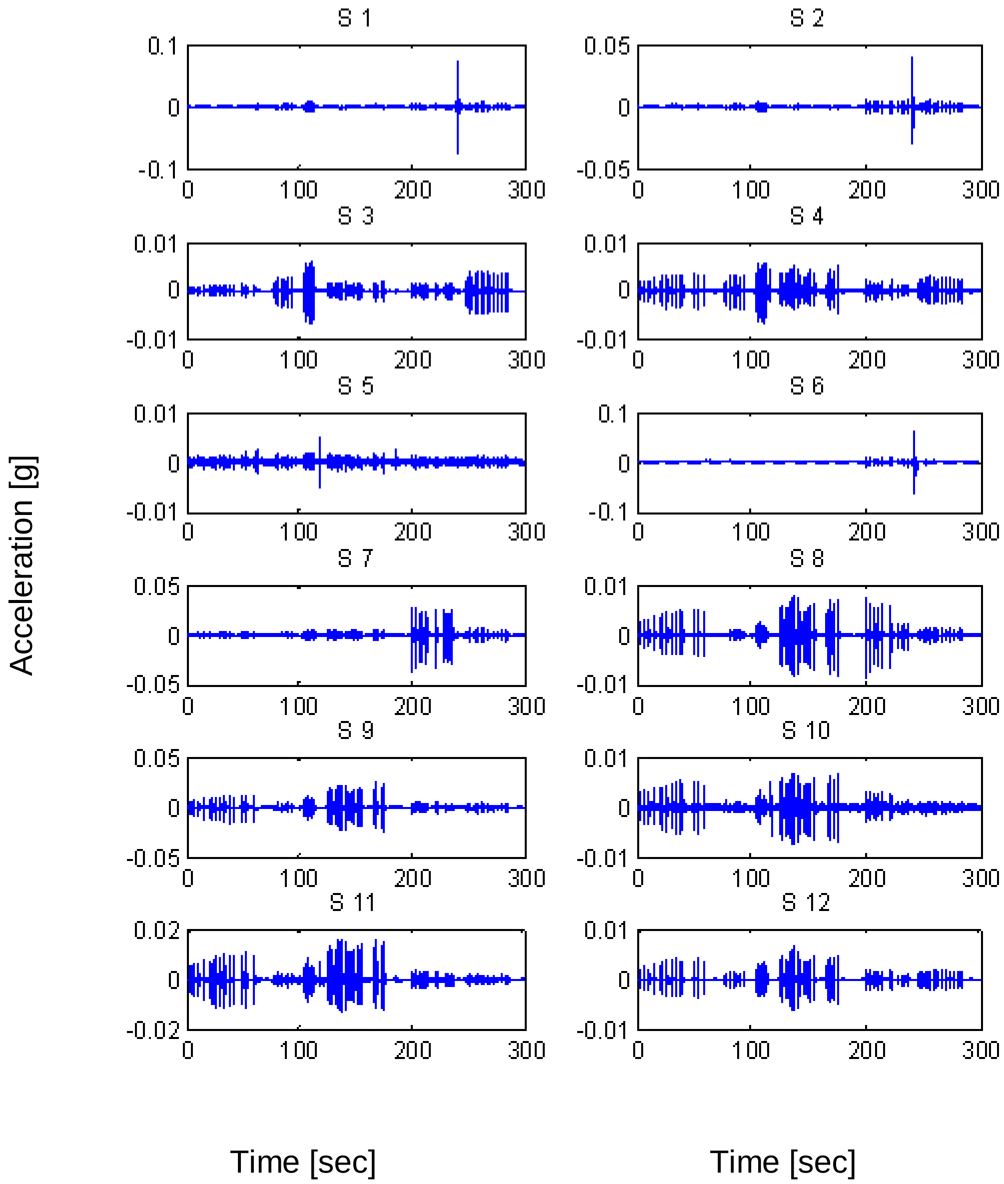

Figure B-13. Time history of the 12 channels recorded during Test 5

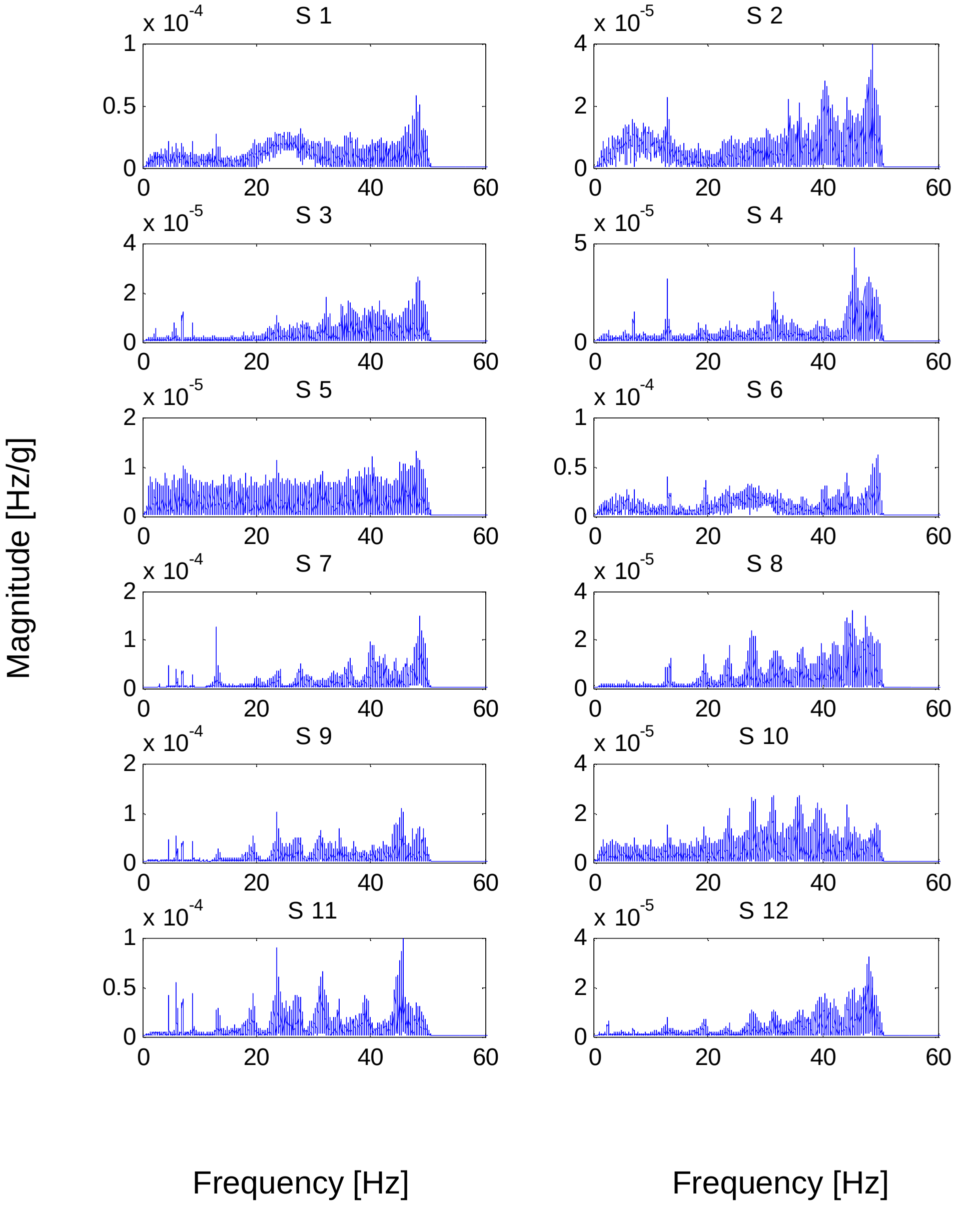

Figure B-14. Fourier amplitude spectra of the 12 channels recorded during Test 5

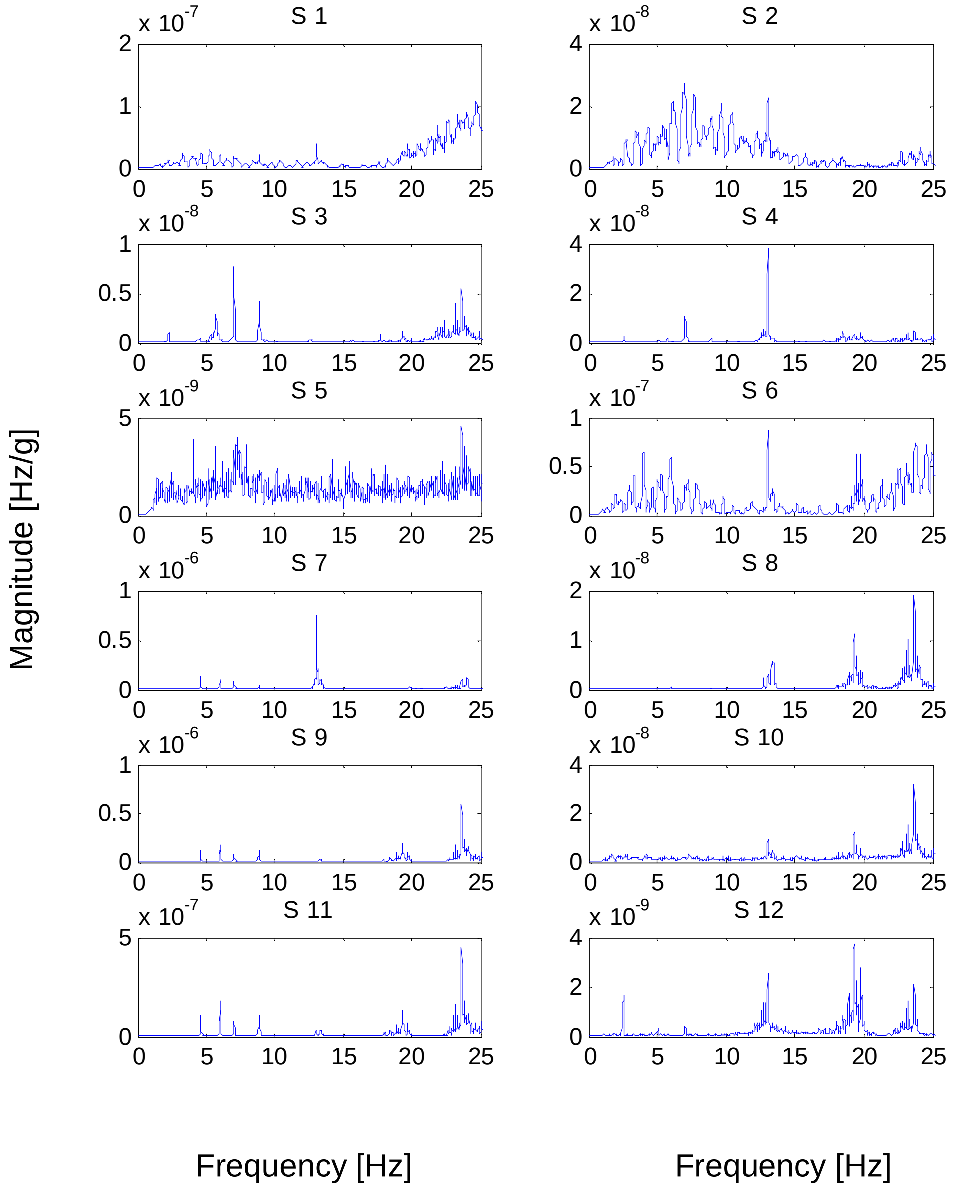

Figure B-15. Power Spectra Density of the 12 channels recorded during Test 5